Self-Tuning Electromagnetic Vibration Systems

by

Seyed Hossein Kamali

M.Sc., Sharif University of Technology, 2014
B.Sc., University of Tehran, 2012

Thesis Submitted in Partial Fulfillment of the
Requirements for the Degree of
Doctor of Philosophy

in the
School of Mechatronic Systems Engineering
Faculty of Applied Sciences

SIMON FRASER UNIVERSITY
Summer 2019

Approval

Name:	**Seyed Hossein Kamali**
Degree:	**Doctor of Philosophy (Mechatronic Systems Engineering)**
Title:	**Self-Tuning Electromagnetic Vibration Systems**
Examining Committee:	**Chair:** Woo Soo Kim Associate Professor
	Mehrdad Moallem Senior Supervisor Professor
	Siamak Arzanpour Supervisor Associate Professor
	Kevin Oldknow Supervisor Senior Lecturer
	Flavio Firmani Internal Examiner Lecturer
	Ryozo Nagamune External Examiner Associate Professor Department of Mechanical Engineering The University of British Columbia
Date Defended:	**May 6th, 2019**

Abstract

This thesis presents the efforts made toward making industrial mechanical vibration systems smarter. This objective is accomplished in two steps. The first step is realization of mechanical vibration actuators that can mimic the behaviour of mechanical dampers and springs with variable and controllable damping and stiffness. The second step includes the design and implementation of algorithms that can find the optimum damping and stiffness in different operating conditions.

First, electromagnetic actuators are selected for force generation. It is shown that creating a parallel RL circuit with variable parameters in the shunt of an electromagnetic actuator results in variable damping and stiffness behavior by the actuator. It is shown that this circuit configuration can be realized using a power electronics converter connected to a power source. Next, automatic control methods are developed for adding a self-tuning loop to the system including an electromagnetic actuator. To this end, the sliding mode extremum seeking controller was utilized to make the system self-tuning in a model-free control architecture.

The concept is applied to two major problems in vibration systems: vibration energy harvesting and vibration absorption, which is also known as tuned mass damping. In the former application, single variable and multi-variable sliding mode extremum seeking controllers are used for controlling the damping and stiffness of the actuator to maximize the harvested power. In the latter case, the same controller is used with the objective of minimizing the unwanted oscillations in a host structure.

Analytical methods, computer simulations, and experimental results are provided to support the proposed concept and verify the theoretical findings. The results show that it is possible to achieve efficient, variable, and controllable damping and stiffness with an electromagnetic actuator comprised of a brushless DC motor and a mechanical motion conversion mechanism. It was also shown that the proposed extremum seeking controllers successfully tune the variables toward the optimum points.

Keywords: Adaptive Control; Electromagnetic Actuators; Vibration Systems; Power Electronics

’Exaltations to You, ’the angels replied to God, ’we have no knowledge except that which You have taught us. You are indeed the Knowing, the Wise.’

Holy Quran [1:32]

Acknowledgements

This project would not have gone anywhere without the effective and professional supervision of my senior supervisor professor Mehrdad Moallem. I give thanks to him for his invaluable support and giving me the motivation to be creative and productive. He gave me the confidence to explore some topics in power electronics and control that were unknown to me. He encouraged me to gain a broad understanding of mechatronics, which will help me through my future career. I also thank my other supervisors Dr. Siamak Arzanpour and Dr. Kevin Oldknow for providing me with their precious feedback to improve the quality of the work.

I express my gratitude to the examining committee Dr. Ryozo Nagamune and Dr. Flavio Firmani for accepting to be present in my defence. I also thank Dr. Woo Soo Kim for chairing the defence session. I offer Thanks to all my fellow graduate students at the Motion and Power Electronics Control Laboratory. I give special thanks to Dr. Jalal Amini and Mohammadhossein Miri who directly contributed to the project.

I acknowledge the funding provided by the Natural Sciences and Engineering Research Council of Canada (NSERC). I also thank the Kaiser Foundation for providing me with the Kaiser Foundation Award for Digitally Controlled Power Electronics. I would also thank professor Olof Samuelsson, who hosted me during my research visit at Lund Univesity, Lund, Sweden as the Mitacs Globalink Research program.

Last but foremost, I give my deepest appreciation to my lovely companion Melika Shahriari for her patience and encouragement during this long journey. Finally but importantly, I express my humble gratitude to my parents, to whom I owe everything.

Table of Contents

List of Tables

List of Figures

Chapter 1

Introduction

1.1 Motivation for the Research

Mechanical Vibration can be defined as a motion that occurs fairly repeatedly after certain time intervals called *vibration period* [30]. It can happen freely or as a result of external excitation, leading to continuous energy transformation between kinetic and potential forms. It widely happens in industry and everyday life e.g. in vehicle suspension, rotary machines and civil structures.

Since vibrations can cause human discomfort, damage or unstability in structures, engineers usually try to minimize the oscillations which are considered to be "unwanted vibrations" [106]. However, in some cases like energy harvesting, engineering techniques are utilized to keep the oscillations within a decent range. With these case-specific requirements, mechanical and electromechanical elements involved in a vibration system are designed and controlled to show the best possible behavior [74].

Considerable amount of research and development has been conducted for improving the behaviour of vibration systems. Optimal design of linear elements with constant mechanical characteristics was the first attempt of engineers. Use of non-linear elements, inventing elements with tunable behaviour and active feedback control are examples of the extensive efforts made so far. The progress in this field has continued with emergence of new technologies. Advanced and low-cost micro-processing devices as well as efficient electrical power converters have created new opportunities to move from conventional systems to more sophisticated and intelligent products [2].

In conventional vibration systems, a combination of passive mechanical elements is used. In other words, all damping, stiffness and inertial components which are connected in a certain configuration, have constant values [89]. System elements are designed with considering the dynamics of the system as well as the characteristics of the input excitation [40].

Behavior of passive elements in a system may change as the result of aging or ambient conditions. Moreover, characteristics of input excitation may vary in terms of frequency and amplitude. In such scenarios, the performance of conventional systems deteriorates because there is no chance of re-tuning the parameters using a feedback control system [60].

In more advanced systems, multi-physical techniques are adopted for creating more intelligent vibration control. Magneto-rheology, electro-rheology and electromagnetism are good examples of the physical effects used for creating forces with a higher level of controllability in terms of damping and/or stiffness [64]. Moreover, adaptive control techniques can be used to make tuning of vibration systems autonomous [52]. The literature in the mentioned topics seems not to be fully developed, which motivates further studies that are provided in the coming parts of this thesis.

1.2 Background and Overview of the Present State of the Technology

1.2.1 Controllable mechanical impedance in vibration control actuators

In general, vibration systems consist of inertial, elastic and dissipative elements. Every mechanical component might show a combination of the mentioned characteristics, but it is common to model vibration systems as a number of lumped springs, lumped dampers and lumped masses [77]. In the linear cases, the terminal forces on a spring and a damper are proportional to the relative displacement and its derivative respectively, while the net force on a mass is proportional to the second derivative of the mass displacement. The constant relating force and displacement in a spring is called stiffness, while the ratio of damper force to its relative velocity is called damping constant. The combination of damping and stiffness in an element, which describes how a force generating element reacts to an input excitation can be called mechanical impedance [63].

As the common practice, linear stiffness is realized using compliant structures such as cantilever beams and coil springs. In this case, stiffness is mainly dependent on the geometry of the component and mechanical properties of the elastic material. As a result, the stiffness remains almost constant [65]. Similarly for dampers, the damping constant is dependent on geometry as well as the viscosity of the gas or fluid that creates the resistive force. Consequently in conventional systems, the damping factor is considered to be constant.

Apart from fixed-impedance elements, realizing variable-impedance for improving dynamic behaviour of vibration systems has been an interesting idea for engineers [117]. Changing damping and stiffness as control inputs of a system creates the opportunity to implement feedback control methods in different applications involving mechanical vibrations. It would also be possible to adapt a vibration system impedance according to its input behavior and input characteristics. Here, the overview of the present technologies for realization of variable mechanical impedance is divided to variable stiffness and variable damping as explained below.

Variable stiffness

In many applications, the stiffness coefficient, defined as the ratio of spring force to its displacement, is constant. However, *smart springs* that can be controlled to achieve desired stiffness coefficients have many potential advantages [101]. For instance, they can improve performance in robotic applications [32] or can be utilized in advanced vibration control and energy harvesters working under a wide range of frequencies [60, 111].

There are two major types of variable stiffness elements: active and semi-active devices. In the latter case, the inherent elastic behavior of mechanical elements is utilized for creating stiffness. Such systems can be operated under different operating points with different stiffness coefficients [102]. For example, in [103], a variable pre-load is provided for a nonlinear spring. Depending on the amount of the pre-load, the spring's operating point and its stiffness coefficient are controlled. Another example is changing the motion transmission ratio between the stiff element and the end-effector, which results in variable stiffness between input and output [47]. As another approach, physical properties of springs such as the number of active coils are changed to control the stiffness coefficient [34].

In active devices, on the other hand, an actuator is driven to mimic the behavior of a spring. Software control is used to calculate the amount of force that the actuator should create to synthesize the stiffness. A hydraulic system utilizing the above method was presented in [12].

Electromagnetic (EM) devices can be good choices for creating active stiffness elements because they are simple to design and control. Furthermore, it is possible to create bi-directional flow of power between the actuator and its power source such as a battery [104]. In other words, the mechanical power that the actuator receives can be converted into electric power and stored in a battery [109]. Likewise, if the actuator does positive mechanical work, the required power can be supplied by the battery. This flexibility in power flow management can be achieved with proper design or control of a shunt circuit and will be proven to be useful for synthesizing energy-storing mechanical elements such as springs.

Several researchers have investigated the design and control of shunt circuits for EM actuators. In [57], physical electrical elements were used in the shunt circuit to optimally change the impedance on the mechanical side. In [38], an electromagnetic actuator embedded in a mass-spring system was utilized, and the actuator was shunted with a constant resistor and capacitor to provide resonance to the system. The resistance and capacitance were selected to optimize the performance of the system as a vibration controller. In [19], the authors proposed use of two circuits in parallel with a coil-magnet actuator. Each circuit was a series RLC branch designed to control the first two modes of a cantilever beam. Constant RLC parameters were optimized for minimizing the vibration. In [122], an actuator was shunted in a mass-spring system with a series RLC circuit with constant parameters. They showed that this shunt circuit acts like an added mass-spring-damper mounted on the original mass, which could be used as a vibration absorber. They optimized the system parameters for optimal energy harvesting and vibration control at the same time. In [56], an H_2 optimal design approach was presented for designing an RLC shunted vibration absorber. Passive elements with constant values were used in the circuit. A review of the above works indicates that the use of electrical elements with constant parameters in the shunt circuit can be used for changing mechanical impedance of the actuator; however, these methods do not allow changing the system impedance instantaneously in real-time through software control.

Other approaches have utilized power electronics techniques to synthesize electrical elements in the shunt circuit. In [28], the authors have presented how variable impedances can be used for

synthesizing elements that do not physically exist (e.g., negative resistors or inductors). Achieving negative resistance and inductance in the shunt circuit of an EM actuator was presented in [115], aimed at multi-mode vibration control of a plate. The negative inductance canceled the internal inductance of the actuator while the negative resistance induced higher currents in the circuit. In [100], the authors proposed creating parallel RL shunt circuit to change damping and stiffness of a tunable vibration absorber. Their simulations proved efficacy of the system in controlling flexural vibration of a cylindrical cavity in a wide frequency range. Op-amps were suggested for creating the shunt impedance with no analysis provided regarding the power requirements of the system. In [61], the researchers used synthetic negative and positive resistance and capacitance to change the mechanical impedance in a vibration absorber. They showed that a synthetic shunt resistor and capacitor connected in series can create controllable stiffness and damping for the actuator. According to their calculations, this way of controlling mechanical impedance requires measurement of motion frequency. In the latter three works, the synthetic shunts are created using analog amplifiers. However, a major drawback of the above circuits is that they are not energy-efficient due to operation in the active linear amplifier mode.

To avoid use of linear amplifiers for current control, switching power converters have been suggested. A parallel RLC arrangement in shunt circuit of a pendulum energy harvester was presented in [62], where PWM switching of an H-bridge was used to control the shunt current. It was shown that a change of $\pm 10\%$ in the resonance frequency of the harvester was achieved by changing the circuit susceptance; however, the harvester performance was limited to a horizontally rocking motion as the source of excitation. A variable series RLC configuration was used in a single-phase coil-magnet energy harvester in [14]. They tuned the shunt impedance to maximize the power harvested from base excitation in a frequency sweep. Most recently, power generation and stability of an electromagnetic vibration energy harvester with a general load in the shunt circuit was presented in [73]. However, they did not focus on the power electronic circuit needed for creating the shunt load and did not discuss the stiffness and damping generated in the harvester [72].

As discussed above, there has been a growing interest in developing shunt control and optimization techniques for vibration control and energy harvesting [92, 16]. However, simple and practical ways of creating variable stiffness have not been investigated and analyzed in the recent literature.

Variable damping

It is common to model the behavior of a mechanical damper as a force proportional to velocity with a ratio called damping factor. Damping factor is approximately constant in conventional vibration systems; however, there are different ways to create variable damping to improve dynamic behavior of a system.

A well-developed method for achieving variable damping is the use of magneto-rheological (MR) fluids in hydraulic dampers. MR damping level can be changed in a certain range by applying a magnetic field in the fluid and changing its viscosity. The minimum damping in an MR damper is created when the field is turned off (off-state), while the maximum is limited by the fluid yield stress

(on-state). As a result, the dynamic range of an MR damper, defined as the ratio of maximum to minimum achievable damping, remains limited [114]. There exist other problems with MR dampers such as wearing of seals, sedimentation of particles, thickening of fluid and oxidation of particles. Moreover, long-term changes in MR dampers' behavior have been reported especially when they remain dormant for a long time [17].

It is possible to take advantage of electromagnetic (EM) effect to create damping effect [59]. It can be shown that using a resistive impedance in shunt circuit of a linear EM actuator results in mechanical damping, and changing the resistance varies the damping effect [42]. Creating variable stiffness with shunt control is a well-established method in the literature; however, creating damping levels that are high enough is a challenge in some applications [97].

Decreasing the external shunt resistance helps to induce larger currents in the actuator and create higher damping levels. To maximize the damping, it is possible to short-circuit the actuator, however, the internal resistance of the EM machine does not let the damping exceed a certain value, which might not be enough in some applications. The above issue has been a limiting factor against the application of EM dampers in vibration systems [57].

To increase maximum available damping in EM actuators, different approaches have been reported in the literature. In [121], an eddy current damper is optimized as a linear EM damper. In [97], the geometry and configuration of a multi-layer linear EM transducer were optimized for maximization of power density. Similar approaches were presented in [29] and [85].

In [69, 11, 49] magnetic lead screws were developed for trans-rotary motion conversion. Mechanical motion rectifiers such as two-leg mechanism [58], algebraic screw [82], rack and pinion [55, 112], scissor structure [67, 66], lead-screw [37, 109], and bevel gears [57] are commonly combined with gearhead motors in order to increase motion rectification factor. However, using high-ratio gearing adds unwanted inertia to the system which distorts the resulting force-velocity behavior expected from a vibration damper.

Another solution for increasing the damping coefficient in EM dampers is combining them with hydraulic systems. In [105], a linear EM motor was used in parallel with a passive hydraulic damper. In [23] and [7], linear motors were embedded inside passive shock absorbers. in [116, 28], hydraulic circuits were utilized as power transmission media. As the result, the hydraulic circuit contributes to creating damping forces, so the baseline passive damping remains constant and un-controllable, which limits the dynamic ratio of the damper.

The approach under focus in this study provides a solution in the electrical domain, which is creating a negative resistance in the shunt circuit. The negative resistance compensates some of the resistance already in the transducer circuit and decreases the overall shunt resistance. As the result, higher currents are induced in the circuit, creating larger forces. Yan et al. [110] created negative resistance in the shunt circuit of a coil-magnet actuator. The negative resistance was implemented with three operational amplifiers in a complicated circuit. The resulting shunt circuit leads to both EM damping and stiffness which cannot be controlled separately. In the most recent work, Stabile et al. [93] created negative resistance for control of spacecraft micro-vibration, and used a simpler circuit

with only one power amplifier. The negative resistance cannot be controlled during the experiments as its value is a function of the resistive components in the circuit.

1.2.2 Autonomous tuning for optimum performance

Realization of variable mechanical impedance would be an important step toward adaptive vibration systems; however, a control structure would be needed to provide the optimal values of mechanical impedance as the reference. In other words, it is needed to tune the damping and the stiffness as control variables to optimize the performance of a vibration system. The tuning can be achieved using model-based or model-free techniques. In the former, characteristics of the excitation should be measured, and the mechanical impedance should be tuned according to a model-based equation or look-up-table. This approach would not be robust against model uncertainties or changes in the plant parameters. Model-free tuning, on the other side, offers optimal tuning without dependency on the system model and is studied in this project.

The idea of self-tuning vibration control can be studied in different applications. This study focuses on two well-known problems in mechanical vibrations: Vibration Energy Harvesters (VEH) and Vibration Absorbers also known as Tuned Mass Dampers (TMD). In the former, the main objective is maximizing the harvested power while the latter is aimed at control of vibrations in civil structures.

Self-tuning for vibration energy harvesting

Vibration energy harvesters consist of an inertia element mounted on a compliant structure. An electromechanical transducer, such as a coil-magnet or electric motor, undergoes displacements as a result of the relative movements induced between the inertia element and its excited base. Roughly speaking, the best performance of a harvester is expected when it operates at the resonance frequency [76]. The efficacy of the power generation drops rapidly as the frequency of excitation deviates from that of resonance. As a solution, adaptive tuning of resonance frequency is suggested [86, 60, 95].

Adaptive tuning of resonance frequency can be achieved with mechanical or electrical approaches. In the former approach, mechanical properties of the structure such as dimensions [27], centre of gravity [108] and spring stiffness [18] are changed. In the electrical approach, the electrical load of the harvester is changed by controlling the shunt circuit [119].

Various strategies have been proposed for periodic tuning of energy harvesters [119]. Balato *et al.* [10] designed a Resonant Electromagnetic Vibration Energy Harvester (REVEH) for wireless sensor nodes in freight wagons. Their proposed system is connected to a buck converter that tunes the load voltage for maximum power tracking. However, a look-up table is used for tuning based on *a priori* knowledge of the harvester. A model-based feed-forward MPPT that tunes a resistive load was presented in [75].

A major disadvantage of model-based tuning methods is that they rely on harvester model or require a look-up table. The harvester model may be inaccurate or change over time because of

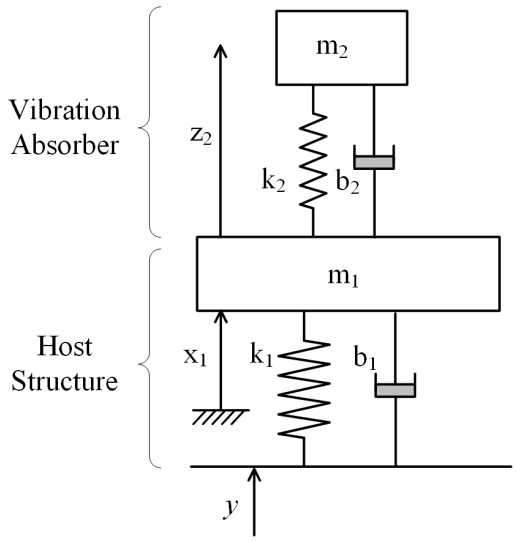

Figure 1.1: Schematic view of a vibration absorber on a host structure

aging or environmental conditions, which may affect performance of the harvester. Model-free self-tuning algorithms have been used in photovoltaic and wind energy conversion systems [79, 50] and vibration energy harvesters [22]. For instance, Gyorgy *et al.* [96] designed a simple Perturb and Observe (P&O) MPPT for a coil-magnet ultralow-power energy harvester. Leicht *et al.* [53] used a similar algorithm and implemented it for very low power applications.

In more advanced systems, both shunt resistance and inductance are tuned in the frequency domain for widening the frequency bandwidth. For example, in [15], a variable RLC circuit is used in the shunt of a vibration energy harvester, but no tuning method is suggested. Model-free tuning of shunt resistance and inductance requires applying a two-variable extremum seeking controller which has not been reported in the literature to the best of our knowledge.

Self-tuning for tuned mass dampers

Tuned mass dampers (TMDs), also known as harmonic absorbers, are mass-spring or mass-spring-damper systems that serve as vibration controllers. They can be mounted on excited host structures to minimize their vibration amplitude. Applications include vibration suppression in tall buildings, bridges and vehicles. The force induced in a TMD counteracts the exciting force of the main structure and decreases its vibration amplitude, especially at its resonance frequency [39]. Fig. 1.1 shows a conventional vibration absorber on a host structure.

An optimal TMD is designed based on the host structure's properties, excitation pattern, and control objectives. In the case that the input excitation has a single and known frequency, the TMD is tuned to have the same frequency as the excitation while its damping is minimized. However, the input frequency may not be exactly known when a TMD is designed, or it may vary over time. Moreover, the system parameters including those of the host structure or the TMD itself may change

because of aging or environmental conditions. As a result, the TMD would be out of tune for the designed structure and its performance may decrease significantly [60].

To address the above problem, different robust and adaptive TMDs have been proposed in the literature. For instance, in [8, 120] the authors utilize constant damping and stiffness values for a passive TMD based on an optimization criterion within a given frequency range. However, adaptive TMDs offer more flexibility since they can change their damping or stiffness according to the system's behavior or input characteristics.

Adaptive semi-active systems exhibiting variable damping, variable stiffness, or both have been proposed in TMDs [26, 13, 81]. However, active systems are faster and more flexible in creating independently and continuously variable damping and stiffness [60]. An active electromagnetic actuator with proper bi-directional shunt control has been reported to provide positive and negative damping and stiffness [100]. The aforementioned system can also remain self-powered in a range of operating points. Utilizing such an actuator in a passive TMD results in a hybrid TMD whose damping and stiffness can be tuned to minimize the host structure vibration under different input frequencies.

Finding the optimal impedance for an active TMD to achieve a desired vibration absorption is a remaining issue for further investigation. This impedance can be analytically calculated for each input frequency and provided for the system as an equation or look-up-table. This method is not robust to uncertainties and changes in structural characteristics because of being model-based and open-loop.

Model-free extremum-seeking controllers have been proposed with the ability to change a system's inputs and navigate its output to the extremum point [21, 20]. Sliding Mode Extremum-Seeking Controllers (SMESC) can be viable methods for application to self-tuning TMDs because of their fast and smooth convergence [98]. To this end, the objective would be to minimize the absolute displacement of the host structure. Damping and stiffness are chosen as tunable variables synthesized by proper control of the electromagnetic machine through power electronics.

1.3 Summary of Contributions and Outline of the Dissertation

Review of the literature about variable stiffness and variable damping elements shows that there are three major systems used for this purpose: semi-active, active and hybrid systems. A semi-active vibration controller is capable of changing at least one of the system parameters but unable to inject mechanical energy into the system [36]. More accurately, the power that they consume is spent only for changing damping, stiffness or inertance. In an active system, however, an externally powered force actuator is available to create forces calculated by a feedback controller. As the main advantage of active systems, they can potentially provide a high level of performance even if excitation characteristics or dynamics of a host structure change. This, on the down side, happens at the expense of increased power requirements and, in some cases, bulky and complicated systems.

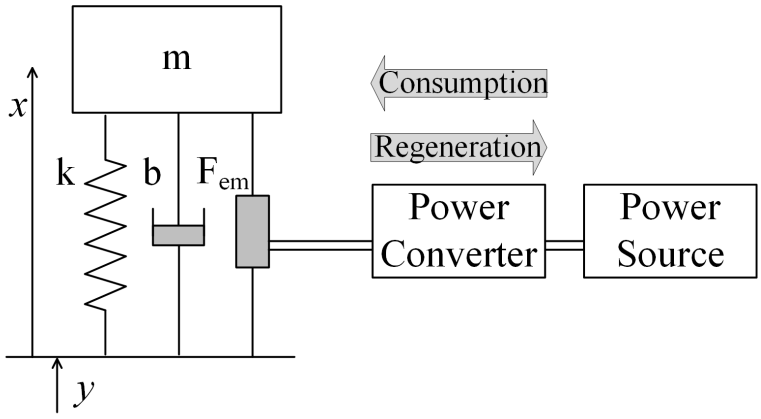

Figure 1.2: Schematic view of the adaptive vibration control structure used in this study

In hybrid systems, different kinds of force actuators including passive, semi-active and active elements are combined. This approach guarantees certain amount of damping to be always present in the system. As the result, the system is less likely to become unstable.

Hybrid systems including passive and active systems can provide more flexibility in creating forces. While passive elements provide a baseline impedance, an active force actuation can be added to improve the system performance. As another advantage, smaller actuators in terms of size and power requirement can be used since a portion of the control force is already provided by the passive elements.

Hybrid systems incorporating passive components as well as a regenerative force actuator (RFA) are selected to be subject of this study. The RFA is controlled to imitate mechanical impedance (damping and stiffness) whose characteristics can be controlled by software. This force is added to the forces created by the passive elements. Depending on the sign of the imitated mechanical impedance, the result will be a system with lower or higher damping and stiffness. Figure 1.2 shows the concept schematically.

In Fig. 1.2, parameters b and k show the passive damping and stiffness in the system respectively. m is the mass of the harvester (in case of vibration energy harvesting) or the mass of the tuned mass damper (in case of vibration absorption). F_{em} is the active force created by an Electro-Magnetic Actuator (EMA) which is connected to a power source through a bi-directional converter. If the actuator does positive mechanical work, the flow of power is from the source to the actuator, while the system becomes regenerative in the case of receiving positive mechanical power.

The passive component of the force created by the mechanical damper and spring can be written as

$$F_p = b\dot{x} + kx \tag{1.1}$$

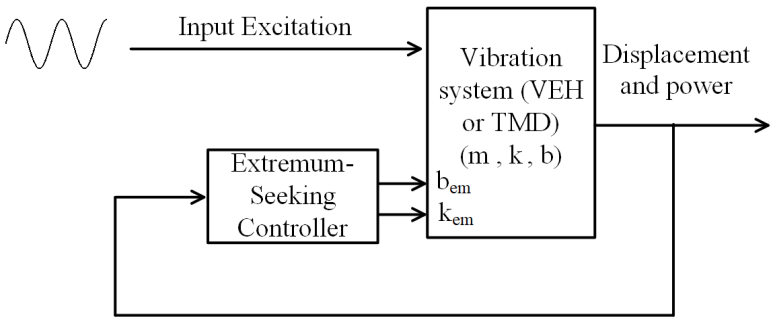

Figure 1.3: Self-tuning scheme for vibration systems

while the active force created by the EMA can be controlled to be equal to

$$F_{em} = b_{em}\dot{x} + k_{em}x. \tag{1.2}$$

The resulting force created by the hybrid actuator will be

$$F = (b + b_{em})\dot{x} + (k + k_{em})x. \tag{1.3}$$

Writing dynamic equation of the electromechanical system results in

$$m\ddot{x} + (b + b_{em})\dot{x} + (k + k_{em})x = -m\ddot{y} \tag{1.4}$$

while y is the displacement of the excited base. Equation (1.4) shows that the overall damping and stiffness of the system can be tuned by changing b_{em} and k_{em}.

It will be shown in Chapter 2 that creating forces described as (1.2) is equivalent with creating a synthetic shunt impedance for the actuator that includes positive or negative inductance and resistance. The shunt impedance can be synthesized by means of a bi-directional power converter controlled by a digital processor.

The scope of this thesis extends beyond realization of variable damping and stiffness in vibration systems. Effort is put to use this feature in two major mechanical vibraion applications: Vibration Energy Harvesting (VEH) and Tuned Mass Damping (TMD). For tuning the impedance of the vibration systems, extremum-seeking controllers are adopted to avoid model-based approaches. The general idea of the proposed scheme is provided in Fig. 1.3.

The next two Chapters provide the groundwork for realization of variable stiffness and damping using power electronic techniques. The rest of the thesis investigates application of extremum-seeking controllers in self-tuning vibration systems including energy harvesters and vibration absorbers. Summary of the contributions in each Chapter are provided below.

1.3.1 Chapter 2: Realization of Variable Stiffness and Damping with Power Electronics Shunt Control

This Chapter provides the groundwork upon which the rest of the thesis is developed. It is shown that a parallel RL configuration in the shunt circuit of an electromagnetic actuator makes the system behave like a parallel spring-damper configuration. To this end, a series negative RL circuit is created to cancel out the internal impedance of the electromagnetic machine, and the parallel part of the circuit is added to create variable damping and stiffness. The relationship between the shunt electrical impedance and the mechanical impedance of the actuator is mathematically derived. The voltage and power requirements for creating damping and stiffness are calculated as well. A power electronics boost converter is used for controlling the shunt circuit. The controller is implemented on a dSpace control hardware, and some experiments are conducted to verify the findings. The outcomes of this part of the project are now published in [42].

1.3.2 Chapter 3: Increasing the Maximum Achievable Damping with Active Shunt Control

This Chapter has a focus on variable damping in electromagnetic actuators. It is common to realize variable damping by creating a resistive shunt. It is shown that damping level is inversely proportional to the shunt resistance and can be maximized with short-circuiting the actuator shunt. In this case, the internal resistance of the machine limits the maximum damping. It is discussed that the maximum damping in this configuration might not be enough in some applications.

It is suggested to create a negative resistance element in the shunt circuit to cancel part of the internal resistance of the machine. Voltage and power requirements are studied, and experimental results are provided.

As another contribution, this Chapter suggests a novel mechanical design for axial electromagnetic actuators. Cylindrical cams also known as barrel cams are suggested as the mechanical motion rectifier for conversion between the rotary motion of the brushless DC motor and the axial motion needed in real applications. It is shown that the novel mechanism results in larger stroke-to-length ratios compared to the other reported mechanisms, which is desirable in some applications. The results of this study are under review by the IEEE Transactions on Mechatronics.

1.3.3 Chapter 4: Single-Variable Constrained Self-Tuning for Vibration Energy Harvesting

After realizing variable impedance in vibration systems, it is time to take advantage of the developed generic technology in engineering problems. One of the issues in vibration energy harvesting is tuning the harvester damping level when the frequency or amplitude of the excitation changes.

In this Chapter, the sliding mode extremum seeking controller is used for tuning the damping of an energy harvester. In this part of the study, self-tuning is limited to changing the damping, and stiffness is assumed to be constant. It is assumed that the harvester relative displacement should not

exceed a certain allowable level to avoid mechanical damage. To this end, a constraint is added to the extremum seeking controller using a penalty term in the objective function. Experimental results are provided to prove the efficacy of the suggested approach. The results of this study are published in [43].

1.3.4 Chapter 5: Multi-variable Self-tuning for Vibration Energy Harvesting

As a complement to Chapter 4, this Chapter investigates model-free self-tuning vibration energy harvesters with both variable damping and variable stiffness. An analytical model is used for calculating optimal damping, optimal stiffness and the maximum achievable harvested power.

To make the system self-tuning, a multi-variable extremum seeking controller is required. Multi-variable sliding mode extremum seeking is studied for this application. A new version of this controller is proposed, and it is shown that the novel controller results in better convergence to the extremum point. Experimental results are provided to demonstrate the performance of the system. This work is accepted for publication in the journal of Smart Materials and Structures.

1.3.5 Chapter 6: Constrained Self-tuning Vibration Absorbers with Variable Damping and Stiffness

By this Chapter, application of the generic innovation provided in Chapter 2 will have been explored for vibration isolation (Chapter 3) and vibration energy harvesting (Chapters 4 and 5). The last topic covered in this thesis is self-tuning vibration absorbers.

Sliding mode extremum seeking controller is used for self-tuning a tuned mass damper with variable damping and variable stiffness. A constraint is implemented on the power consumption of the TMD to avoid injection of any power to the system and minimize the risk of unstability. Simulations are used to investigate convergence of the algorithm to the optimum points. This study was presented in the 2nd IEEE Conference on Control Technology and Applications (CCTA 2018). It is now published in the conference proceedings [43].

1.3.6 Chapter 7: Conclusions and Suggestions for Future Works

The research outcomes and achievements will be summarized in this Chapter. General conclusions will be made based on the theories, simulations and experiments provided in the thesis. Some ideas that have been generated during the whole project but have not had a chance to be investigated will be suggested as future works.

Chapter 2

Realization of Variable Stiffness and Damping with Power Electronics Shunt Control

Although semi-active variable mechanical damping is a well-known and highly developed concept, creating efficient variable-stiffness has remained a challenge. In this Chapter, a brushless DC motor combined with a mechanical motion converter is utilized to synthesize the behavior of a mechanical spring. It is shown that synthesizing resistive and inductive elements in the motor shunt circuit can create damping and stiffness behaviors respectively. The actuator shunt is digitally controlled by a bi-directional boost converter that uses a sliding-mode algorithm. Using the proposed approach, the actuator can exhibit independent damping and stiffness effects in real-time. Analytic studies regarding the power requirements as well as the criteria for controller convergence are presented and verified through experimental studies.

2.1 Background

In this Chapter, the development of purely RL shunt electromagnetic actuators utilizing bi-directional power electronics circuits is presented. It is shown that an RL shunt, rather than an RLC one, is enough to create independent damping and stiffness terms. The resulting stiffness and damping terms have a decoupled relationship with the shunt inductance and resistance. This is unlike the series RL configuration [61], in which the resulting damping and stiffness terms are coupled with inductance and resistance of the shunt. Furthermore, the RL synthesis concept is extended to the 3-phase case, which makes it possible to use brushless DC (BLDC) motors and avoid friction and other limitations of brushed machines. The power requirements for creating damping, stiffness, and their combination is quantified in this paper along with the range of damping and stiffness values for self-powered operation of the EM actuator.

The organization of this Chapter is as follows. In Section 2.2, analytic developments are presented regarding the correspondence between shunt circuit impedance and actuator mechanical behavior. The power required for creating a synthetic parallel RL configuration in the shunt circuit is

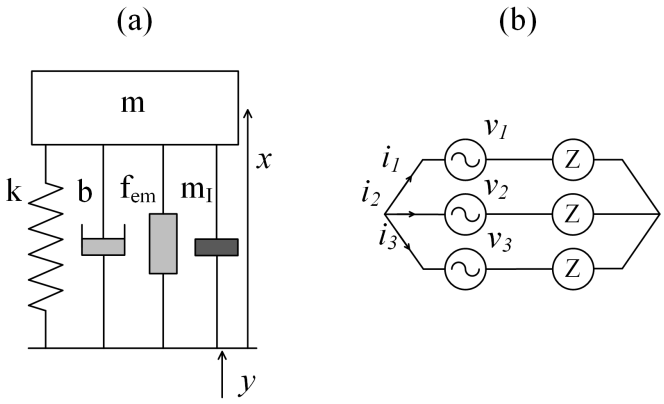

Figure 2.1: (a) mass-spring-damper structure with an EM actuator (b) shunt circuit of the 3-phase actuator

obtained along with power efficiency. The results are compared with non-regenerative shunt control systems. In Section 2.3, a stability analysis for the sliding mode controller is provided. Experimental results including the actuator performance in a mass-spring-damper system are presented in Section 2.4.

2.2 Theory

2.2.1 Synthetic Shunt Impedance

Consider a mass-spring-damper along with a three-phase brushless actuator shown in Fig. 2.1(a). The actuator can be modeled as a linear electromagnetic force generator in parallel with an inerter element. The electric machine's terminals are connected to three equal impedances connected in a star configuration (Fig. 2.1(b)). The phase back emf voltages can be written as

$$\begin{cases} v_1 = V_m \sin(\theta - \frac{2\pi}{3}) \\ v_2 = V_m \sin(\theta) \\ v_3 = V_m \sin(\theta + \frac{2\pi}{3}) \end{cases} \tag{2.1}$$

where V_m is the voltage amplitude.

For a single harmonic motion, in the frequency domain, we can write

$$\hat{I} = \frac{\hat{V}}{Z}. \tag{2.2}$$

where $\hat{I}$ and $\hat{V}$ are the current and voltage phasors, and Z is the overall impedance of the shunt circuit including the actuator internal resistance and inductance.

If the overall impedance is designed to be purely resistive, the relationship between the electromagnetic actuator force f_{em} and its speed $\dot{x}$ can be written as

$$f_{em} = \frac{{c_{em}}^2}{R}\dot{x}, \tag{2.3}$$

where c_{em} is the electromechanical coupling constant of the actuator defined as the ratio between force f_{em} and current $i(t)$. According to (2.3), if the shunt circuit is completely resistive, the machine behaves like a mechanical viscous damper with damping constant given by

$$b_{em} = \frac{{c_{em}}^2}{R}. \tag{2.4}$$

If the shunt circuit is purely inductive, the actuator force is calculated as follows

$$f_{em} = \frac{{c_{em}}^2}{L}x, \tag{2.5}$$

where L is the overall inductance of the shunt circuit. Equation (2.5) shows that an inductive shunt circuit would create a mechanical stiffness given by

$$k_{em} = \frac{{c_{em}}^2}{L}. \tag{2.6}$$

To combine EM damping and stiffness effects, a combination of resistive and inductive elements in the shunt circuit should be used. If a resistor and inductor are connected in parallel, the current generated in the circuit is given by

$$i(t) = \frac{1}{L}\int v(t)dt + \frac{1}{R}v(t), \tag{2.7}$$

and the actuator force is calculated as

$$f_{em} = k_{em}x + b_{em}\dot{x}. \tag{2.8}$$

For this case, the shunt circuit is demonstrated in Fig. 2.2.

It should be noted that the circuit has an internal resistance r_{in} and an internal inductance L_{in}. This means that for creating the parallel configuration of Fig. 2.2, we first need to cancel the internal shunt RL circuit with a negative resistor $-r_{in}$ and negative inductor $-L_{in}$. The resulting circuit is shown in Fig. 2.3.

2.2.2 Power Analysis

To calculate the power requirements for creating the external impedance shown in Fig. 2.3, the power exchange in the boundaries of Z_{ex} should be calculated. Assuming a balanced circuit, the

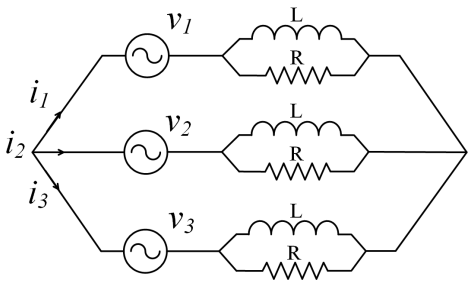

Figure 2.2: Shunt circuit configuration for creating both damping and stiffness with an electromechanical actuator

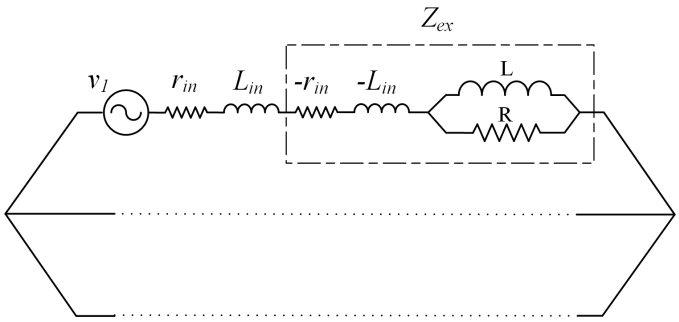

Figure 2.3: Complete shunt circuit for combining electromechanical damping and stiffness

instantaneous power associated with $-r_{in}$ and R is calculated as follows

$$p(t) = \{\frac{{v_1}^2}{R} + \frac{{v_2}^2}{R} + \frac{{v_3}^2}{R}\} - \{r_{in}{i_1}^2 + r_{in}{i_2}^2 + r_{in}{i_3}^2\} \tag{2.9}$$

Using (2.1), we have

$$p(t) = 1.5\{\frac{v(t)^2}{R} - r_{in}i(t)^2\}. \tag{2.10}$$

The actuator is intended to be used as a spring element in a linear vibration system shown in Fig. 2.1(a). Consequently, it can be assumed that the displacement $x(t)$ and voltage $v(t)$ have harmonic behavior described as follows

$$x(t) = X\sin(\omega(t)), \tag{2.11}$$

$$v(t) = V\cos(\omega(t)) \tag{2.12}$$

where ω is the harmonic vibration frequency, X is the actuator displacement amplitude, and V is the voltage amplitude that can be calculated as a function of actuator displacement and electromechanical constant, i.e.,

$$V = X\omega c_{em}. \tag{2.13}$$

Thus the current can be expressed as

$$i(t) = I\cos(\omega(t) + \phi) \tag{2.14}$$

where ϕ is the phase difference between the emf voltage and current. Using (2.7), the relationship between voltage and current amplitudes is as follows

$$I = \frac{V}{\omega}\sqrt{\frac{1}{L^2} + \frac{\omega^2}{R^2}}. \tag{2.15}$$

Considering (2.10) and using (2.12) to (2.15), the average power can be calculated as follows

$$P_{avg} = \int_0^{\frac{2\pi}{\omega}} p(t) = \frac{3}{4}X^2\left\{\omega^2(\frac{{c_{em}}^2}{R} - \frac{r_{in}{c_{em}}^2}{R^2}) - \frac{r_{in}{c_{em}}^2}{L^2}\right\} \tag{2.16}$$

in which the positive and negative values indicate energy regeneration and consumption, respectively. The first two terms in (2.16) show the power exchange as a result of resistance R, and the last term corresponds to the power consumption for creating inductance L. Using (2.4) and (2.6), the expression for power can be rewritten as a function of damping b_{em} and stiffness k_{em} as follows

$$P_{avg} = \frac{3}{4}X^2\left\{\omega^2(b_{em} - \frac{r_{in}}{{c_{em}}^2}{b_{em}}^2) - \frac{r_{in}}{{c_{em}}^2}{k_{em}}^2\right\}. \tag{2.17}$$

Equation (2.17) provides useful information about the power exchange for creating the external impedance. It is possible to split the equation into two separate expressions P_b and P_k which describe the power regeneration due to damping and stiffness, respectively, i.e.,

$$P_b = \frac{3}{4}X^2\omega^2(b_{em} - \frac{r_{in}}{{c_{em}}^2}{b_{em}}^2) \tag{2.18}$$

and

$$P_k = -\frac{3}{4}X^2\frac{r_{in}}{{c_{em}}^2}{k_{em}}^2. \tag{2.19}$$

According to (2.18), the power exchange for creating damping can take both positive and negative values. If $0 < b_{em} < \frac{c_{em}^2}{r_{in}}$, damping is regenerative, which can be used for energy harvesting from mechanical vibrations. If $b_{em} > \frac{c_{em}^2}{r_{in}}$, damping becomes energy consuming. The same thing happens for negative values of b_{em} which is justified due to the fact that a negative damper is an energy consuming component. Fig. 2.4 shows the average power as a function of EM damping.

In contrast, (2.19) shows that creating electromechanical stiffness is always energy consuming. The power is linearly proportional to r_{in} and has a quadratic relationship with k_{em}. Fig. 2.5 shows P_k as a function of k_{em}.

As a special case, it is possible to keep the system self-powered through balancing P_b and P_k. In other words, one can regenerate power by creating positive damping and consume the regenerated power for changing the stiffness. To this end, (2.17) is set equal to zero, and the maximum self-

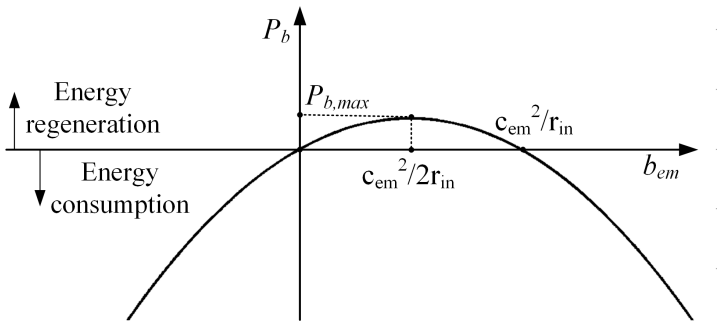

Figure 2.4: Power regeneration for creating electromechanical damping in the actuator

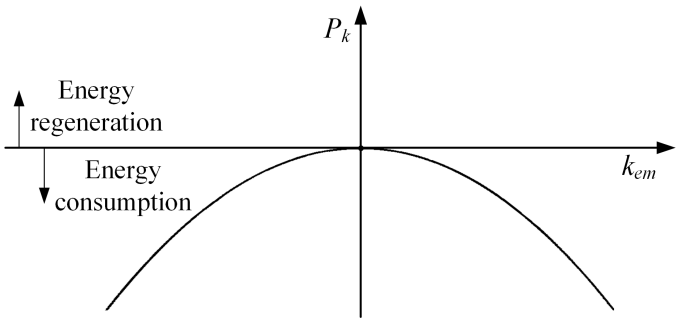

Figure 2.5: Power regeneration for creating electromechanical stiffness in the actuator

powered stiffness can be obtained as follows

$$max|k_{em}| = c_{em}\omega\sqrt{\frac{b_{em}}{r_{in}} - \frac{{b_{em}}^2}{{c_{em}}^2}}. \tag{2.20}$$

Fig. 2.6 summarizes the above discussion. According to this figure, if the EM damping b_{em} is in the regenerative range ($0 < b_{em} < \frac{c_{em}^2}{r_{in}}$), a range of positive and negative values for k_{em} can be obtained which keeps the system self-powered. In other words, power is regenerated if the operating point is inside the oval shape (Fig. 2.6).

2.2.3 System Efficiency

In this Section, efficiency of the system for generating an electromagnetic stiffness k_{em} is discussed. It is assumed that the external resistance R is infinitely large (open circuit), i.e., the EM damping is equal to zero ($b_{em} = 0$).

The energy transfer efficiency is commonly defined as the ratio of the desirable transferred energy to the whole energy consumed from a source. In this Chapter, we define the efficiency for stiffness generation by obtaining the average exchanged power regardless of the direction of energy flow. To this end, the absolute value of mechanical work for a spring element in one harmonic cycle

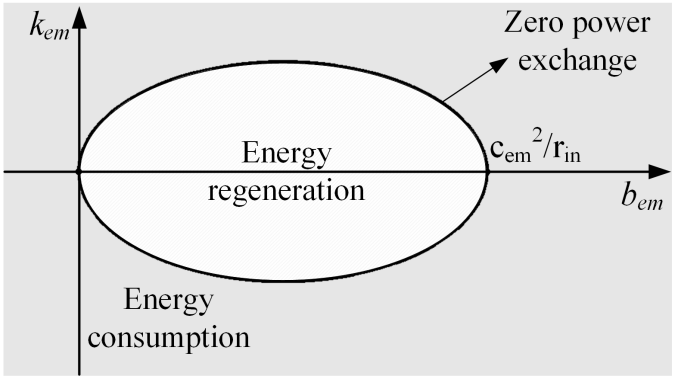

Figure 2.6: EM stiffness range for self-powered operation of damper

can be expressed as follows

$$P_{ideal} = \int_0^{\frac{2\pi}{\omega}} |kx(t)\dot{x}(t)|dt = \frac{\omega}{\pi} kX^2, \tag{2.21}$$

where P_{ideal} is the power that is ideally exchanged in the presence of stiffness k, and ω is the frequency of its harmonic motion with amplitude X.

Now let us define the power efficiency for generating stiffness as follows

$$\eta = \frac{P_{ideal}}{P_{ideal} + P_{loss}} \tag{2.22}$$

where P_{ideal} is the power to generate ideal stiffness, and P_{loss} is the power loss for generating stiffness k. With the above definition, if a system requires no power for generating stiffness ($P_{loss} = 0$), its efficiency is 100%, whereas higher values of P_{loss} result in lower η.

Equation (2.22) is used for calculating power efficiency of the method proposed. In this case, the term P_{loss} is equal to the expression provided in (2.19) . As a result, the power efficiency for generating stiffness with RL shunt can be written as

$$\eta_{RL} = \frac{1}{1 + \frac{3}{4}\frac{\pi}{\omega}(\frac{r_{in}}{{c_{em}}^2})k_{em}}. \tag{2.23}$$

Next, let us advantage the performance of the proposed approach over active systems with a uni-directional power flow (non-regenerative). To this end, we have to calculate the power requirements with the assumption that no energy can be recovered back from the actuator. In other words, instead of calculating the power loss only in the internal resistor r_{in}, one should calculate the power exchange by the externally created impedance Z_{ex} (Fig. 2.3). The power for the stiffness generation case ($R = \infty, L \neq 0$) can be calculated by multiplying the voltage and current in the boundaries of Z_{ex}, i.e.,

$$p(t) = 1.5\big(v(t) - r_{in}i(t) - L_{in}\frac{di(t)}{dt}\big)\big(i(t)\big). \tag{2.24}$$

Rewriting the power in terms of the EM stiffness k_{em} and actuator displacement $x(t)$ results in

$$p(t) = 1.5\Big((k_{em} - \tfrac{L_{in}}{{c_{em}}^2}{k_{em}}^2)x(t)\dot{x}(t) - \tfrac{r_{in}}{{c_{em}}^2}{k_{em}}^2 x^2(t)\Big). \tag{2.25}$$

Assuming a sinusoidal motion $x(t) = X\sin(\omega t)$, the power can be written as

$$p(t) = 1.5\Big((k_{em} - \tfrac{L_{in}}{{c_{em}}^2}{k_{em}}^2)\tfrac{1}{2}X^2\omega\sin(2\omega t) - \tfrac{r_{in}}{{c_{em}}^2}{k_{em}}^2 X^2\sin^2(\omega t)\Big), \tag{2.26}$$

where the first term with $\sin(2\omega t)$ is a sinusoidal function with frequency twice the motion frequency, and the second term is always negative because of the term $-\sin^2(\omega t)$. If the system is capable of providing a bi-directional power exchange, the first term can be integrated over positive and negative values resulting in zero. Integrating the second term results in (2.19), which was already calculated with the same assumptions.

To obtain the power exchange for a non-regenerative system, the first term in (2.26) should not be integrated over positive values since the system is not able to regenerate any power. Integrating the whole expression over negative values results in

$$P_{loss} = \frac{3}{4}\Big(X^2\frac{r_{in}}{{c_{em}}^2}{k_{em}}^2 + \frac{\omega}{\pi}X^2|k_{em} - k_{em}\frac{L_{in}}{{c_{em}}^2}|\Big). \tag{2.27}$$

Stiffness generation efficiency can now be calculated using (2.22) as

$$\eta_{active} = \frac{1}{1 + \frac{3}{4}\frac{\pi}{\omega}(\frac{r_{in}}{{c_{em}}^2})k_{em} + \frac{3}{4}|1 - \frac{L_{in}}{{c_{em}}^2}|}. \tag{2.28}$$

Comparing (2.28) to (2.23), it can be inferred that efficiency of an active-only system is less than that of an active-regenerative system, η_{RL}. To have a better sense of numerical values for efficiency, let us calculate η_{RL} and η_{active} for $k_{em} = 3000N/m$ when the excitation frequency is $6Hz$. Using parameters of the experimental system in this study, the efficiency for active-regenerative stiffness is $\eta_{RL} = 66.8\%$ while generating active-only stiffness yields $\eta_{active} = 44.5\%$. The difference between the two efficiencies depends on the parameters of the system and excitation frequency; however, we can claim that η_{RL} is always larger than η_{active} because of the third positive term in the denominator of η_{active}. This can be explained using the fact that an active-regenerative system (RL shunted actuator) recovers some of the mechanical energy that it provides for the dynamic system, while the active-only system only injects power without regenerating electrical energy.

2.3 Power Electronics Control

For creating the shunt circuit in Fig. 2.3, one should consider the desired impedance Z_{ex} in the shunt circuit and calculate the desired current $i_d(t)$. Thus the desirable shunt impedance Z_{ex} is realized by controlling the motor current. In this study we utilize a bi-directional 3-phase boost converter

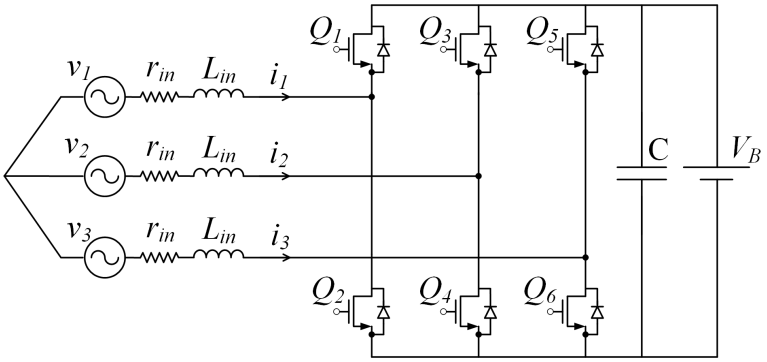

Figure 2.7: 3-phase boost converter for controlling the circuit current

consisting of 6 switches Q_1 to Q_6 which take complementary states in each pair as shown in Fig. 2.7.

Following [88], the circuit equations can be written as follows

$$\begin{cases} \frac{di_1}{dt} = -\frac{r_{in}}{L_{in}} i_1 + \frac{1}{3L_{in}}(2v_1 - v_2 - v_3) \\ -\frac{V_B}{6L_{in}}(2u_1 - u_2 - u_3) \\ \\ \frac{di_2}{dt} = -\frac{r_{in}}{L_{in}} i_2 + \frac{1}{3L_{in}}(2v_2 - v_1 - v_3) \\ -\frac{V_B}{6L_{in}}(2u_2 - u_1 - u_3) \\ \\ \frac{di_3}{dt} = -\frac{r_{in}}{L_{in}} i_3 + \frac{1}{3L_{in}}(2v_3 - v_2 - v_1) \\ -\frac{V_B}{6L_{in}}(2u_3 - u_2 - u_1) \end{cases} \tag{2.29}$$

or, in the matrix form, given by

$$\frac{d}{dt}\mathbf{i} = -\frac{r_{in}}{L_{in}}\mathbf{i} + \frac{1}{3L_{in}}\mathbf{B}\mathbf{v} - \frac{V_B}{6L_{in}}\mathbf{B}\mathbf{U} \tag{2.30}$$

where

$$\mathbf{i} = [i_1, i_2, i_3]^T, \tag{2.31}$$

$$\mathbf{B} = \begin{bmatrix} 2 & -1 & -1 \\ -1 & 2 & -1 \\ -1 & -1 & 2 \end{bmatrix}, \tag{2.32}$$

$$\mathbf{v} = [v_1, v_2, v_3]^T, \tag{2.33}$$

and

$$\mathbf{U} = [u_1, u_2, u_3]^T. \tag{2.34}$$

Note that u_i's can take values from the set $\{1, -1\}$, in which $u_i = 1$ corresponds to turning on only the high side switch in leg i, and $u_i = -1$ turns on the low side switch.

The control objective is to impose a desired current vector $\mathbf{i_d}$ in the BLDC motor phases. The vector can be written as

$$\mathbf{i_d} = i_d(t)\mathbf{S(t)} \tag{2.35}$$

while

$$\mathbf{S(t)} = \begin{bmatrix} \sin(\omega_m t - 2\pi/3) \\ \sin(\omega_m t) \\ \sin(\omega_m t + 2\pi/3) \end{bmatrix}. \tag{2.36}$$

In the above equations, $i_d(t)$ can be calculated using (2.7) and ω_m is the motor angular speed.

Now let us consider the following sliding surface

$$\boldsymbol{\sigma} = \mathbf{i(t)} - \mathbf{i_d(t)}. \tag{2.37}$$

To design a controller that guarantees attractiveness of the sliding surface (2.37), a positive-definite Lyapunov function is introduced as follows

$$V_L = \frac{1}{2}\boldsymbol{\sigma^T}\boldsymbol{\sigma}. \tag{2.38}$$

The time derivative of the Lyapunov function leads to

$$\dot{V}_L = \boldsymbol{\sigma^T}\dot{\boldsymbol{\sigma}} = \boldsymbol{\sigma^T}(-\frac{r_{in}}{L_{in}}\mathbf{i} + \frac{1}{3L_{in}}\mathbf{Bv} - \frac{V_B}{6L_{in}}\mathbf{BU} - \dot{\mathbf{i}}_\mathbf{d}). \tag{2.39}$$

From (2.37), we have $\mathbf{i} = \boldsymbol{\sigma} + \mathbf{i_d}$, so

$$\begin{aligned} \dot{V}_L &= \boldsymbol{\sigma^T}(-\tfrac{r_{in}}{L_{in}}\boldsymbol{\sigma} - \tfrac{r_{in}}{L_{in}}\mathbf{i_d} + \tfrac{1}{3L_{in}}\mathbf{Bv} - \tfrac{V_B}{6L_{in}}\mathbf{BU} - \dot{\mathbf{i}}_\mathbf{d}) \\ &\leq \boldsymbol{\sigma^T}(-\tfrac{r_{in}}{L_{in}}\mathbf{i_d} + \tfrac{1}{3L_{in}}\mathbf{Bv} - \tfrac{V_B}{6L_{in}}\mathbf{BU} - \dot{\mathbf{i}}_\mathbf{d}). \end{aligned} \tag{2.40}$$

Let us now define matrix ψ as

$$\boldsymbol{\psi} = -\frac{r_{in}}{L_{in}}\mathbf{i_d} + \frac{1}{3L_{in}}\mathbf{Bv} + \frac{V_B}{6L_{in}}\mathbf{J_{3\times 3}U} - \dot{\mathbf{i}}_\mathbf{d} \tag{2.41}$$

where $\mathbf{J_{3\times 3}}$ is a 3×3 matrix with all elements equal to 1. Referring to (2.40), we can write

$$\dot{V}_L \leq \boldsymbol{\sigma^T}\boldsymbol{\psi} - \boldsymbol{\sigma^T}\frac{V_B}{2L_{in}}\mathbf{U} \tag{2.42}$$

Using the following control law

$$\mathbf{U} = sign(\boldsymbol{\sigma}), \tag{2.43}$$

we have

$$\dot{V}_L \leq \boldsymbol{\sigma}^{\boldsymbol{T}}\boldsymbol{\psi} - \boldsymbol{\sigma}^{\boldsymbol{T}}\tfrac{V_B}{2L_{in}} sign(\boldsymbol{\sigma}) \leq \sum_{i=1}^{3} |\sigma_i||\psi_i| - \tfrac{V_B}{2L_{in}} \sum_{i=1}^{3} |\sigma_i|$$
$$\leq max(\psi_i) \sum_{i=1}^{3} |\sigma_i| - \tfrac{V_B}{2L_{in}} \sum_{i=1}^{3} |\sigma_i| = (max(\psi_i) - \tfrac{V_B}{2L_{in}}) \sum_{i=1}^{3} |\sigma_i|, \tag{2.44}$$

where

$$max(\psi_i) = max\Big(- \tfrac{r_{in}}{L_{in}} i_{d,i}(t) + \tfrac{1}{3L_{in}}\big(3v_i(t) - \sum_{i=1}^{3} v_i(t)\big) + \tfrac{V_B}{6L_{in}} \sum_{i=1}^{3} u_i - \dot{i}_{d,i}(t)\Big), \tag{2.45}$$

in which c_r is the motion rectification factor between the linear and rotational motion of the EM actuator.

To achieve system stability, the term $(max(\psi_i) - \frac{V_B}{2L_{in}})$ in (2.44) should remain negative. Considering (2.12)–(2.15) and (2.45) the final stability condition can be written as

$$V_B > 3(Xc_{em}\omega) \times \Big(1 + L_{in}\big(\tfrac{r_{in}}{L_{in}} + c_r X\omega + \omega\big)\sqrt{\tfrac{1}{L^2\omega^2} + \tfrac{1}{R^2}}\Big). \tag{2.46}$$

Equation (2.46) indicates the DC supply voltage required for creating the inductance L and resistance R when using an EM actuator. Using (2.4) and (2.6), it is possible to rewrite (2.46) in terms of electromagnetic damping and stiffness as

$$V_B > 3(Xc_{em}\omega) \times \Big(1 + \big(\tfrac{r_{in}}{\omega} + L_{in}c_r X + L_{in}\big)\tfrac{1}{{c_{em}}^2}\sqrt{k_{em}^2 + b_{em}^2\omega^2}\Big), \tag{2.47}$$

which can be used to determine if the circuit can create a combination of damping b_{em} and stiffness k_{em} when the displacement amplitude is X and the vibration frequency is ω. It can also be concluded that creating large values of b_{em} and k_{em} would require a large DC voltage. This is already expected since creating high damping and stiffness requires high shunt currents, which results in higher voltage requirements. On the other hand, if b_{em} and k_{em} are small enough, the equation is reduced to

$$V_B > 3Xc_{em}\omega, \tag{2.48}$$

which is valid when lower currents are created in the actuator shunt circuit.

2.4 Experiments

The actuator used in this study is a combination of a 3-phase brushless DC motor and a two-leg mechanism for converting linear motion into rotary motion. This combination, introduced in [58], can be used for creating forces using a rotational electric motor (Fig. 2.8). The relationship between the rotary and linear displacement of the two plates in the mechanism is given by [58]

$$\delta = \sqrt{l^2 - 2a^2(1 - \cos\theta)}, \tag{2.49}$$

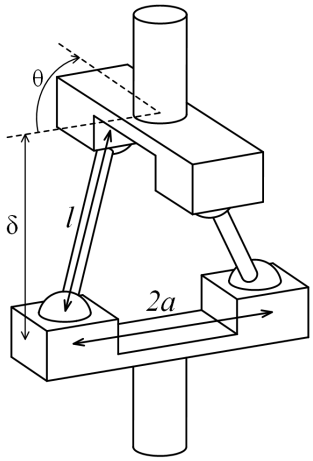

(a)

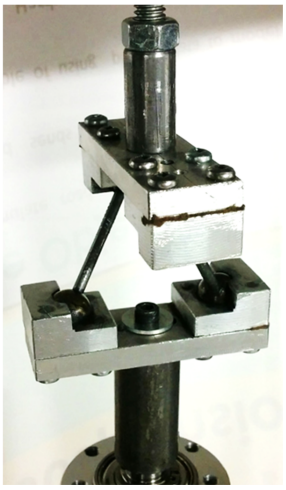

(b)

Figure 2.8: Two-leg mechanism for motion conversion (a) Schematic (b) Prototype.[78]

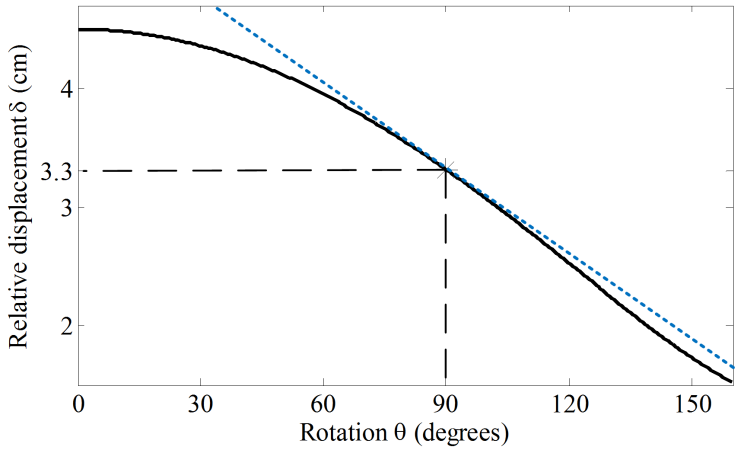

Figure 2.9: Relationship between the mechanism rotation (θ) and displacement (δ)

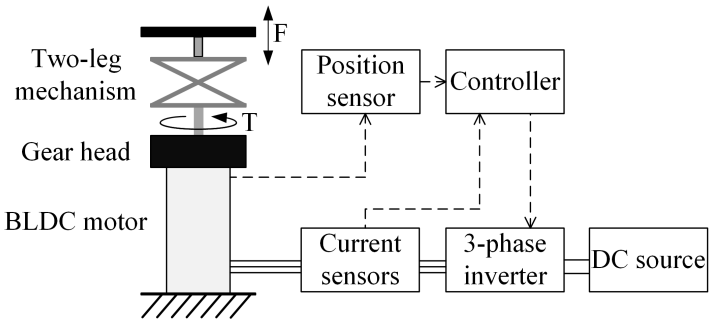

Figure 2.10: The schematic view of the electromechanical actuator control

where a is equal to half of the mechanism width, and l is its length. From (2.49), the mechanism has nonlinearity as plotted in Fig. 2.9. The test set-up equilibrium point corresponds to an angular position of $90°$. For small displacements (less than $1cm$), the linearized relationship can be written as follows

$$\dot{\delta} = -\frac{a^2 \sin(\theta)}{\sqrt{l^2 - 2a^2(1-\cos\theta)}}\bigg|_{\theta=90°} \dot{\theta}. \tag{2.50}$$

The mechanism explained above was connected to a 3-phase brushless DC motor with a gear-head added to the motor to increase the electromechanical coupling. The resulting system is shown in Fig. 2.10.

The motor used in the experiments was a Maxon EC-MAX 283873 brushless motor equipped with Hall sensors. Encoder HEDS-5540A14 from the Broadcom was connected to the motor for accurate displacement measurements. For current sensing, the voltage drop across a $25m\Omega$ shunt resistor was amplified using AMC1100 fully-differential isolation amplifier. The controller was implemented on a dSpace real-time control hardware with control loop frequency of $f_s = 50kHz$, and a TI DRV8305 driver board was used as a full-bridge converter circuit. All system parametric values are provided in Table 2.1.

Table 2.1: Parameter values of the test setup for the smart spring

Parameters	Value
mechanical stiffness, k	$12000N/m$
mechanical damping, b	$40N.s/m$
mass, m	$8.7kg$
inertance, m_I	$1.3kg$
motor phase resistance, r_{in}	4.9Ω
actuator inductance, L_{in}	$2.15mH$
electromechanical coupling constant, c_{em}	$43N/A$

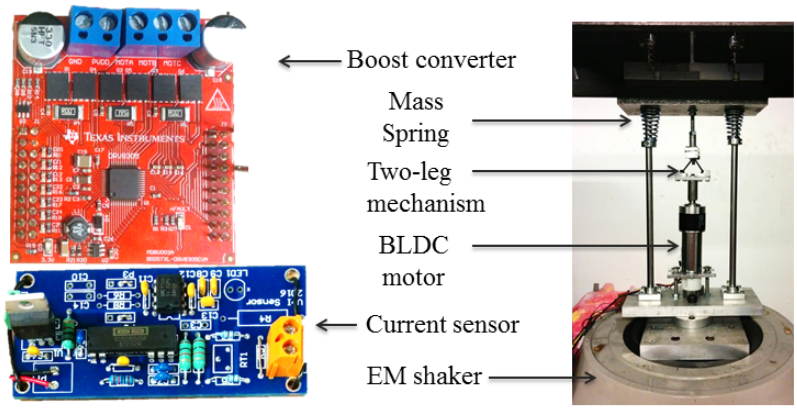

Figure 2.11: The whole test setup for the smart spring experiments

As shown in Fig. 2.1, the actuator was designed and controlled as a part of a linear vibration system. Hence, a mass-spring system was used as the test setup. The whole structure was put on an electromagnetic shaker. Fig. 2.11 shows the complete setup.

The Simulink file parameters uploaded on the hardware were used for changing the system's emulated damping and stiffness terms independently. This makes it possible to change the damping and stiffness terms in real-time using digital control of the power electronics interface. The system was shaken from its base in the range of frequencies from 4 to 8 Hz, and its relative displacement and regenerated power were measured.

In the first experiment, damping levels equal to 0, 50, 100 and 600 Ns/m were created. Fig. 2.12 shows the system non-dimensional relative displacement for the frequency sweep. As seen in this figure, relative displacement values around the system's resonance frequency ($f = 5.5Hz$) become smaller when the damping values increase. At higher frequencies, the values get closer to 1, which is expected from a linear mass-spring-damper system.

To observe the effect of damping level on power regeneration, Fig. 2.13 was obtained. According to this figure, creating no damping leads to zero energy exchange between the actuator and the power source ($b_{em} = 0Ns/m$). Increasing the damping takes the system to the energy regenerative state

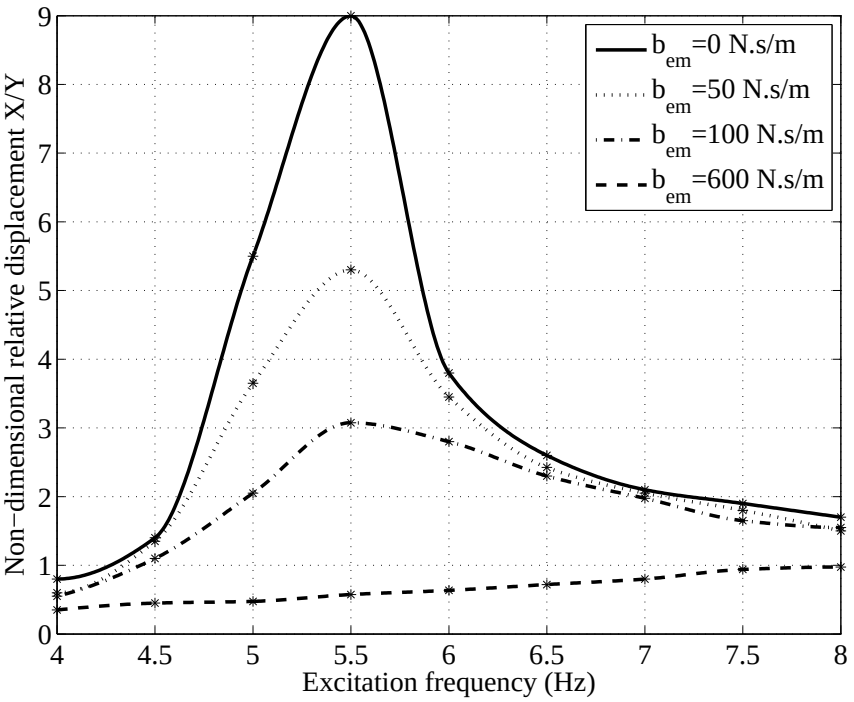

Figure 2.12: System non-dimensional relative displacement in the frequency sweep

($b_{em} = 50$ or $100Ns/m$). Higher damping values can exceed the maximum available self-powered damping and make the system energy consuming ($b_{em} = 600Ns/m$). This is commensurate with the theory provided in Section 2.2. Creating damping is energy regenerative in a certain range of damping, which corresponds to creating positive synthetic resistance in the shunt circuit. Creating damping higher than $\frac{c_{em}^2}{r_{in}}$ is equivalent to creating negative resistance in the shunt circuit and leads to energy consumption.

Different positive and negative stiffness values were created while the electromechanical damping was kept equal to zero. Relative displacement of the system is shown in Fig. 2.14. As seen in this figure, the natural frequency of the host stucture is approximately $5.5Hz$ (case $k_{em} = 0N/m$). Adding positive electromechanical stiffness ($k_{em} = 3kN/s$ and $k_{em} = 6kN/s$) increased the resonance frequency to 6 and $6.5Hz$, respectively. Negative electromechanical stiffness ($k_{em} = -3kN/s$), on the other hand, decreased the resonance frequencies to $5Hz$. Creating stiffness $k_{em} = -6kN/s$ resulted in a response with a peak between 3 and $4Hz$ which is in accordance with the expected theoretical resonance frequency of $3.5Hz$. The results show that variable stiffness is obtained with proper control of the shunt circuit current. Consequently, the system is capable of tuning its resonance frequency toward both lower and higher values. The results are in accordance with the behavior predicted in theory.

The theoretical analysis in Section 2.2 indicates that creating synthetic stiffness is energy consuming. To verify the claim, regenerated power in the recent experiment was measured and plotted in Fig. 2.15. According to the above figure, the required power is negative meaning that energy is

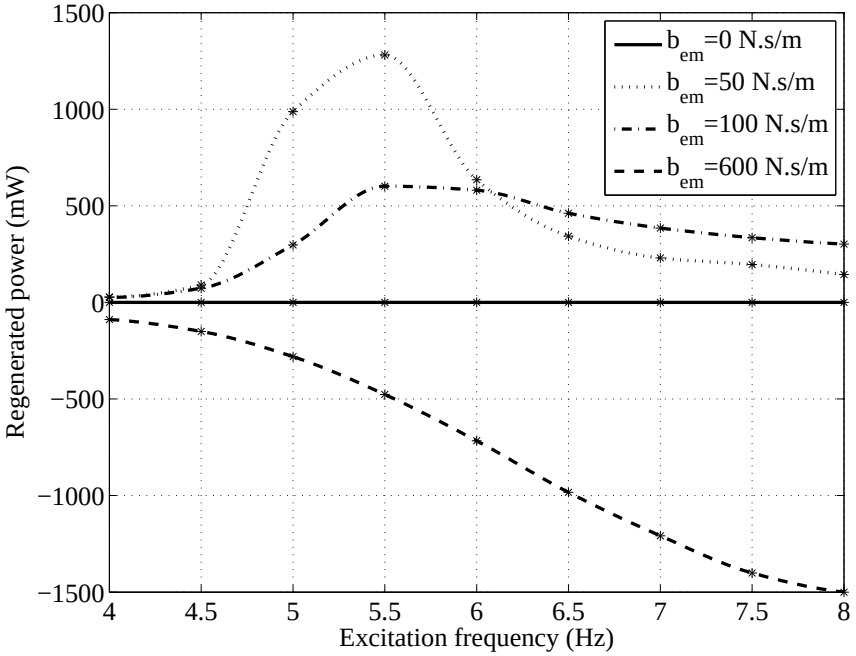

Figure 2.13: System power regeneration in the frequency sweep

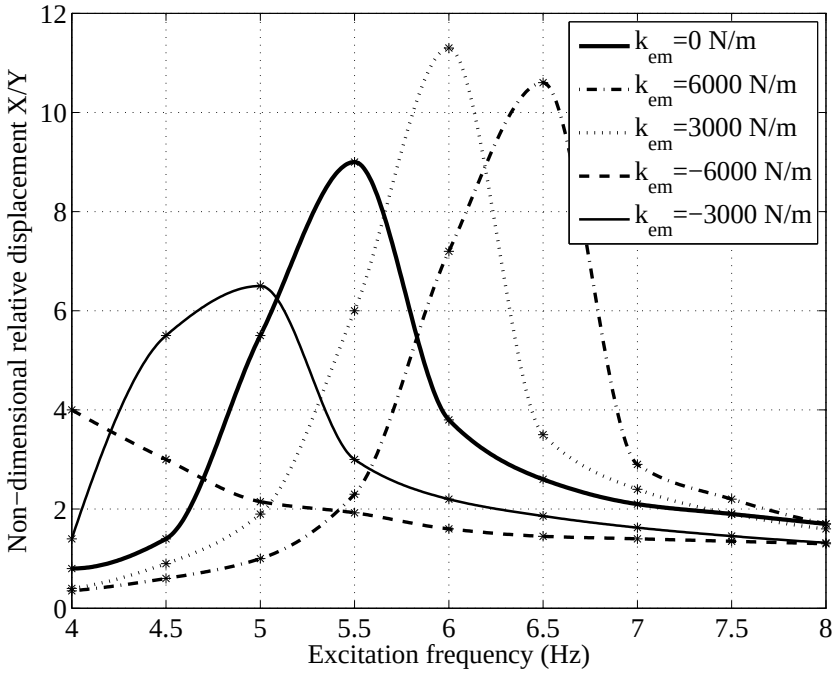

Figure 2.14: System relative displacement with different stiffness values in the frequency sweep

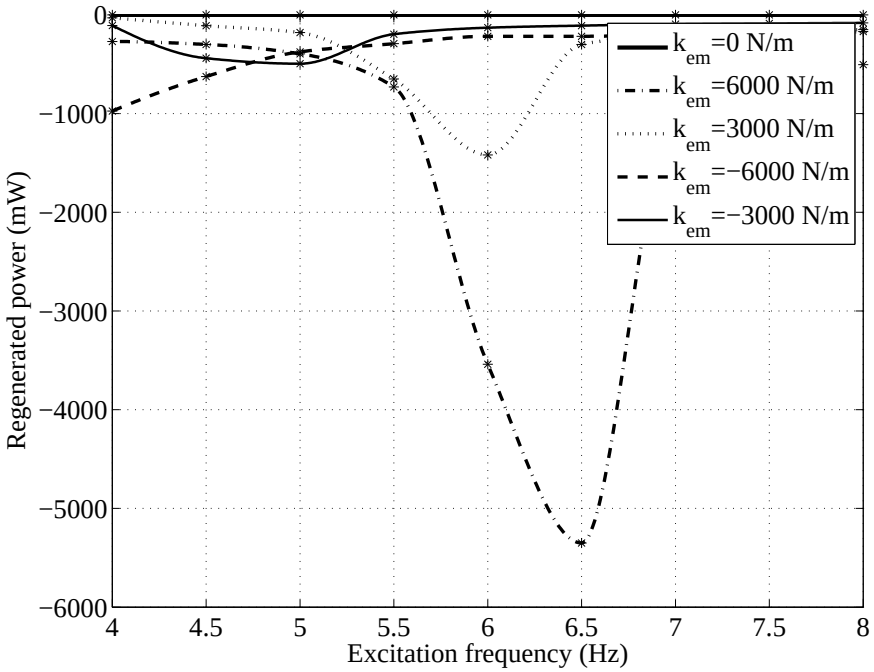

Figure 2.15: System power consumption in the frequency sweep

consumed. In every experiment, power consumption has a peak in resonance frequency. In agreement with (2.19), energy consumption is proportional to the square of displacement and synthetic stiffness injected into the system.

2.5 Conclusions

A switched-mode bi-directional boost converter was utilized for controlling shunt current in an EM actuator. A sliding mode controller was implemented on a dSpace hardware connected to a power converter. Using the proposed system and the current control scheme, synthetic variable resistance and inductance were implemented, resulting in the creation of a damper and stiffness element whose parameters can be controlled in real-time. The experimental results showed that using the method proposed, damping and stiffness of an EM actuator can be changed independently using a simple energy conversion circuitry. Power requirements were analyzed, and it was verified that creating synthetic stiffness is always energy consuming while damping can lead to either energy regeneration or consumption depending on the damping level. The proven idea has a wide range of applications including optimal energy harvesting and vibration control, whose investigation is provided in the coming Chapters.

Chapter 3

Increasing Maximum Achievable Damping with Active Shunt Control

Two common problems in utilizing electromagnetic dampers are addressed in this Chapter. The first problem is the maximum available damping that can be created in an electromagnetic actuator using a positive resistive load. Maximum damping is achieved when motor terminals are placed in a short circuit configuration, but it might not be enough in certain applications. As a solution, a method to produce negative resistance using power electronics and control techniques is presented in this Chapter. The negative resistance cancels part of the resistance of the electromagnetic machine, which leads to producing larger electrical current in the actuator coils. As a result, higher damping levels are generated.

The other contribution in this Chapter is devising an effective motion rectification mechanism for converting the translational motion into rotary motion that drives an electric machine. To this end, a cylindrical cam mechanism is proposed which can provide longer strokes while keeping the geometry and size of the damper similar to the axial dampers used in automotive and bicycle dampers. The mechanism shows longer values for the ratio of stroke to maximum length compared to other designs reported in the literature.

3.1 Introduction

In this Chapter, power electronic techniques are used for increasing maximum available damping force. To this end a negative resistance element is created in the shunt circuit of the actuator. The negative resistance partially cancels out the internal resistance of the machine and induces higher currents in a brushless DC (BLDC) motor coils. Comprehensive modeling and controller design of the proposed system will be provided and validated through experiments. A switched-mode power converter with MOSFETs is used for creating the desired shunt impedance. As a result, it is possible to have a bi-directional power flow between the machine and a power source. Depending on the required damping level, positive or negative resistance can be synthesized in the shunt circuit, and power can be regenerated or consumed. This is one of the advantages of the proposed system over

some similar configurations that allow only one-way power transfer from the power source to the actuator [115, 91, 92].

The other topic covered in this Chapter is designing a new motion rectifier for conversion between rotation of the EM machine and the actuator linear motion. A common challenge in designing such motion converters is providing enough stroke for the damper end effector while keeping the dimensions as small as regular hydraulic dampers. At the same time, enough portion of the whole damper should be dedicated to the EM machine to keep the power density high. For example in [35], a small brushed DC motor is designed in an off-centered position with a ball-screw mechanism to achieve enough travel. In [5] and [57], the motor axis is perpendicular to the damper displacement, which significantly limits the size of the motor. Lead-screw and ball-screw mechanisms are good candidates for motion rectification because of allowing single axis design for the motor and the moving ends [84]. However, damping stroke remains limited because the lead-screw mechanism is relatively long. To avoid this problem, a hollow shaft motor is used in combination with a lead-screw in [99]. To this end, a motor is customized to incorporate the mechanism inside its rotor. For some other mechanisms like two-leg mechanism [58] and algebraic screw [82], increasing stroke needs scale up of the mechanism in all directions, which ends up in extra large radius of the motion converter.

The design provided in [54] consists of rack-pinion mechanism and bevel gears to achieve larger travel and higher power density at the same time. However, bevel gears take up some axial length and result in shorter stroke or power density. To minimize the axial length occupied by the motion rectifier, a cylindrical cam mechanism is suggested and designed as explained in the coming Sections. The cylindrical cam is a hollow cylinder with helical grooves that can slide axially around the motor. A T-type coupler connected to the motor shaft slides inside the grooves and converts linear motion of the cylindrical cam to shaft rotation. Effort has been made to maximize the ratio of the damper stroke to its overall length.

The rest of the Chapter continues as follows: In Section 3.2, an electromechanical model of the system is used for deriving the actuator forcing function. In Section 3.3, the power electronics circuit and current control algorithm capable of creating the desired shunt impedance are introduced, and voltage requirements are analyzed. Details on mechanical design of the novel motion converter are provided in 3.4, and information about experiments setup and the resulting achievements can be found in Section 3.5.

3.2 Electromechanical Modeling

In this Section, an electromechanical model of a linear electromagnetic actuator with resistive shunt is provided. It is assumed that the terminals of the electric machine are connected to a power electronic circuit that synthesizes a negative inductor that cancels out the internal inductance of the machine. A negative resistor is also created in series with the negative inductor to decrease the over-

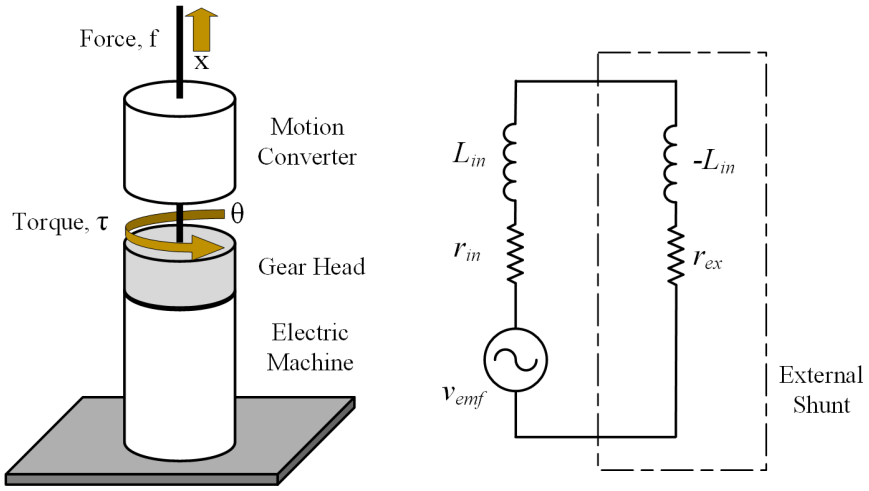

Figure 3.1: Schematic of the electromagnetic actuator with negative resistance and negative inductance

all resistance of the shunt. As a result, a purely resistive shunt circuit is created. Fig. 3.1 shows a schematic diagram of the system.

The Lagrange equation of motion is used to derive the force generated by the actuator regardless of the mechanical friction in the components. Assuming x as the only generalized coordinate of the system, the equation can be written as

$$\frac{d}{dt}\left(\frac{\partial K}{\partial \dot{x}}\right) - \frac{\partial K}{\partial x} + \frac{\partial V}{\partial x} + \frac{\partial D}{\partial \dot{x}} = f. \tag{3.1}$$

The kinetic energy term can be written as

$$K = \frac{1}{2} I \dot{x}^2 \tag{3.2}$$

where I is the effective inertia of the actuator end-effector. The potential energy term is written as

$$V = mgx, \tag{3.3}$$

where m is the actuator mass that moves with the end-effector and g is the gravity acceleration. To obtain the electrical energy dissipation function D, one has to include the power dissipation in the resistors of the shunt circuit. Since the inductors cancel the effect of each other, the power dissipation in the circuit can be written as

$$D = v_{emf}^2 / 2(r_{in} + r_{ex}) \tag{3.4}$$

where v_{emf} is the back emf voltage induced in the shunt circuit, and r_{in} and r_{ex} are the shunt internal and external resistances, respectively. It is possible to write v_{emf} as a function of the actuator speed,

$\dot{x}$, i.e.,

$$v_{emf} = c_{em}\dot{x} \tag{3.5}$$

where c_{em} is the electromechanical coupling of the actuator that can be expanded as follows

$$c_{em} = c_t c_g c_r \tag{3.6}$$

in which c_t is the torque constant, c_g is the gear ratio, and c_r is the motion rectification factor of the motion converter defined as

$$c_r = \frac{\theta}{x}. \tag{3.7}$$

As a result, (3.4) can be written as

$$D = c_{em}^2 \dot{x}^2 / 2(r_{in} + r_{ex}). \tag{3.8}$$

Taking derivatives in (3.1), f is derived as follows

$$f = I\ddot{x} + mg + c_{em}^2/(r_{in} + r_{ex})\dot{x}. \tag{3.9}$$

The first term is the effect of moving inertial elements in the actuator, also known as inertance [89]. If I and $\ddot{x}$ are small enough, this term can be neglected. The second term is a constant value equal to the weight of elements that move vertically. Since the actuator is supposed to be used as part of a larger linear vibration system, this weight could be considered to be part of the weight of the structure connected to the actuator's end-effector. This force can slightly move the equilibrium position of the whole vibration system. But the equations of displacement around the new equilibrium point remain unchanged. Moreover, if the actuator is placed in the horizontal direction, this term becomes zero.

The last term in (3.9) is the main focus of this paper. It shows that the shunt configuration shown in Fig. 3.1, results in an electromagnetic force which is proportional to the actuator velocity in the opposite direction. This is similar to the force created by a mechanical viscous damper. The damping factor of this actuator can be called electromagnetic (EM) damping and will be denoted here as

$$b_{em} = c_{em}^2/(r_{in} + r_{ex}). \tag{3.10}$$

It is possible to calculate the amount of power needed for creating r_{ex} in the shunt circuit. To this end, the power exchange between the external resistance and the rest of the system can be calculated as

$$p(t) = r_{ex} i(t)^2 \tag{3.11}$$

where

$$i(t) = \frac{v_{emf}}{r_{in} + r_{ex}}. \tag{3.12}$$

Using (3.5) and (3.12), power regeneration in the external resistor can be written as

$$p(t) = \frac{c_{em}^2 r_{ex}}{(r_{in} + r_{ex})^2} \dot{x}(t)^2. \tag{3.13}$$

Regarding the application of the actuator as a vibration shock absorber, we assume a single-harmonic sinusoidal motion with amplitude X and frequency ω. Integrating (3.13) in one complete cycle of the motion results in the average harvested power by the actuator as follows

$$P_{avg} = \frac{1}{2} X^2 \omega^2 \frac{c_{em}^2 r_{ex}}{(r_{in} + r_{ex})^2}. \tag{3.14}$$

Equations (3.10) and (3.14) show the effect of the external resistance r_{ex} on the EM damping level and the harvested/consumed power. Fig. 3.2 shows a plot of the two functions. According to this figure, positive values of r_{ex} creates positive EM damping which results in power regeneration (the right-side area). This is the common range of operation in vibration energy harvesters and regenerative suspension systems. If r_{ex} is too large, EM damping level becomes trivial, which is similar to the case that the motor is open-circuit. To achieve maximum power regeneration, the external resistance should be equal to the shunt internal resistance r_{in}. However, to maximize the EM damping, r_{ex} should be reduced to zero. This results in $b_{em} = c_{em}^2/r_{in}$, which is the maximum available damping that does not need power consumption ($P_{avg} = 0$) and is almost equivalent to operation under short circuit.

In certain application scenarios, the maximum available self-powered damping, $b_{em} = c_{em}^2/r_{in}$, might not be enough for absorbing mechanical shocks and controlling vibrations. This may limit the application of an EM damper. To solve this problem, creating negative resistance is suggested in this study. In Fig. 3.2, the middle area shows the region in which negative shunt resistance results in EM damping levels which are larger than c_{em}^2/r_{in}. Theoretically, EM damping can be increased to infinitely large values, however, enough electric power should be available and certain electronic circuit requirements should be met. Further discussions are provided in the next Section.

Reducing external shunt resistance to values less than $-r_{in}$ (i.e. $r_{ex} < -r_{in}$) creates negative damping (the left region in Fig. 3.2). Negative damping results in injection of mechanical energy into the system which might result in instability.

3.3 Power Electronics Control

To create the external shunt impedance shown in Fig. 3.1, a negative inductor should be used in series configuration with a negative resistor. Since this configuration does not physically exist, power electronic techniques are used to synthesize the desired behavior. To this end, the electrical current passing through the circuit in the presence of the desired shunt is calculated using (3.12) and used as the reference current in a current controller. To create the desired current in the circuit of a BLDC

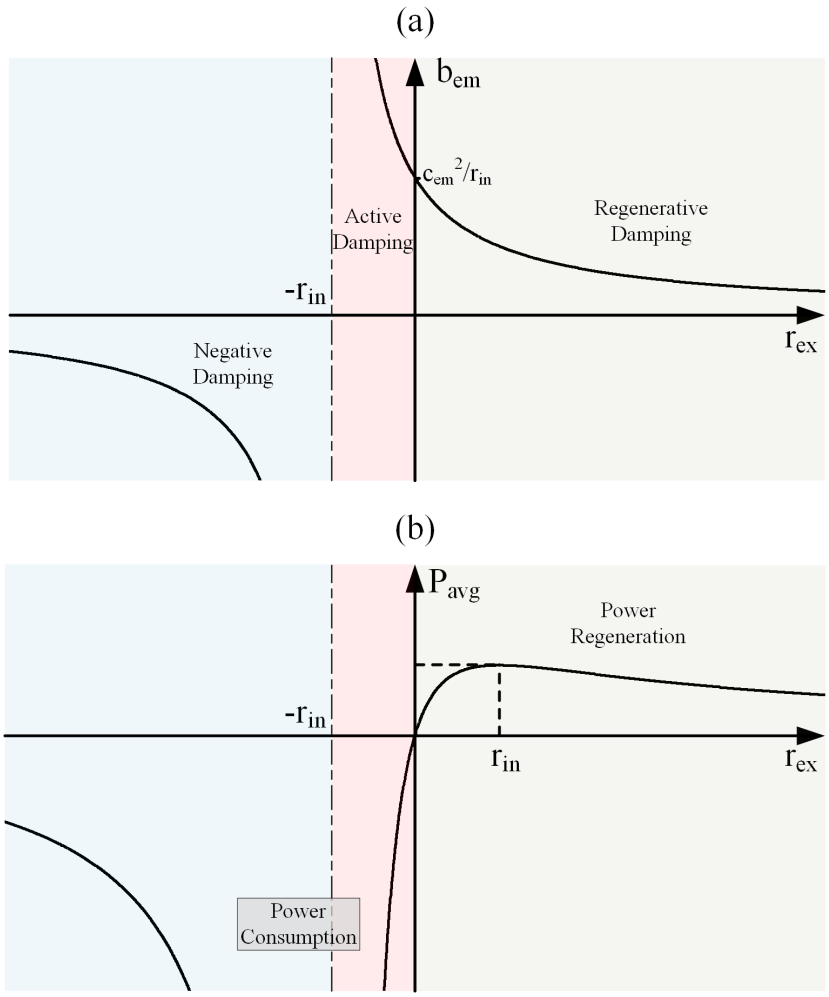

Figure 3.2: Effect of external shunt resistance on (a) EM damping level (b) power regeneration/consumption

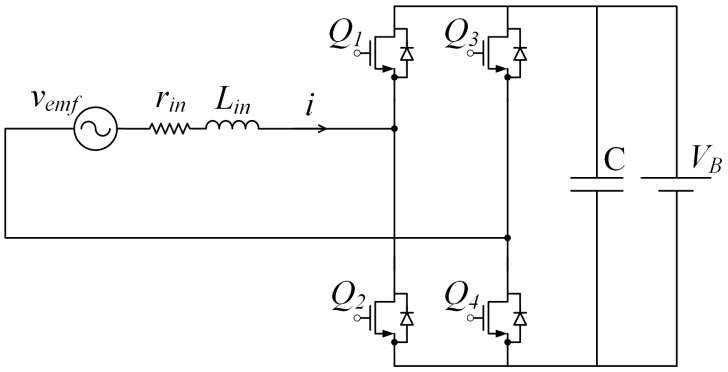

Figure 3.3: Converter topology for BLDC motor shunt current control

motor, an H-bridge with four MOSFETs and freewheeling diodes are used. The two MOSFETs in each leg of the converter take complimentary states. Fig. 3.3 shows the schematic of the circuit.

To describe the behavior of the converter, the circuit equation can be written as [9]

$$L_{in}\frac{di}{dt} = -uV_B - r_{in}i + v_{emf}, \tag{3.15}$$

where i is the shunt current and $u \in \{1, -1\}$ is the input variable which shows the state of switches in the circuit. If $u = 1$, only switches Q_1 and Q_4 are in the conducting mode, whereas $u = -1$ means the opposite.

Sliding mode control is utilized for current tracking. The error between the shunt current and its reference value provided in (3.12) is used as the sliding mode error

$$\sigma = i - i_{des}, \tag{3.16}$$

and the sliding mode control law is

$$u = sign(\sigma). \tag{3.17}$$

To prove stability of the sliding mode controller, a Lyapunov function candidate is used as follows

$$V = \frac{1}{2}\sigma^2. \tag{3.18}$$

The time derivative of the Lyapunov function along the trajectory of the system is calculated as follows

$$\dot{V} = \sigma\dot{\sigma} = \sigma(\dot{i} - \dot{i}_{des}). \tag{3.19}$$

Using (3.15), we have

$$\dot{V} = \sigma(-\frac{r_{in}}{L_{in}}i + \frac{v_{emf}}{L_{in}} - \frac{V_B}{L_{in}}u - \dot{i}_{des}). \tag{3.20}$$

From (3.16), we can use $i = \sigma + i_{des}$, which yields

$$\dot{V} = -\frac{r_{in}}{L_{in}}\sigma^2 + \sigma(-\frac{r_{in}}{L_{in}}i_{des} + \frac{v_{emf}}{L_{in}} - \dot{i}_{des}) - \frac{V_B}{L_{in}}|\sigma|. \tag{3.21}$$

As a result

$$\dot{V} \leq \sigma(-\frac{r_{in}}{L_{in}}i_{des} + \frac{v_{emf}}{L_{in}} - \dot{i}_{des}) - \frac{V_B}{L_{in}}|\sigma|. \tag{3.22}$$

To guarantee convergence of the sliding mode control, the amplitude of the terms in parentheses should be smaller than $\frac{V_B}{L_{in}}$, i.e.,

$$|-\frac{r_{in}}{L_{in}}i_{des} + \frac{v_{emf}}{L_{in}} - \dot{i}_{des}| \leq \frac{V_B}{L_{in}}. \tag{3.23}$$

using (3.5) and (3.12), the inequality can be rewritten as a function of the actuator velocity and acceleration as follows

$$|-\frac{r_{in}}{L_{in}(r_{in}+r_{ex})}c_{em}\dot{x} + \frac{c_{em}\dot{x}}{L_{in}} - \frac{c_{em}\ddot{x}}{r_{in}+r_{ex}}| \leq \frac{V_B}{L_{in}}. \tag{3.24}$$

For a single-harmonic sinusoidal displacement function $x = X\sin(\omega t)$, stability criteria can be simplified as follows

$$V_B \geq \frac{\sqrt{r_{ex}^2 + L_{in}^2\omega^2}}{|r_{in}+r_{ex}|}c_{em}X\omega. \tag{3.25}$$

Using (3.10), the stability criterion can be written as a function of EM damping as follows

$$V_B \geq \frac{\sqrt{(b_{em}r_{in} - c_{em}^2)^2 + L_{in}^2\omega^2}}{c_{em}}X\omega. \tag{3.26}$$

Equation (3.26) shows that there is a minimum DC voltage requirement for the converter to be able to create EM damping b_{em} when the displacement amplitude is X and frequency of motion is ω. This value is plotted as a function of b_{em} in Fig. 3.4. According to Fig. 3.4, the minimum voltage is required when $b_{em} = c_{em}^2/r_{in}$. This is corresponding to $r_{ex} = 0$, which results in the maximum positive non-active damping. Creating EM damping levels higher than this value is equivalent with creating negative external resistance in the shunt circuit (Fig. 3.2), which requires higher voltages. Besides, it is possible to calculate the maximum achievable damping for a certain value of V_B, X and ω. To this end, Eq. 3.26 can be written as follows

$$\frac{c_{em}^2}{r_{in}} - A \leq b_{em} \leq \frac{c_{em}^2}{r_{in}} + A, \tag{3.27}$$

while

$$A = \frac{\sqrt{c_{em}^2V_B^2 - L_{in}^2X^2\omega^4}}{X\omega r_{in}}. \tag{3.28}$$

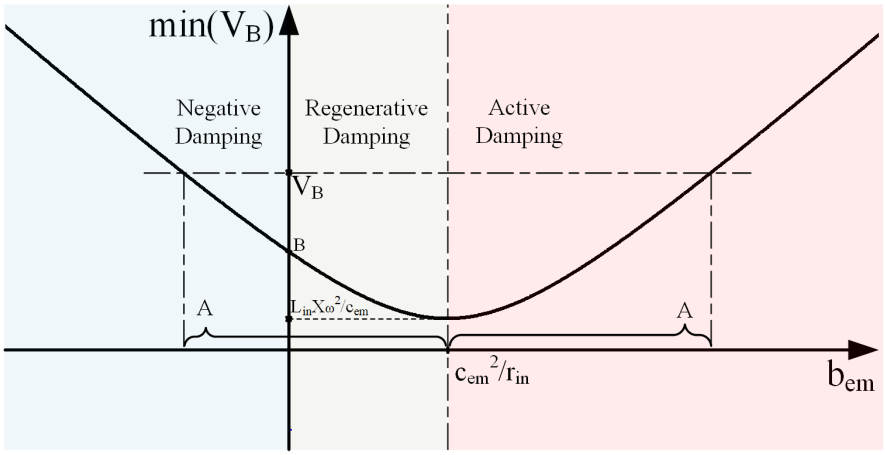

Figure 3.4: Minimum DC source voltage requirement for creating EM damping b_{em}

According to (3.27) and (3.28), to find a range of achievable EM damping levels, A should be a real value which means

$$V_B \geq \frac{L_{in} X \omega^2}{c_{em}}. \tag{3.29}$$

In this case, (3.27) results in a range of EM damping symmetrical with respect to the short circuit damping c_{em}^2/r_{in}. Moreover, to create negative damping (the left side in Fig. 3.4), the minimum necessary DC voltage can be calculated from (3.27) as follows

$$\frac{c_{em}^2}{r_{in}} - A < 0, \tag{3.30}$$

as the result

$$V_B \geq \sqrt{c_{em}^2 X^2 \omega^2 + \frac{L_{in}^2 X^2 \omega^4}{c_{em}^2}} = B. \tag{3.31}$$

The parameters A and B are shown in Fig. 3.4 for better understanding of the derived inequalities.

3.4 Mechanical Design

In this study, a cylindrical cam is proposed as the motion conversion mechanism. Cylindrical cams, also known as groove cams or barrel cams, are cam and follower mechanisms that are usually used for converting rotational motion into linear motion. In this study, the inverse operation, namely linear to rotational conversion, is needed. It is desired to maximize the actuator stroke while keeping the whole design short and compact.

The geometry of the mechanism is shown in Fig. 3.5. As shown in the figure, a helical slot is cut around a hollow cylinder with the walls of the slot perpendicular to the cylinder axis. The groove

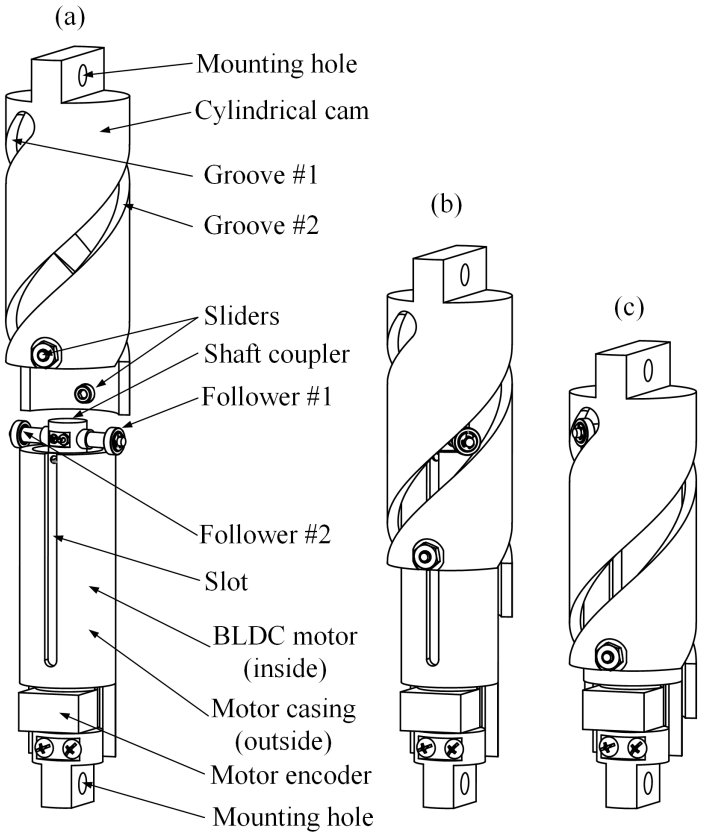

Figure 3.5: Schematic view of the cylindrical cam actuator, (a) extended view, (b) in the middle of travel, (c) compressed view

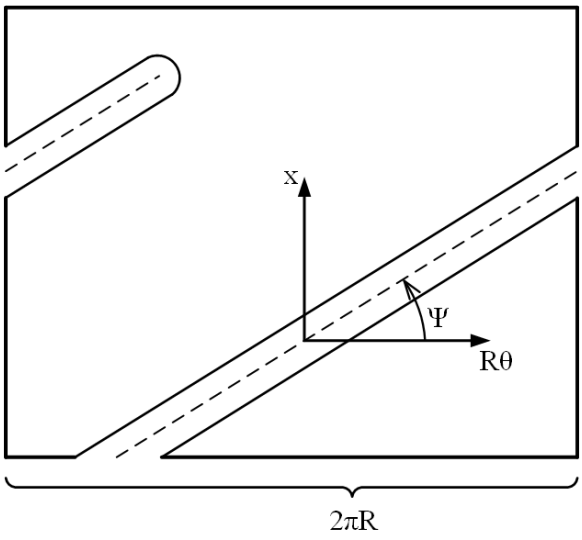

Figure 3.6: Unrolled presentation of the cylindrical cam for calculating motion rectification factor

centerline geometry can be described in the cylindrical coordinate as follows.

$$\begin{cases} r(t) = R \\ \theta(t) = c_r x(t), \end{cases} \tag{3.32}$$

where c_r is the motion rectification factor of the mechanism. For calculating c_r, it is possible to imagine the cylindrical cam unrolled to a flat plate as shown in Fig. 3.6. In this figure, the horizontal bottom line is equal to the circumference of the cylinder intersection while the vertical line is equal to the height of the cam. The helical groove is unrolled to a linear slot that makes an angle ψ with the horizontal line. The relationship between axial movement x and rotation of the shaft θ can be calculated as

$$x = \tan(\psi) R\theta, \tag{3.33}$$

where R is the cylinder radius. As a result, the motion rectification factor can be calculated as

$$c_r = \frac{1}{\tan(\psi) R}. \tag{3.34}$$

The groove has a closed end on its top but, in the bottom end, it is open to the followers. The follower consists of two small ball bearings mounted on a T-type shaft coupler. The coupler is connected to the shaft on one side and supports the bearings on the other. The bearings slide inside the groove to make the shaft follow the linear motion according to (3.32).

To achieve the desired relative motion between the cylinder and the motor, one must prevent rotation of the cam with respect to the motor's stator. To this end, a casing is added to the motor with two axial slots machined on it. The cam is made to move only along the two slots using two

Table 3.1: Comparison between the cylindrical cam damper and other mechanisms in the literature

Mechanism name	Maximum length (cm)	Travel (cm)	Normalized travel
Cylindrical cam	**27.5**	**8.5**	**0.309**
Algebraic screw [82]	35.4	2.4	0.08
Two leg mechanism [58]	30	3	0.1
Ball screw mechanism [57]	60	15	0.25
Electro-hydraulic damper [116]	140	20	0.143
Helical gear damper [84]	40	12	0.231

small sliders fixed on it. Moreover, two mounting holes are designed on the ends of the actuator for easy handling in conducting experiments (Fig. 3.5).

Before manufacturing, the components were all 3D-printed, and the geometry was tested on a DC motor with gearhead and encoder. After rapid prototyping, the parts were manufactured by CNC machining. Maxon DC motor model 392012 with encoder model HEDL5540A11 by the Broadcom and a Maxon gearhead with ratio 4.8:1 were used in the final design. Fig. 3.7 shows the final manufactured damper.

A comparison is made about the maximum size of other electromagnetic dampers in the literature. For a meaningful comparison between dampers of different sizes, normalized stroke is defined as the ratio of the damper travel to its maximum length. Referring to Table 3.1 and comparing the values in the last column reveal that the mechanism used in this study has a larger travel compared to the other designs in the literature.

3.5 Experimental Results

To validate the performance of the system under study, a sliding mode current control algorithm was implemented on a dSpace real-time control hardware with a sampling frequency $f_s = 50kHz$. The evaluation board DRV8305 by TI was used as the power electronic converter. For current sensing, the fully differential isolation amplifier AMC1100 was used in combination with a $25m\Omega$ shunt resistor.

To test the generated force, the actuator was connected to an electromagnetic shaker on one side and fixed on the other side. The load cell LCHB-1k by Omega was installed between the damper and the shaker for force measurement. DMD-465 Bridgesensor from the same company was used as the load cell amplifier. The sensor output data was acquired by the same dSpace used for control, and the values were plotted and saved using the ControlDesk software. Fig. 3.8 shows the test setup and the control hardware.

Two scenarios were considered for testing the performance of the system. In the first test, the system was shaken with a constant displacement amplitude and frequency ($X = 4mm$ and $\omega = 3Hz$). Different damping levels were created by the damper. The force-displacement plots

Figure 3.7: Cylindrical cam damper, manufactured

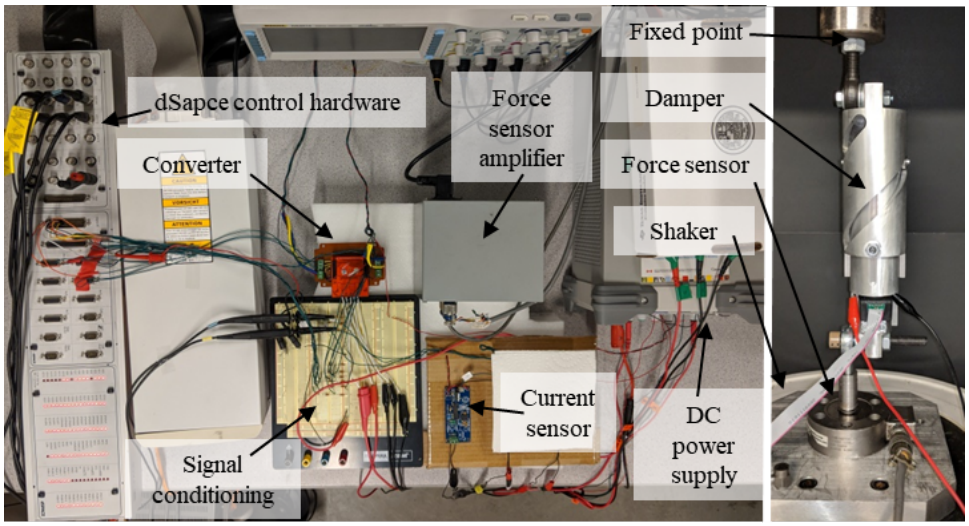

Figure 3.8: Test setup used for conducting experiments

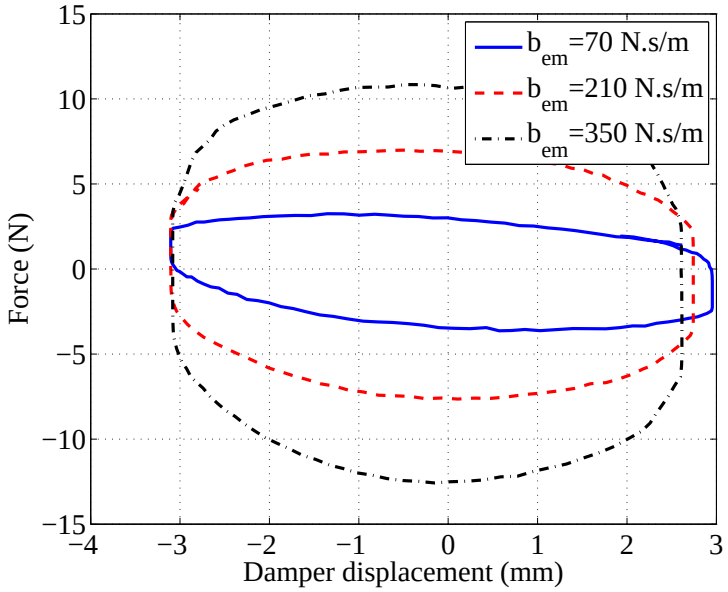

Figure 3.9: Force-displacement plots for different damping levels when $X = 3mm$ and $\omega = 3Hz$

are provided in Fig. 3.9. As shown in Fig. 3.9, the force-displacement curves show power damping by the actuator. The damping force is almost equal to zero at the ends of the stroke, which corresponds to zero velocity. The maximum damping force is generated in the middle of the damper travel ($x = 0mm$), that coincides with the maximum velocity. As the result, oval shapes are plotted as expected from the force-displacement curves. The curves acquired in the experiments are slightly inclined in the clockwise direction. This can be attributed to the inertial term derived in (3.9).

In another experiment, a constant level of damping was created when the damper was operated under different frequencies ($\omega = 2, 3, 4Hz$). Fig. 3.10 shows force displacement curves of this experiment. Increasing frequency while leaving the amplitude unchanged, resulted in an increase in the speed amplitude. As a result, larger damping forces were generated. However, the inertial force that twists the curves becomes larger since it is proportional to frequency squared.

Current control and force generation by the damper is plotted as a function of time in Fig. 3.11. In the first plot, displacement of the system was calculated using the encoder data. It should be noted that the curve is flat in its maxima and minima because of the backlash in the motion converter. As a result, the velocity signal shown in Fig. 3.11(b) remains at zero temporarily when the damper reaches the ends of the stroke. In Fig. 3.11(c), the shunt current is shown. The current is apparently following the desired value which is in phase with the damper velocity to create the desired damping. Finally, Fig. 3.11(d) presents the actuator force. It shows that the actuator has created a damping force, which is the desired behavior in this study.

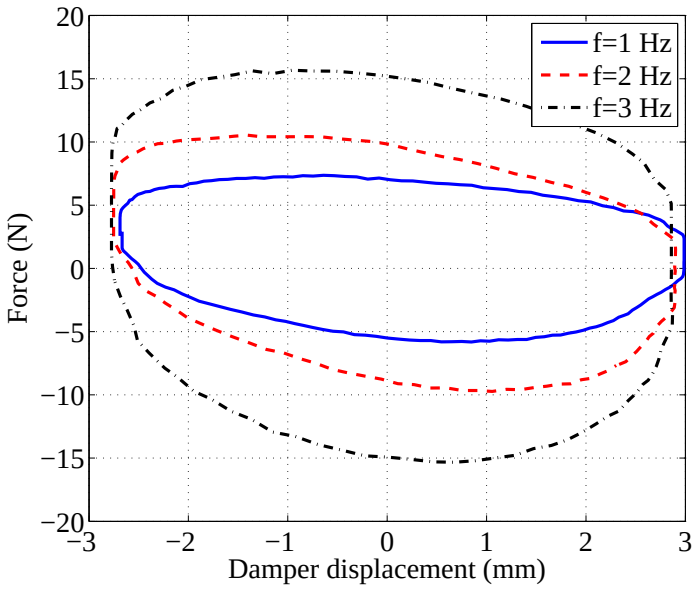

Figure 3.10: Force-displacement plots for different displacement frequencies when $X = 3mm$ and $b_{em} = 40Ns/m$

3.6 Conclusion

Using a power electronics converter, negative resistance was created in the shunt circuit of an electromagnetic actuator. It was shown that using this method, large EM damping levels can be achieved if DC voltage requirements are met. Mathematical expressions were derived to show the minimum voltage required for any level of negative resistance or EM damping. Experimental results proved feasibility of the suggested method as well as its simple implementation.

Regarding the mechanical design, it was shown that the cylindrical cam mechanism is a viable configuration for motion conversion in EM dampers and linear force actuation. The proposed mechanism can be considered a solution for applications in which larger travels are needed in an axial design with limited length and radius.

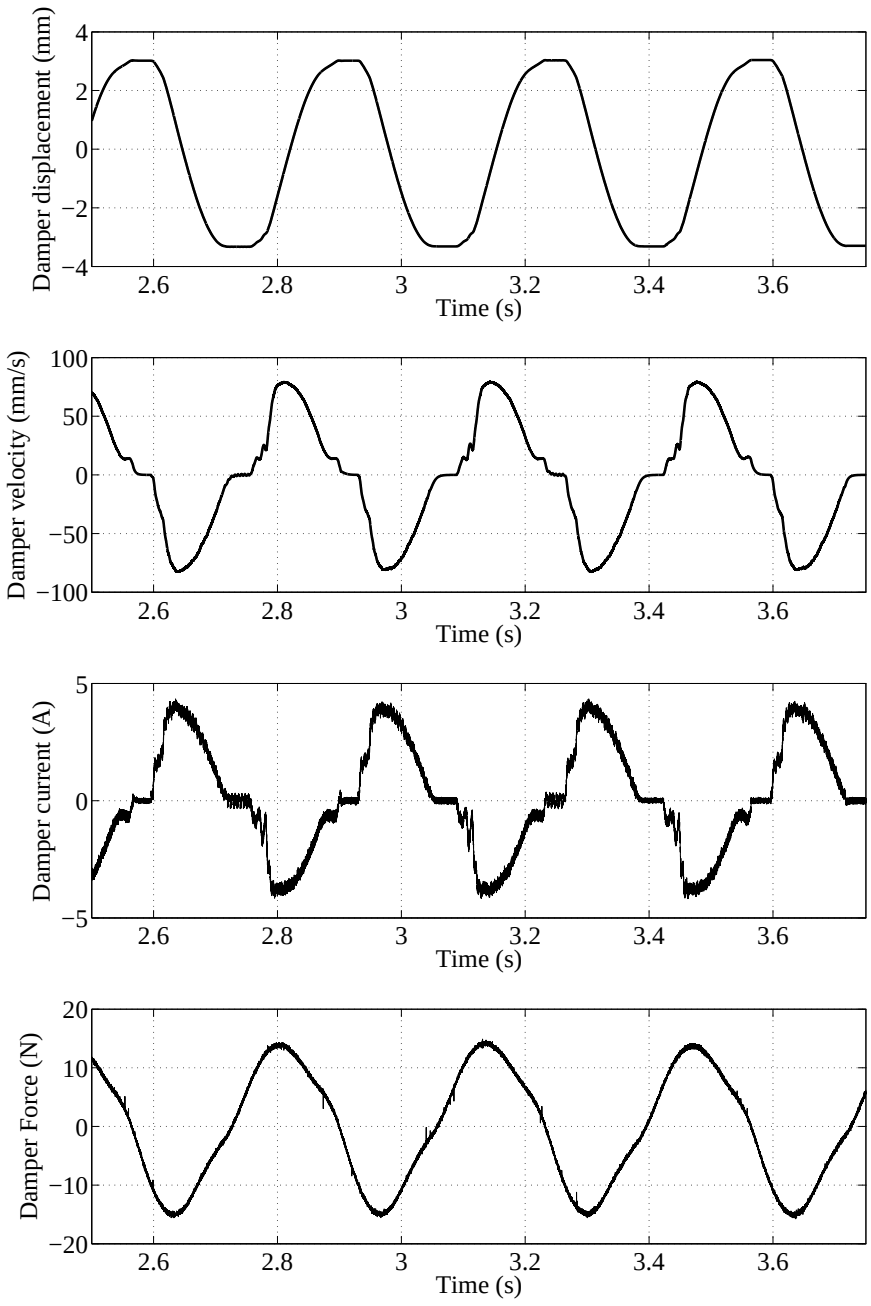

Figure 3.11: Damper displacement, velocity, current and force for $f = 3Hz$ and $X = 3mm$

Chapter 4

Single-Variable Constrained Self-Tuning for Vibration Energy Harvesting

This Chapter presents a constrained model-free tuning algorithm for vibration energy harvesters. Ideally, a vibration energy harvester should operate such that it can absorb the maximum available power when the system undergoes changes in amplitude and frequency of the base excitation input. Furthermore, a vibration energy harvester may have restriction on the maximum allowable value of the displacement of its mass which should not be exceeded during operation. In this Chapter, we utilize an electromagnetic energy converter and power electronic circuitry to create the effect of an adjustable shunt resistive load. A constrained sliding mode extremum-seeking controller is utilized such that the average harvested power is maximized and the mass displacement is kept within an allowable range. Experimental results are presented, which show that the proposed controller can track the maximum power point without violating the constraint on displacement.

4.1 Introduction

Energy harvesting from ambient mechanical vibration has been an active area of research in the past two decades [107, 6]. Its applications include battery-less operation of small electronic sensory systems with very low energy consumption [24], energy harvesting for wearable electronics, and vibration monitoring equipment [3, 71].

In principle, a vibration energy harvester consists of an inertial element that is fixed on a compliant structure such as a cantilever beam or coil spring [18]. In electromagnetic (EM) harvesters, the relative motion between the inertia and the rest of the harvester induces an emf voltage in the harvester's shunt circuit [46]. Using a power electronic circuit, the available energy is consumed in an electrical load or stored in an energy storage device such as a battery or supercapacitor [25].

It has been shown that for a specific displacement of the harvester, to maximize the power extraction, the shunt circuit should be purely resistive [83]. The resistive load in the shunt circuit results in electromagnetic (EM) damping created by the harvester [82]. Furthermore, there is an

optimum EM damping for maximum power extraction depending on the model of the harvester and the excitation characteristics [96].

Traditionally, EM damping (or shunt resistance) of a vibration energy harvester is designed based on the model of the harvester and input excitation [80]. However, there are always uncertainties in system parameters and input variables such as excitation frequency and amplitude [14, 15] which may hinder extracting maximum available power from a vibration energy harvester. To tackle the above problem, one may tune the harvester using a Maximum Power Point Tracking (MPPT) algorithm that can adapt to different working conditions.

Advanced extremum-seeking algorithms that do not require the gradient of the performance function have not been studied for vibration energy harvesting applications. Moreover, current model-free and self-tuning algorithms for vibration energy harvesting do not put any constraint on the harvester's maximum displacement. In other words, the output power is commonly optimized regardless of the fact that the harvester mass may experience very large displacements that exceed its physically allowable boundaries. This becomes more likely when there is uncertainty on the amplitude of the input excitation to high levels that may damage the harvester [33, 94, 90].

In this Chapter, a Sliding Mode Extremum-Seeking Controller (SMESC) is used as an alternative to conventional MPPT methods [4, 87, 1, 51]. By considering a maximum allowable displacement, the harvester's displacement amplitude is kept within an allowable bound. To this end, a constrained sliding-mode extremum-seeking controller is utilized for tuning the harvester's load. A piecewise penalty term is used in the objective function to impose the displacement constraint when the input excitation amplitude becomes larger than expected. A Brushless DC (BLDC) motor combined with a two-leg motion converter [58] is utilized as the harvester and connected to a boost-converter circuit for creating a resistive load in the shunt circuit.

The Chapter is organized as follows: In Section 4.2, an electromechanical model of the harvester and shunt circuit are used for obtaining the constrained optimum load of the harvester. Next, the effect of optimum load on performance of the system under different excitation frequencies is presented. The constrained self-tuning algorithm is introduced in Section 4.3. Experimental verification of the proposed system is provided in Section 2.4.

4.2 Analytical Modeling and Optimization

Consider a three-phase generator used in a vibration energy harvester with mass m, mechanical stiffness k, and mechanical damping b (Fig. 4.1). The actuator is connected to an electric converter to create a variable and purely resistive shunt circuit with resistance R. This results in a variable electromagnetic (EM) damping term b_{em} as follows

$$b_{em} = \frac{{c_{em}}^2}{R} \tag{4.1}$$

where c_{em} is the electromechanical coupling term of the linear actuator.

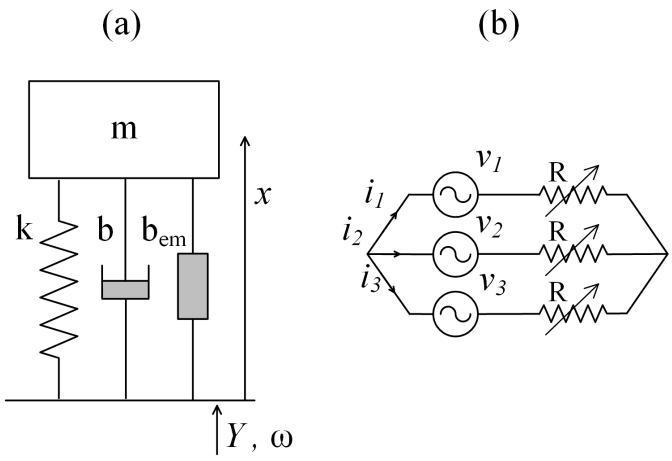

Figure 4.1: (a)Vibration energy harvester, (b)Variable resistive load.

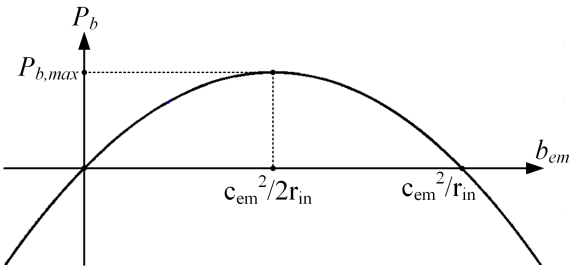

Figure 4.2: Average harvested power as a function of electromagnetic damping.

As shown in Fig. 4.1, the input is a single-frequency harmonic displacement with amplitude Y and frequency ω. The resulting steady-state response has the same frequency and a relative displacement with amplitude X given by

$$X = \frac{m\omega^2 Y}{\sqrt{(k - m\omega^2)^2 + (b + b_{em})^2\omega^2}}. \tag{4.2}$$

It can be shown that the amount of power harvested as a result of creating b_{em} is as follows

$$P_{avg} = \frac{3}{4}X^2\{\omega^2(b_{em} - \frac{r_{in}}{{c_{em}}^2}{b_{em}}^2)\} \tag{4.3}$$

where r_{in} is the per phase internal resistance of the machine.

A plot of (4.3) as a function of EM damping for a constant amplitude and frequency is shown in Fig. 4.2. As shown, the system can harvest energy when it creates a range of damping between 0 and c_{em}^2/r_{in} with its maximum at $b_{em} = \frac{c_{em}^2}{2r_{in}}$. However, referring to (4.3) and (4.2), X is a function

of system characteristics and input excitation. Combining the two equations results in

$$P_{avg} = \frac{3}{4} \frac{m^2 \omega^4 Y^2 \left(\omega^2 (b_{em} - \frac{r_{in}}{{c_{em}}^2} {b_{em}}^2) \right)}{\left(k - m\omega^2\right)^2 + \left(b + b_{em}\right)^2 \omega^2}. \tag{4.4}$$

Equation (4.4) can be used to calculate the harvested power as a function of input frequency ω, input amplitude Y, and the electromagnetic damping b_{em}. It can be further used to calculate the optimum damping value at each input frequency. To this end, differentiating P_{avg} with respect to b_{em} and setting it to zero, we have

$$\frac{\partial P_{avg}}{\partial b_{em}} = 0 \tag{4.5}$$

$$b_{\text{em,op}} = \frac{\Lambda - \sqrt{\Lambda^2 + 4\Lambda\omega^2 (b\hat{b} + \hat{b}^2)}}{-2\omega^2 (b + \hat{b})} \tag{4.6}$$

where

$$\Lambda = \left(k - m\omega^2\right)^2 + b^2\omega^2 \tag{4.7}$$

$$\hat{b} = \frac{{c_{em}}^2}{2r_{in}}. \tag{4.8}$$

The term $\hat{b}$ is interpreted as the EM damping when the shunt circuit is purely resistive with resistance $2r_{in}$. Moreover, if the system is excited at its own natural frequency $\omega = \sqrt{\frac{k}{m}}$, (4.6) reduces to

$$b_{em,op} = \frac{b\hat{b}}{b + \hat{b}}. \tag{4.9}$$

It is assumed that the system is designed to work at a design frequency ω_{des} and amplitude Y_{des}. For optimal performance, the harvester must be designed such that its natural frequency is ω_{des}. However, there is usually uncertainty both in frequency and amplitude of the input vibration as illustrated in Fig. 4.3.

Considering the changes in excitation frequency, an adaptive system can be used to change the damping term according to (4.6) so that the harvested power is maximized at each frequency. However, the optimum EM damping value may result in displacements which are too large considering the physical constraints of the harvester. This is more likely to happen when the excitation amplitude drifts to a value higher than the original design value Y_{des}. In such a case, the EM damping should be large enough to keep the relative displacement equal to or smaller than its maximum allowable value X_{max}. In other words, b_{em} should be larger than a minimum value $b_{\text{em,min}}$, which is the EM damping that results in the maximum allowable displacement X_{max}. To calculate this minimum

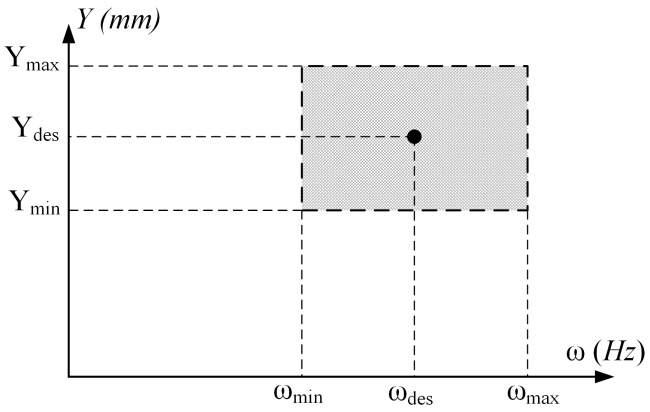

Figure 4.3: The uncertainty range for the input excitation.

value, b_{em} in (4.2) is calculated when $X = X_{max}$, i.e.,

$$b_{\text{em,min}} = \sqrt{\frac{\frac{m^2\omega^2Y^2}{X_{max}^2} - (k - m\omega^2)^2}{\omega^2}} - b. \tag{4.10}$$

Equation (4.10) should be taken into account when there is a constraint in terms of the harvester displacement. We can now introduce $b_{\text{em,csr}}$ as the constrained optimum EM damping as follows

$$b_{\text{em,csr}} = \begin{cases} b_{\text{em,op}} & , (b_{\text{em,op}} \geq b_{\text{em,min}}), \\ b_{\text{em,min}} & , (b_{\text{em,op}} < b_{\text{em,min}}). \end{cases} \tag{4.11}$$

According to (4.11), the optimum damping $b_{\text{em,op}}$ calculated by (4.6) can be used if it is already larger than $b_{\text{em,min}}$, otherwise $b_{\text{em,min}}$, which is the closest allowable value to $b_{\text{em,op}}$, should be adopted as the harvester damping.

The analysis provided above can be used for tuning a vibration energy harvester under different frequencies and amplitudes. To make the system self-tuning, the model-based and feed-forward structure shown schematically in Fig. 4.4 can be used. In this system, the frequency and amplitude of the input excitation are estimated at each control cycle. Then, the optimum b_{em} is calculated using (4.6) or (4.11) depending on the constraint on the harvester displacement. The optimal damping can be programmed in the system as a formula or look-up-table so that the EM damping can be updated accordingly. As a result, the harvester tracks the optimal operating point.

To see how the optimal EM damping changes under different frequencies, parameters of the energy harvester used in the experiments of this study (Table. 4.1) are used. The response of the system in terms of damping, harvested power, and displacement amplitude are plotted using (4.2), (4.4), (4.6) and (4.11). It is assumed that the harvester is originally designed to work with $\omega_{\text{des}} = 5.5Hz$ and $Y_{\text{des}} = 2mm$, but the simulations evaluate adaptiveness of the system when the input characteristics deviate from the original design values. To this end, the input excitation is $Y = 3mm$ with the

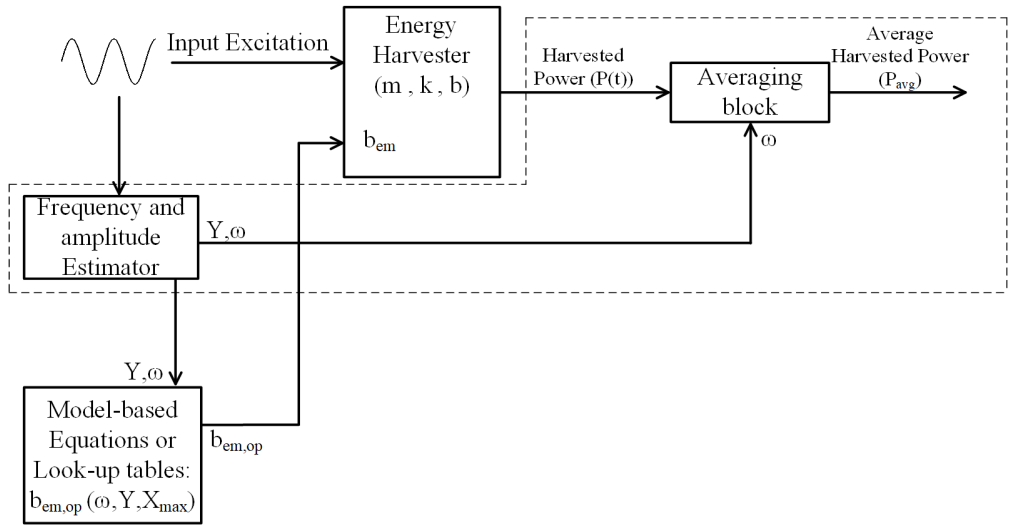

Figure 4.4: Open-loop model-based autonomous system for self-tuning energy harvester in different frequencies and amplitudes.

input frequency ranging from $\omega = 4Hz$ to $7Hz$. Figure 4.5 shows the simulation results for both the constrained and non-constrained adaptive systems. Besides, a non-adaptive system designed for $\omega = 5.5Hz$ without consideration of the constraint is plotted for comparison.

In Fig. 4.5(a), the damping values for the three approaches (non-adaptive, non-constrained adaptive and constrained adaptive) are compared. Unlike the two adaptive systems, the non-adaptive damping does not change from $b_{\text{em}} = 33N.s/m$, which is the optimum damping for $\omega = 5.5Hz$. The curves for constrained and non-constrained adaptive systems coincide except for frequencies around the resonance frequency. This can be explained using Fig. 4.5(b), in which the non-constrained system has exceeded the maximum value of X_{max}, while the constrained system has remained in the allowable range. Moreover, the two adaptive systems have lower displacements compared to the non-adaptive system. This is because they adopt higher damping values as shown in Fig. 4.5(a).

The average regenerated power is plotted in Fig. 4.5(c). The non-constrained adaptive system has the highest power generation since it adapts to frequency changes without being affected by the maximum displacement constraint. In contrary, the non-adaptive system is effective only around the design frequency with the disadvantage of exceeding the constraint. However, the constrained adaptive system not only adapts to frequency changes, but also complies with the displacement constraint (Figs. 4.5(b) and 4.5(c)).

The simulation results show how the tuning method provided in Fig. 4.4 affects the bandwidth of the energy harvester. Moreover, a constrained tuning scheme is needed if there exists a maximum allowable displacement. However, the open-loop system provided so far relies on the model of the harvester. As a result, the controller performance is deteriorated if there are uncertainties or changes in the system model.

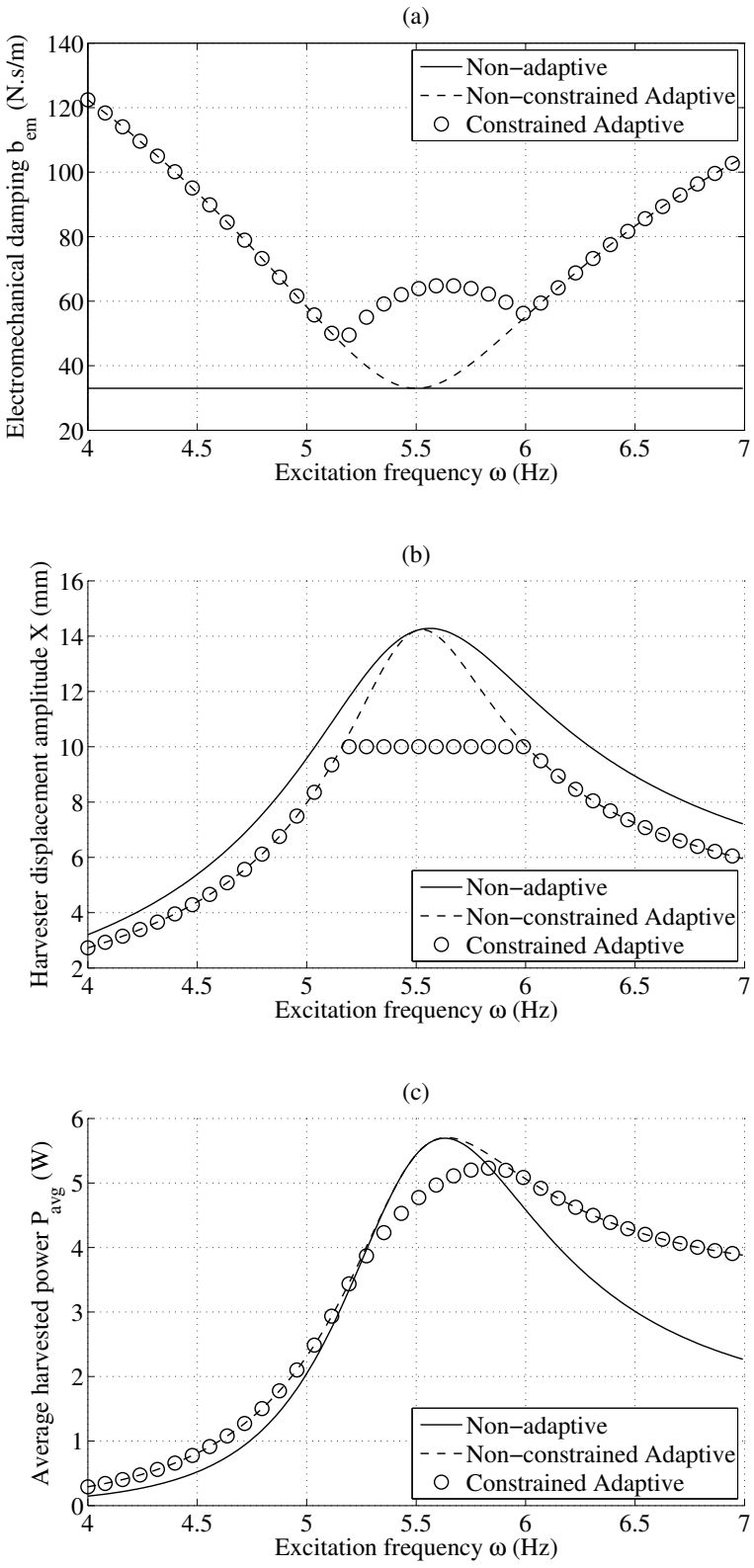

Figure 4.5: (a) Harvester electromagnetic damping in the frequency range, (b) Harvester displacement, (c) Average harvested power.

Table 4.1: Parameters of the vibration energy harvester with maximum allowable displacement

Parameters	Value
mass, m	$10kg$
mechanical stiffness, k	$12000N/m$
mechanical damping, b	$40N.s/m$
actuator internal resistance, r_{in}	4.9Ω
actuator electromehcanical coupling term, c_{em}	$43N/A$
minimum frequency, ω_{min}	$4Hz$
maximum frequency, ω_{max}	$7Hz$
design frequency, ω_{des}	$5.5Hz$
minimum amplitude, Y_{min}	$1mm$
maximum amplitude, Y_{max}	$3mm$
design amplitude, Y_{des}	$2mm$
maximum allowable displacement, X_{max}	$10mm$

4.3 Extremum-Seeking Algorithm

In the open-loop tuning system discussed in Section 4.2 (Fig. 4.4), neither the harvested power P_{avg} nor the harvester displacement X were used as feedback signals by the tuning algorithm. A sliding mode extremum-seeking controller is suggested as a model-free tuning scheme for tunable energy harvesting. The controller is capable of maximizing an objective function f with changing the input, which is the harvester load/damping b_{em} in this study.

As shown in Fig. 4.6, average harvested power P_{avg} is utilized as a feedback in the extremum seeking block to calculate the objective function f. In the presence of the displacement constraint discussed before, vibration amplitude X of the harvester is measured in the block named "output amplitude measurement block" and used for calculating the objective function.

The extremum-seeking constraint is treated as a penalty term in the objective function. The difference between the harvester displacement and its maximum allowable value X_{max} is added as a negative piecewise cost function. If the vibration amplitude is smaller than the maximum allowable value, no cost is put in the objective function, while amplitudes larger than X_{max} reduce the function. This can be represented as follows

$$f(P_{avg}, X) = \begin{cases} P_{avg} - a(X - X_{max}), & X > X_{max} \\ P_{avg}, & X < X_{max} \end{cases} \tag{4.12}$$

where the parameter a is used to adjust the scale difference between the harvested power and its displacement error.

Regarding the power measurement block, it should be noted that the instantaneous harvested power of the system $P(t)$ is a periodic signal with the same period as the input excitation. Thus to calculate the average power P_{avg}, $P(t)$ should be integrated in one or several complete periods of

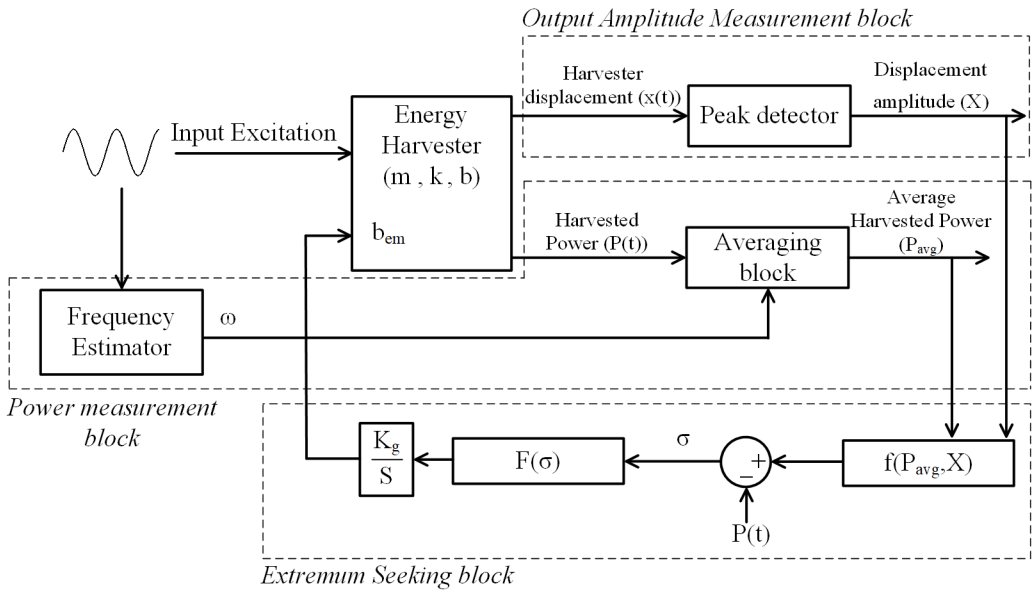

Figure 4.6: Extremum seeking control for self-tuning energy harvester in different frequencies and amplitudes with or without constraint.

the excitation and then divided by the integration period. This is why the averaging block in Fig. 4.4 uses the frequency estimated by the frequency estimator block.

Self-tuning is performed by the sliding mode extremum-seeking block. The average harvested power P_{avg} and the displacement amplitude X are given to the block for calculating the objective function using (4.12). The objective function is then subtracted by a function $P(t)$ which is the sliding curve. For maximization of the objective function, the sliding curve should be a function with a positive constant slope [70, 31]; hence, a linear ramp $P(t)$ is used.

The error between the objective function F and the sliding curve $P(t)$ is fed to the control law $F(\sigma)$ that makes the objective function track the sliding curve. Since the model of the harvester is unknown, a periodic function is used as follows

$$F(\sigma) = \tan^{-1}(\sin(\pi\sigma/\alpha)), \tag{4.13}$$

where σ is the sliding mode error, and α defines the chattering frequency and range in the sliding mode controller. The output of the function is then multiplied by a gain K_g that determines how fast the optimization variable changes to take the system to the optimum point. The result is given to an integrator that calculates the optimization variable b_{em}. If the parameters of the controller are chosen properly, stability of the system is guaranteed [98, 113].

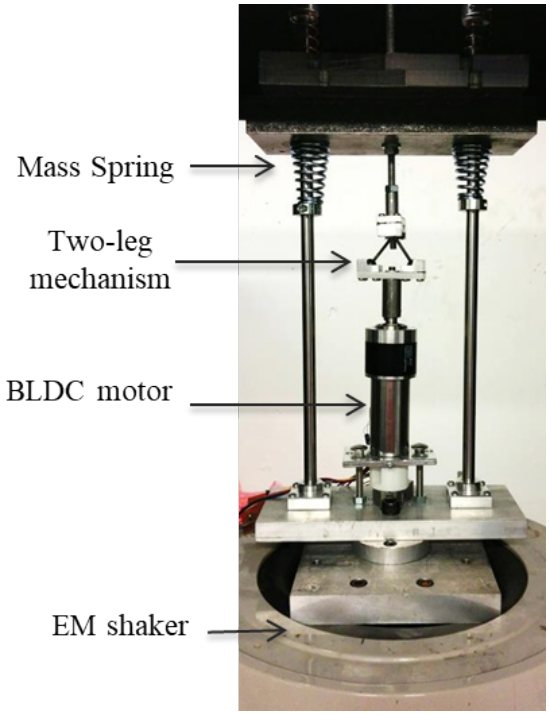

Figure 4.7: Mechanical setup used as the vibration energy harvester.

4.4 Experiments

The performance of the self-tuning method is evaluated on an experimental energy harvester testbed. The setup consists of a Maxon EC-MAX BLDC motor as the generator and a mass-spring mechanical system. To convert the motor torque to a linear force, a two-leg mechanism [58] is utilized, with the whole setup excited using an electromagnetic shaker. Figure 4.7 shows the harvester mechanical setup.

To emulate the desired shunt circuit shown in Fig. 4.1, the motor is connected to a power supply through a TI DRV8305 three-phase boost converter. The shunt current is controlled using the sliding mode control algorithm [78] implemented on a dSpace real-time control hardware with sampling frequency $f_s = 50kHz$. A fully-differential isolation amplifier (AMC1100 from Texas Instruments) and an encoder (HEDS-5540A14) are used to measure the motor current and displacement, respectively, which are required for controlling the harvester. Parameters of the experimental setup are provided in Table 4.1 in which $X_{\text{max}} = 5mm$ is assumed as the maximum allowable displacement.

Before testing the tuning system, an identification test was performed to find the constrained and non-constrained optimum damping. To this end, the system EM damping was increased from $b_{\text{em}} = 0\ N.s/m$ to 200 $N.s/m$ with an excitation amplitude of $Y = 1.25mm$ and frequencies $\omega = 5.5Hz$ and $7Hz$. The harvester displacement and its average power were measured and plotted in Figs. 4.8 and 4.9. Figure 4.8 implies that, at $\omega = 5.5Hz$, the minimum damping needed for keeping the harvester displacement less than $X_{\text{max}} = 5mm$ is $b_{\text{em,min}} = 67\ N.s/m$. However, for

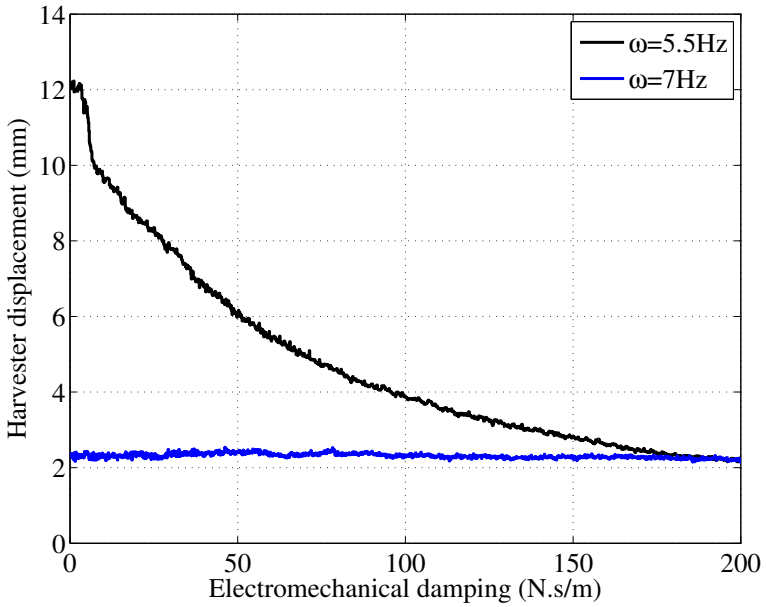

Figure 4.8: Changes in the harvester displacement as a function of electromagnetic damping in two different frequencies.

$\omega = 7Hz$, the displacement does not exceed the maximum allowable value. This means that the EM damping can be reduced to values as low as $b_{\text{em}} = 0\ N.s/m$ without exceeding the X_{max} constraint.

Referring to Fig. 4.9, no power is harvested when there is no EM damping ($b_{\text{em}} = 0$). Harvested power increases with the damping to its maximum value and starts decreasing after a peak. For $\omega = 5.5Hz$, it can be inferred that the non-constrained optimal damping is almost $b_{\text{em,op}} = 43\ N.s/m$. This damping results in $X = 6.6mm$ which is above the maximum allowable value. As a result, the damping should increase to $b_{\text{em}} = 67N.s/m$, which is the constrained optimum value located at the boundary of the constraint. For $\omega = 7Hz$, the non-constrained optimal damping is almost $70N.s/m$ which does not violate the constraint. The optimum points found were used for verifying the performance of extremum-seeking controller in the rest of the experiments.

In the next experiment, an initial damping of $b_{\text{em}} = 150\ N.s/m$ was used at the beginning of the test. First the system was excited with the design frequency $\omega = 5.5Hz$, but at time $t = 550s$, the excitation frequency was abruptly changed to $\omega = 7Hz$, which is away from the harvester's natural frequency. This scenario was tested once with the non-constrained control system and once with the maximum allowable displacement $X_{\text{max}} = 5mm$. The results are shown in Fig. 4.10.

According to Fig. 4.10(a), both controllers start decreasing the damping in the first 200 seconds. The non-constrained system ended up oscillating around point $b_{\text{em}} = 43N.s/m$, which is the non-constrained optimum point indicated in Fig. 4.9. However, the constrained controller has not reduced the damping to values below $67\ N.s/m$ to harness the displacement. The result of damping changes on the harvester displacement amplitude is shown in Fig. 4.10(c). The non-constrained system exhibited large displacements up to $9mm$, while the constrained system did not violate the

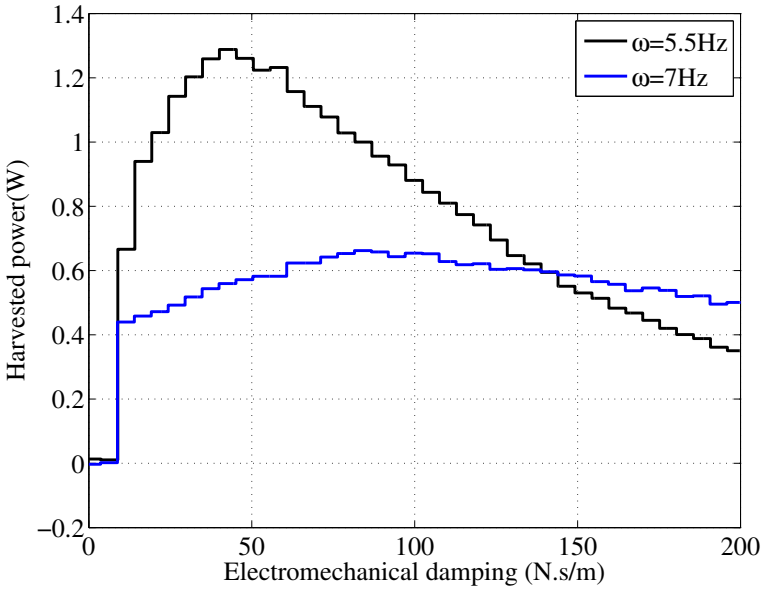

Figure 4.9: Changes in the average harvested power as a function of electromagnetic damping in two different frequencies.

$5mm$ limit. Regarding the harvested power, as seen in Fig. 4.10(b), both systems show an initial increase in the harvested power, while the constrained control resulted in lower power because of the constraint.

After the frequency change in the middle of the test, the non-constrained damping successfully moved to its new optimum point of $b_{\text{em}} = 70N.s/msec$. This is again in harmony with the identification results shown as Fig.4.9. Not surprisingly, both controllers stay around the same operating point since the constraint does not affect the optimum point when $\omega = 7Hz$. As a result, both systems behave similarly after the frequency change.

4.5 Conclusion

In this Chapter, the problem of energy harvesting from base vibration in the presence of uncertainty in excitation amplitude and frequency was studied. It was shown that there is an optimum level of damping that results in maximum power extraction. It is possible to find the optimum damping for each excitation frequency using an analytical model or experimenting on the real harvester.

For optimal tuning of the energy harvester, a maximum allowable displacement can be considered. This constraint might be needed to prevent the harvester seismic mass from very large displacements that can potentially damage the harvester or take it out of the desirable operating range. Tuning of the harvester damping with this consideration was achieved by defining a constrained optimization problem, and it was shown that the constrained optimal values can result in less power regeneration compared to non-constrained optimal values.

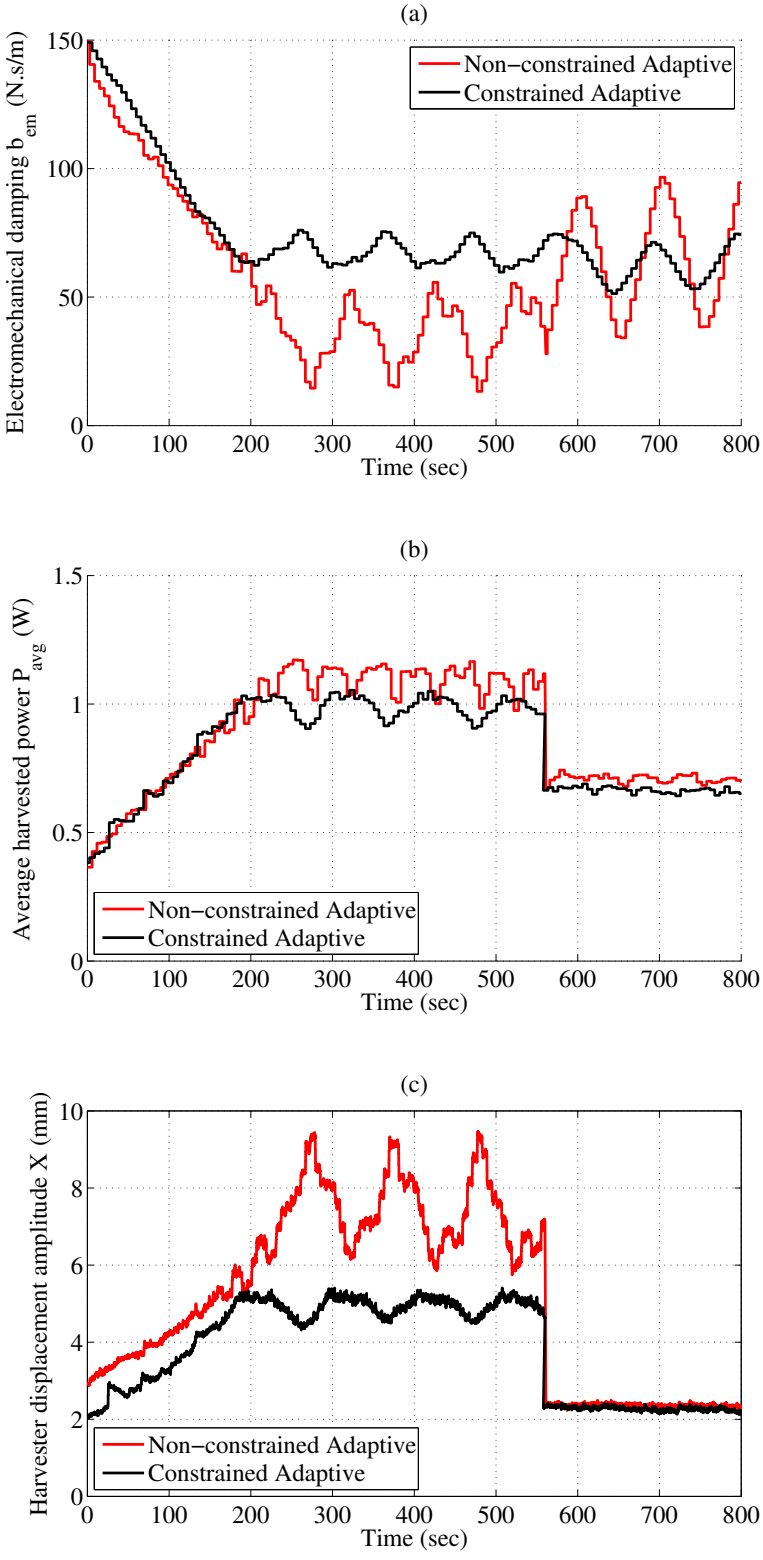

Figure 4.10: Constrained and non-constrained self-tuning for finding and tracking the maximum power point.

A sliding mode extremum-seeking algorithm was used in the vibration energy harvester with the constraint treated as a penalty term in the extremum-seeking objective function. Experimental results showed that the algorithm can obtain the maximum power point in real-time while achieving the constraint on displacement.

Chapter 5

Multi-Variable Self-Tuning for Vibration Energy Harvesting

A new control strategy for sliding-mode extremum seeking with two-variables is proposed in this Chapter. The controller converts the two-variable search problem into a single-variable problem in which the direction of changes on the two-dimensional phase plane is used as the sliding mode variable. Simulations are conducted to show that the proposed method is simpler, faster and more accurate than multi-variable sliding mode extremum seeking control methods in the current literature. The proposed controller is utilized for maximum power point tracking in vibration energy harvesters where both damping and stiffness of the harvester can be tuned using power electronic techniques. Experimental results show that the proposed controller is capable of tuning the variables for seeking the extremum point without using any model of the system.

5.1 Introduction

Extremum seeking controllers have a wide range of applications from energy systems to process control [45, 118]. They can be classified as gradient based and non-gradient based controllers. Gradient-based controllers need continuous measurement of the gradient or Hessian of the performance function, while non-gradient based controllers have the advantage of avoiding calculation of the gradient. Sliding mode extremum seeking control (SMESC), first suggested in [48], is a non-gradient method that combines sliding mode controller with extremum seeking problem. It uses a switching function to guide the system seek different directions to find the extremum.

Fast and smooth convergence besides simple implementation of SMESC motivates extension of this controller to multivariable algorithms. A simple generalization of this controller was first suggested in [98] and adopted in [44]. In this controller, n single-variable SMESCs work in a decoupled way according to the system only output. They provided a Lyapunov based stability analysis that guarantees convergence of the controller if parameters are designed properly. However, large number of design parameters and slow convergence to extremum point encourage further attempts to

design a multivariable sliding mode extremum seeking controller (MVSMESC) with a higher level of intelligence.

In most of extremum seeking applications, the system of interest comprises no more than two variables, so in this study, a novel Two-Variable SMESC (TVSMESC) is suggested, and further extension of the algorithm to higher-dimensional systems is left for future works. Using a geometrical approach, the two-variable problem is reduced back to the single-variable SMESC, and it is shown that the controller can potentially demonstrate the steepest ascent behaviour in its search for the extremum. Fast and effective advance towards the extremum point opens up new opportunities in designing model-free self-tuning energy conversion systems that have two tunable parameters. Here, the problem of shunt impedance tuning for maximum power point tracking (MPPT) in vibration energy harvesters is considered as the case study.

In this Chapter, a new two-variable extremum seeking controller is suggested. The novel controller shows faster and more accurate convergence and is easier to implement compared to its only rival reported in [98]. Other than the novel controller, two-variable maximum power point tracking (MPPT) is accomplished for the first time in the application of vibration energy harvesters.

The structure of this Chapter is as follows: In Section 5.2, the novel extremum seeking controller is introduced and compared to the state of the art. Also, a geometrical interpretation of the system behaviour is provided to explain how the new algorithm finds the extremum point and stays at its neighbourhood. In Section 5.3, the controller is applied to vibration energy harvesters. First, optimal shunt damping and stiffness levels of an electromagnetic energy harvester are calculated, and the effect of frequency-domain tuning on harvested power is studied. Then, MatLab simulations are conducted to show how the new controller tunes the variables to find the optimal values and adapt to frequency changes.

5.2 Two-Variable Sliding Mode Extremum Seeking

5.2.1 Control Structure

In the single variable sliding mode extremum seeking control, the objective function is made to follow a reference increasing/decreasing function until it reaches the extremum point. The error between the output and the reference signal is fed into a switching function (sliding mode controller), and the resulting signal is integrated over time to calculate the input variable. An extension of the single variable controller was suggested in [98] as depicted in Fig. 5.1, in which the controller assumes a decoupled relationship between the two inputs and the final output y. This can result in poor performance of the system in terms of convergence time, response smoothness and accuracy.

To alleviate the above problems, the controller shown in Fig. 5.2 is suggested in this work. As an extension of the above work, we utilize only one sliding surface. The error between the system output and the reference signal is multiplied by a gain $\frac{\pi}{\alpha}$. The result θ can be considered as the direction (or angle) of the *velocity vector* of the extremum seeking variables $[\dot{x}_1, \dot{x}_2]$. The term θ

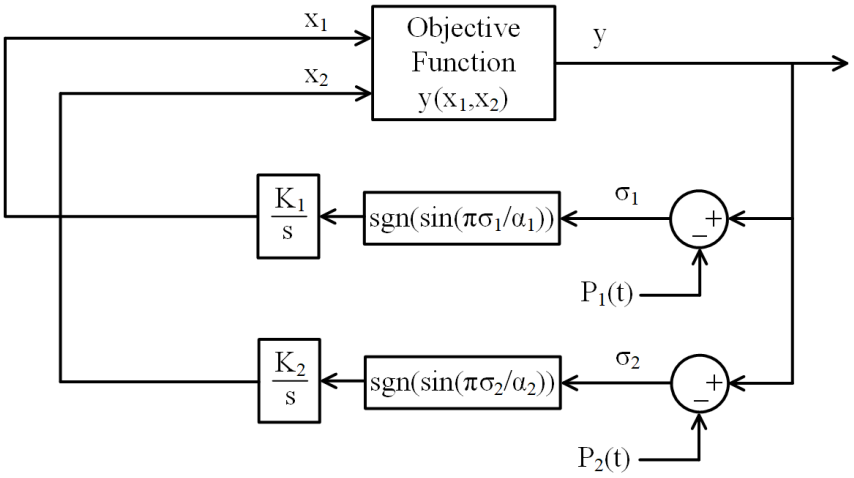

Figure 5.1: Schematic view of the MVSMESC proposed by Toloue *et al.*[98]

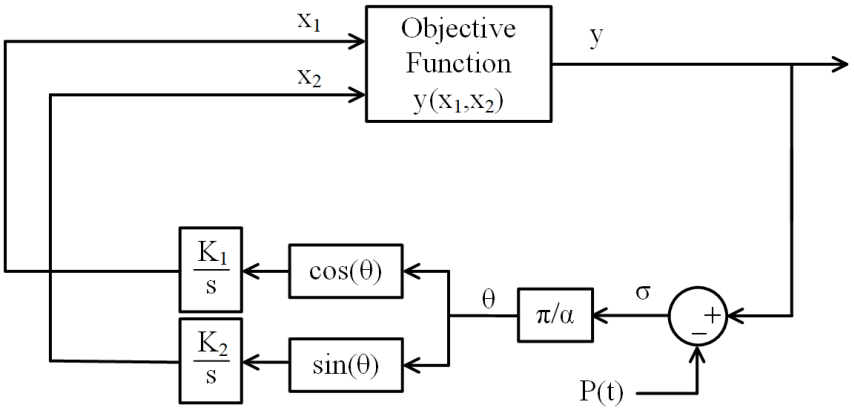

Figure 5.2: Schematic view of the proposed two-variable SMESC

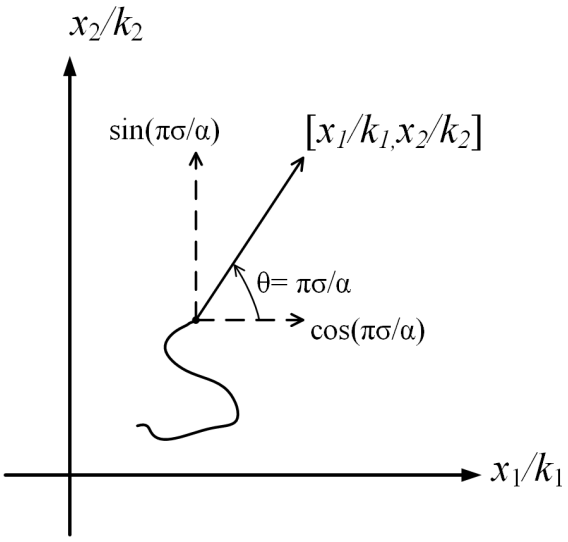

Figure 5.3: Angle of state velocity vector θ

is used for calculating $\dot{x}_1$ and $\dot{x}_2$ using expressions $\cos(\theta)$ and $\sin(\theta)$, respectively. The results are multiplied by gains k_i and integrated over time to calculate the extremum seeking variables.

As explained above, the previous multivariable SMESC is now converted into a single-variable controller that calculates only θ using a sliding mode algorithm (Fig. 5.2). Using this method, the number of design parameters reduces from 6 (in the previous version) to 4 in this controller. This means that the new system has two less design parameters compared to the previous approach [98].

5.2.2 Geometrical Interpretation

Using the controller structure shown in Fig. 5.2, the normalized rate of change of the input variables can be derived as

$$\frac{\dot{x}_1}{k_1} = \cos(\frac{\pi\sigma}{\alpha}), \tag{5.1}$$

$$\frac{\dot{x}_2}{k_2} = \sin(\frac{\pi\sigma}{\alpha}). \tag{5.2}$$

It can be easily inferred that the angle $\frac{\pi\sigma}{\alpha}$, also shown as θ, is the direction of changing the input variables on a phase plane normalized with respect to k_1 and k_2 (Fig. 5.3). The system's normalized operating point in the phase plane keeps moving with a constant speed of 1 and the variable angle θ. It is expected that the angle θ is calculated reasonably to navigate the system states towards the extremum point. Since the speed of the state vector does not change in the search, the state of the system would keep rotating around the extremum point when the extremum is achieved.

The functionality of the control structure is pretty much dependent on the navigation angle $\theta = \frac{\pi\sigma}{\alpha}$. The sliding mode controller error σ is calculated as the difference between the plant output and the sliding surface. Here, we assume a maximum-seeking controller, so a ramp function with positive slope is picked as the reference signal $p(t)$ [31, 70]. If the plant output y increases with

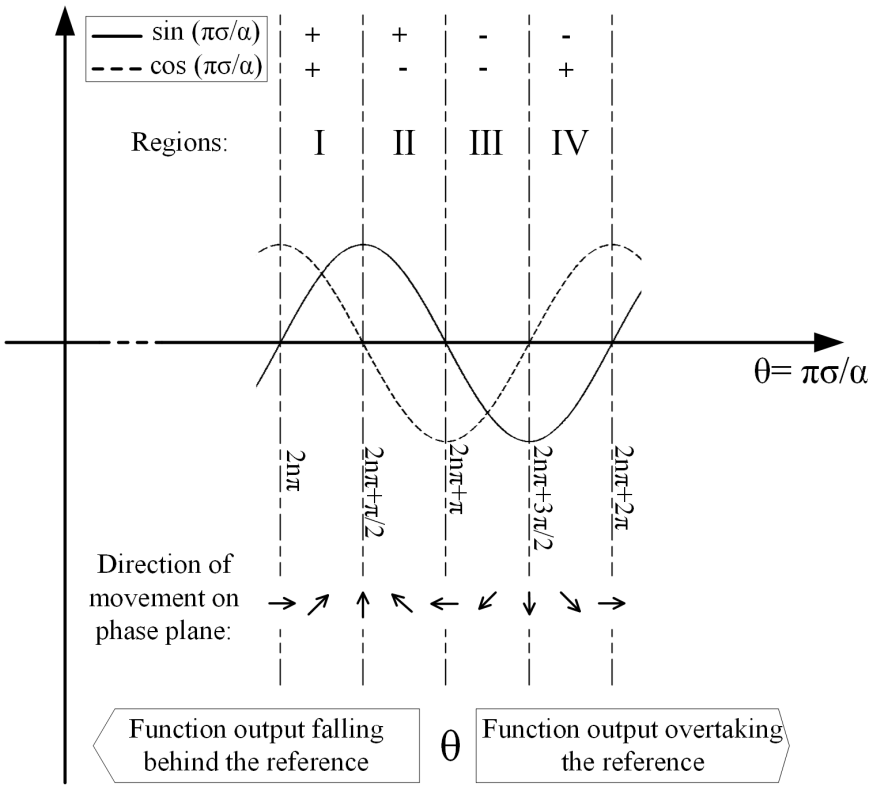

Figure 5.4: Effect of sliding mode error on direction of movement on the phase plane

a higher pace compared to the reference ramp, σ increases. Alternatively, if y increases with a lower rate compared to $p(t)$ or if it decreases, σ keeps decreasing. It is possible to explore different scenarios on how the system behaves while seeking for the extremum.

Fig. 5.4 illustrates how changing θ increases or decreases each state variable. There are four different regions that are repeated sequentially with respect to θ. In the region denoted as region I, both $\cos(\theta)$ and $\sin(\theta)$ functions are positive, meaning that both state variables increase. In this case, the state velocity vector faces a direction between the positive directions of x and y axes. If θ lies in region II, the state velocity vector faces upward and inclined to left. As a result, x_1 decreases but x_2 keeps increasing. Considering the other regions and points between them, the direction of movement in the phase plane covers 360 degrees. This makes it possible for the controller to find its direction toward the extremum point.

In the following, we describe how the sliding mode controller obtains the path toward the extremum point. Let us assume that, in a maximum-seeking scenario, the angle θ is in the proper region (*e.g.,* region I). Two scenarios are expected depending on whether the output y is increasing faster or slower than the reference signal. If y tends to overtake the reference signal, the angle θ increases (Fig. 5.4). In other words, the direction of movement in the phase plane deviates to its left. This continues by the time that the rate of increase of y is no longer larger than that of the reference signal because of deviating too much from the correct direction. As a result, the function

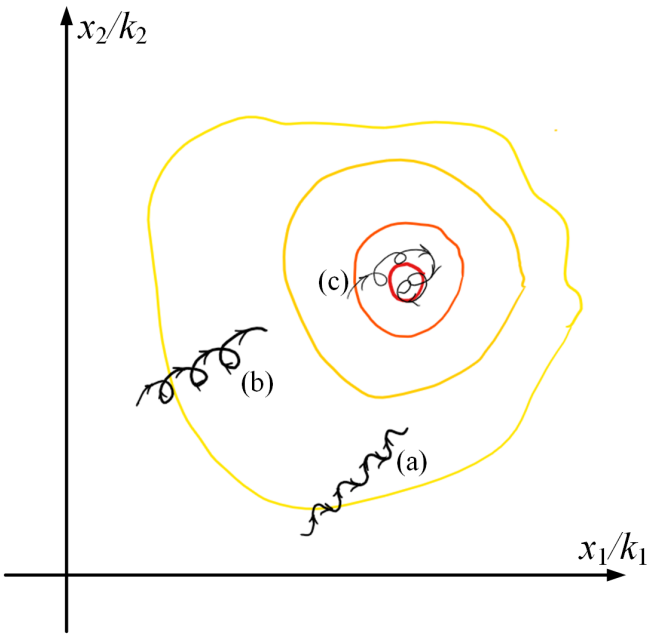

Figure 5.5: Different types of approaching the extremum point

output starts falling behind the reference signal and θ starts decreasing (starts turning to right). By the time this sequence continues to occur, the sliding mode controller tracks the reference signal and the function output increases with the same rate as the sliding ramp $p(t)$. In this case, the trace of the state trajectory on the phase plane would be like a winding path as shown in Fig. 5.5 curve (a).

Another scenario is when the function output increases more slowly than the reference signal or does not increase at all. In this case, θ starts decreasing, and the state velocity vector keeps turning right. If in passing through the four different regions, it happens that $\dot{y}$ becomes larger than $\dot{p}(t)$, the case explained in the previous paragraph occurs, but if $\dot{p}(t)$ turns to be always larger, the state velocity vector keeps turning to right. This might be considered unstability in terms of the sliding mode control, but it will be shown that even this oscillatory behaviour results in drifting toward the extremum point.

The scenario explained above is more likely to happen when the reference signal is designed to be too steep or the plant function is close to the extremum point. Under these conditions, the output y fails to catch up with the reference signal $p(t)$, and θ continuously decreases. It keeps passing through the four regions in the reverse direction over and over again. Even in this case, in at least one of the four regions, $\dot{y}$ should be positive but not as large as $\dot{p}(t)$. When θ is in that region, the system output does a relatively good job in following the reference signal. As a result, θ decreases with a lower rate compared to the other regions and it takes more time for it to exit the region. In other words, θ stays in the correct direction for a longer time and sweeps the other directions more quickly. This behaviour ends up in a rotational motion in the phase plane that

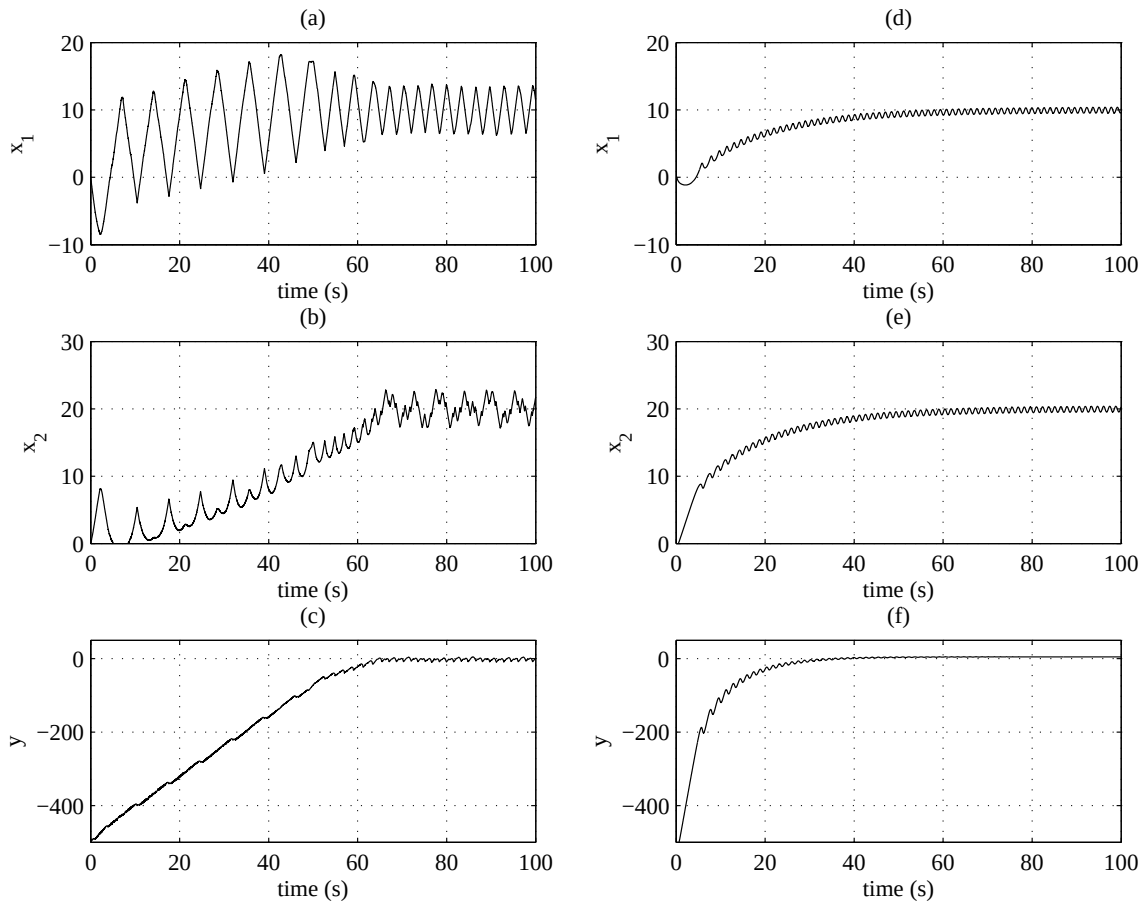

Figure 5.6: (a-c) Extremum Seeking using the decoupled MVSMESC (d-f) Extremum Seeking using the novel ESC proposed in this study

moves towards the maximum point. Almost the same thing happens when the system reaches the extremum. The function output is no longer able to increase; hence the system keeps rotating around the function's maximum value. Curves (b) and (c) in Fig. 5.5 show the system behaviour in these cases, respectively.

5.2.3 Simulations for Comparison with the Previous Version

To compare the behaviour of the proposed Two-Variable controller with the MVSMESC in [98], simulations are done on a simple static two-variable function as follows.

$$y(x_1, x_2) = 5 - (x_1 - 10)^2 - (x_2 - 20)^2. \tag{5.3}$$

The two controllers are supposed to seek the extremum point $y = 5$ at point $[x_1, x_2] = [10, 20]$ with the initial values starting from $[x_{1_0}, x_{2_0}] = [0, 0]$. Simulation results are provided in Fig 5.6.

In Fig. 5.6, the three plots on the left show extremum seeking using the previous method (MVSMESC), and the three curves on the right show the system response using the new method.

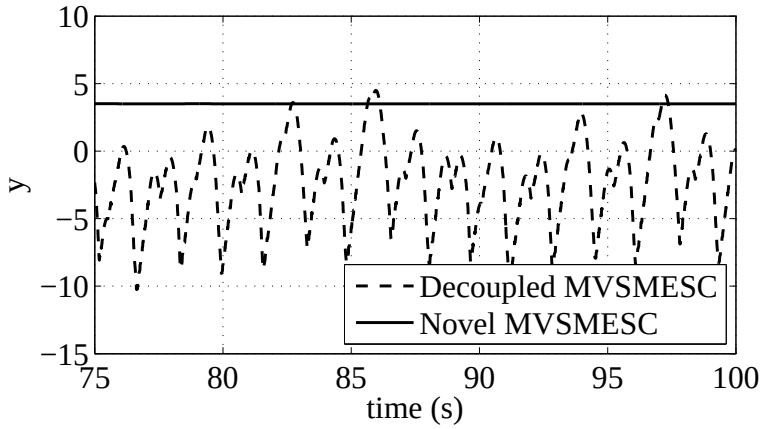

Figure 5.7: Comparison of the two extremum-seeking methods in reaching the extremum value (zoomed view)

Both controllers converge to the optimum set of $[x_1, x_2] = [10, 20]$, but MVSMESC shows oscillations around the optimum point. Moreover, the proposed method has a faster convergence time.

Figure 5.7, shows the output y for both controllers in a closer view. It shows that MVSMESC does not converge to the extremum point $y = 5$, whereas the proposed method results in reaching the extremum point accurately.

Finally, Fig. 5.8 provides a comparison of both methods in the phase plane. Trajectories show that the new method has a better convergence. Interestingly, the new method behaves like a steepest ascent algorithm that takes the closest route to the extremum point.

5.3 Application in Self-Tuning Vibration Energy Harvesters

As a practical case study, the proposed controller is utilized in electrical tuning of a vibration energy harvester (VEH) as a maximum power point tracking (MPPT) algorithm. In the system under study, a power electronics circuit is used for creating a variable impedance in the shunt circuit of a VEH. It has been shown that the electrical impedance results in controllable mechanical damping and stiffness in the VEH [42]. Damping and stiffness levels are used as the extremum seeking variables for maximizing the harvested power in different frequencies without any knowledge of the harvester model.

5.3.1 Electromechanical Modeling

For a basic analysis on the effect of shunt impedance on the regenerated power in a base-excited energy harvester, a mass-spring system comprising an electromagnetic actuator with a shunt circuit is assumed. As shown in Fig. 5.9, the proposed external shunt circuit has one negative resistance and one negative inductance to cancel the internal impedance of the machine. A parallel RL circuit with variable parameters is synthesized in the circuit in an attempt to add electromagnetic damping

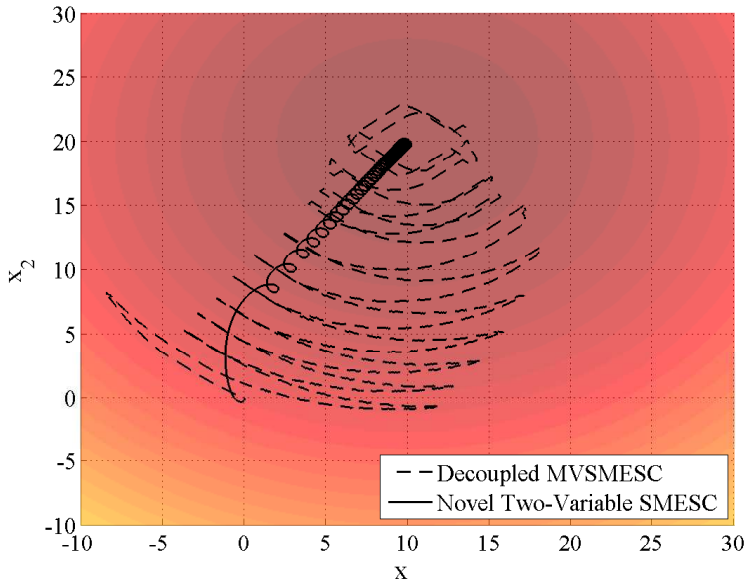

Figure 5.8: Comparison of the variables trajectories between the two methods

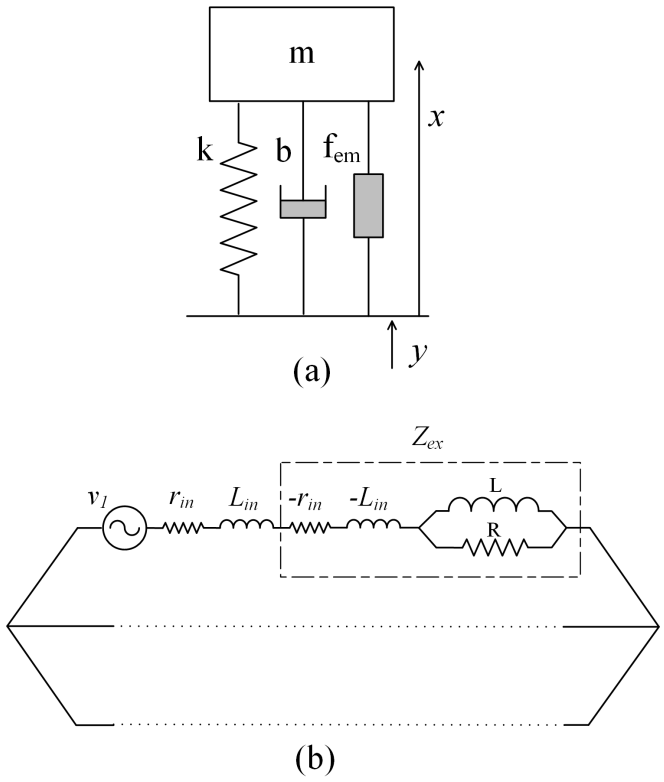

Figure 5.9: (a) Electromagnetic vibration energy harvester (b) Harvester shunt circuit

and stiffness to the system. The above system can be built using a switched-mode power electronic converter connected to the motor terminals on one side and a DC source on the other side [42].

Electromechanical damping and stiffness of the system can be written as

$$b_{em} = \frac{{c_{em}}^2}{R}, \tag{5.4}$$

$$k_{em} = \frac{{c_{em}}^2}{L}, \tag{5.5}$$

where c_{em} is the electromechanical coupling constant of the actuator defined as

$$c_{em} = \frac{f(t)}{i(t)}, \tag{5.6}$$

where $f(t)$ and $i(t)$ are the actuator force and current respectively. The average regenerated power for a single-harmonic base excitation can be derived as

$$P_{avg} = \frac{3}{4}|X|^2\left(\omega^2(b_{em} - \frac{r_{in}}{{c_{em}}^2}{b_{em}}^2) - \frac{r_{in}}{{c_{em}}^2}{k_{em}}^2\right), \tag{5.7}$$

where $|X|$ is the amplitude of the relative displacement of the mass [42]. It should be noted that the vibration system, including the actuator force, has a combination of passive (mechanical) and active (electromagnetic) damping and stiffness terms. Hence, the system's relative displacement can be obtained as follows

$$|X| = \frac{m\omega^2 Y}{\sqrt{(k + k_{em} - m\omega^2)^2 + (b + b_{em})^2\omega^2}}, \tag{5.8}$$

where Y is amplitude of base displacement. Using (5.7) and (5.8), the closed form expression for the harvested power can be written as

$$P_{avg} = \frac{3}{4}\frac{m^2\omega^4 Y^2\left(\omega^2(b_{em} - \frac{r_{in}}{{c_{em}}^2}{b_{em}}^2) - \frac{r_{in}}{{c_{em}}^2}{k_{em}}^2\right)}{(k + k_{em} - m\omega^2)^2 + (b + b_{em})^2\omega^2}. \tag{5.9}$$

In (5.9), the average power harvested by the EMEH is given as a function of input excitation characteristics (ω and Y), electromagnetic damping (b_{em}) and stiffness (k_{em}) respectively. In the case of single-harmonic excitations, the parameters b_{em} and k_{em} should be optimized for maximum power. To this end, the partial derivatives of P_{avg} is taken with respect to b_{em} and k_{em} and set equal to zero as follows

$$\frac{\partial P_{avg}}{\partial b_{em}} = 0, \tag{5.10}$$

$$\frac{\partial P_{avg}}{\partial k_{em}} = 0. \tag{5.11}$$

Table 5.1: Parametric values of the multi-variable self-tuning test setup

Parameters	Value
mechanical stiffness, k	$12000N/m$
mechanical damping, b	$40N.s/m$
mass, m	$10kg$
motor phase resistance, r_{in}	4.9Ω
actuator inductance, L_{in}	$2.15mH$
electromechanical coupling constant, c_{em}	$43N/A$

Solving (5.10) and (5.11) simultaneously for $b_{em,op}$ and $k_{em,op}$ results in optimal electromagnetic damping and stiffness as follows

$$b_{em,op} = \frac{\hat{b}\Big((k-m\omega^2)^2 + b(b+\hat{b})\omega^2\Big)}{(k-m\omega^2)^2 + (b+\hat{b})^2\omega^2}, \tag{5.12}$$

$$k_{em,op} = \frac{\omega^2\hat{b}^2(m\omega^2-k)}{(k-m\omega^2)^2 + (b+\hat{b})^2\omega^2}, \tag{5.13}$$

where

$$\hat{b} = \frac{c_{em^2}}{2r_{in}}. \tag{5.14}$$

The term $\hat{b}$ is interpreted as the EM damping when the shunt circuit is purely resistive with resistance $2r_{in}$.

For a better understanding of the equations derived so far, a set of realistic parameters are assumed to plot the expressions for average power P_{avg}, optimal electromagnetic damping $b_{em,op}$ and stiffness $k_{em,op}$ in a frequency sweep. Using the values in Table 5.1, the harvester natural frequency can be calculated as

$$\omega_n = \frac{1}{2\pi}\sqrt{\frac{k}{m}} = 5.51Hz, \tag{5.15}$$

which is almost in the middle of the simulation frequency range. It is assumed that the harvester is originally designed to harvest energy in its own natural frequency $5.51Hz$. However, the harvester is simulated in frequencies ranging from $\omega = 0$ to $10Hz$.

For the self-tuning harvester, the optimal stiffness and damping levels are calculated using (5.12) and (5.13) at each frequency. It is assumed that the harvester adopts the optimal values. The optimal EM damping and stiffness are plotted in Figs. (5.12) and (5.13). The harvested power is shown in Fig. 5.12. For comparison, behavior of a non-adaptive harvester designed for $\omega = 5.51Hz$ is plotted.

As seen in Fig. 5.10, in a non-adaptive harvester, the electromechanical damping is designed for its natural frequency using (5.12) and remains constant in the whole frequency range ($b_{em} =$

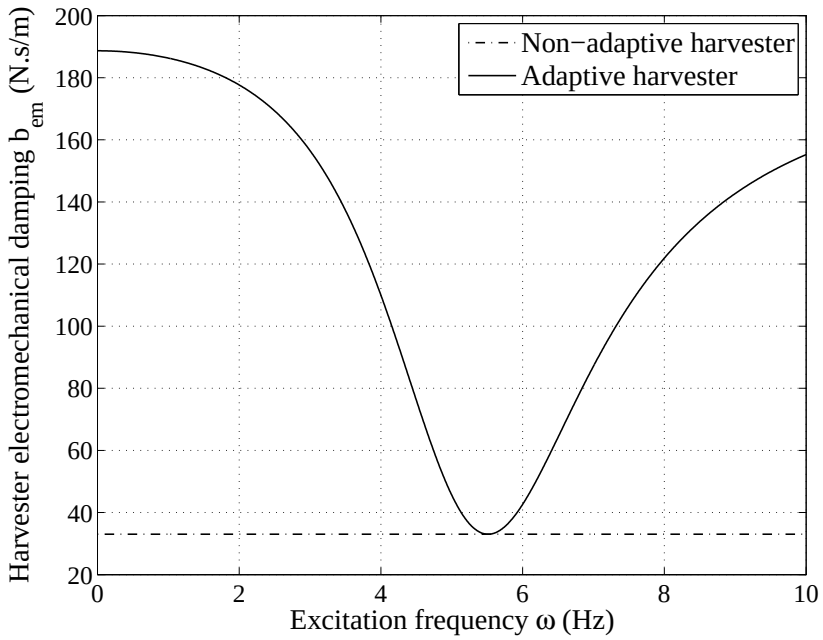

Figure 5.10: Comparison of electromechanical damping for adaptive and non-adaptive approaches

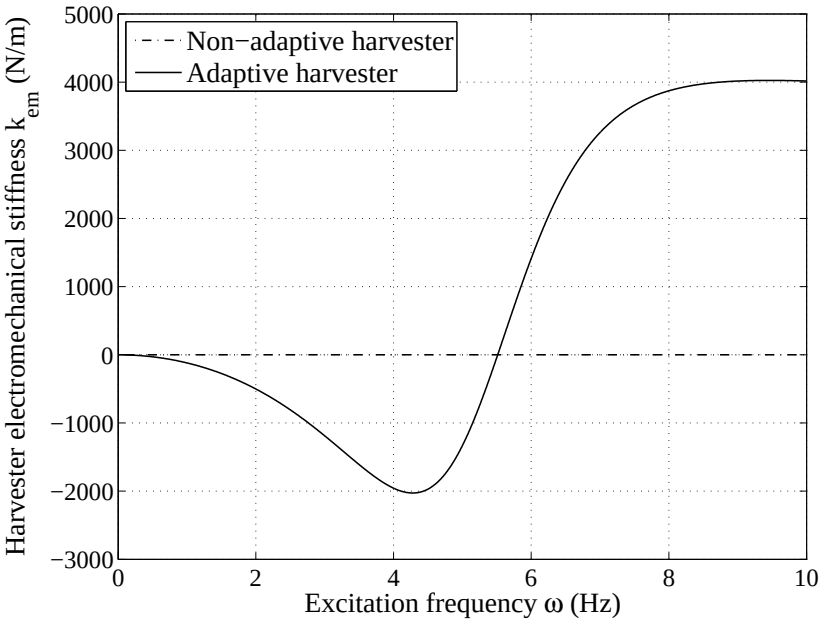

Figure 5.11: Comparison of electromechanical stiffness for adaptive and non-adaptive approaches

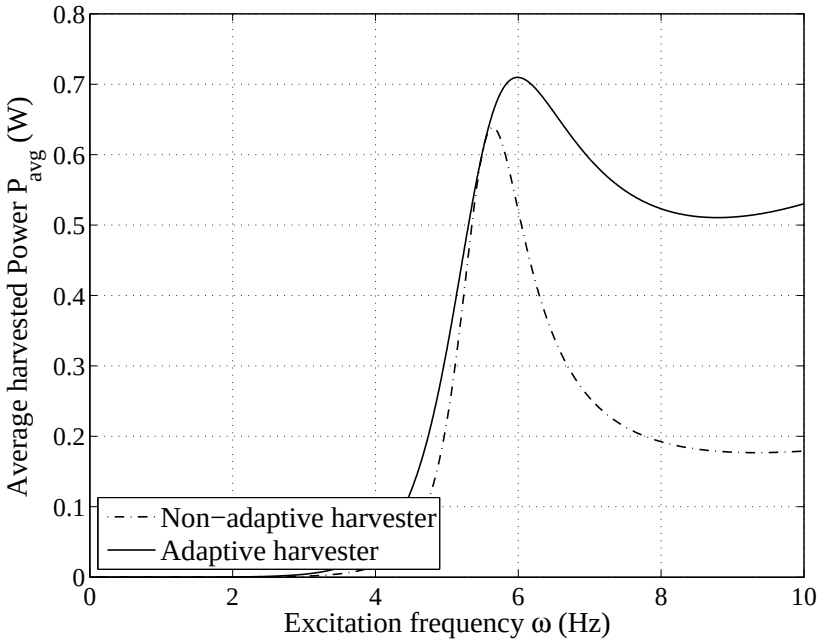

Figure 5.12: Comparison of harvested power for adaptive and non-adaptive approaches

$33N.s/m$). For the adaptive harvester, $b_{em,op}$ reaches a minimum at harvester's natural frequency, which is equal to damping of the non-adaptive harvester. At other frequencies, optimum EM damping is higher than the original value.

In Fig. 5.11, k_{em} is zero for the non-adaptive harvester since the natural frequency of the harvester is already equal to the design frequency $\omega = 5.51Hz$. In contrast, optimal electromagnetic stiffness, $k_{em,op}$, changes in frequencies different from the original value. If the excitation frequency is higher than the harvester natural frequency, $k_{em,op}$ takes positive values, while lower input frequencies require a negative electromagnetic stiffness. These observations can be easily explained considering the fact that the system resonance frequency should be as close as possible to the excitation frequency. If $\omega > \omega_n$, the system should increase its own stiffness to match its own resonance frequency with the input excitation; hence positive electromagnetic stiffness is required. Similarly, at lower frequencies ($\omega < \omega_n$), negative values for k_{em} are needed to decrease the resonance frequency.

Figure 5.12, shows the resulting harvested power for the two energy harvesting approaches. The non-adaptive power has a peak at its natural frequency. For input frequencies higher or lower than ω_n, the harvested power decreases significantly. This behaviour negatively impacts the harvester efficacy and is the main motivation of adding a form of adaptiveness to a VEH. The self-tuning harvester, as plotted, shows a wider bandwidth, which results in more energy regeneration compared to the non-adaptive harvester.

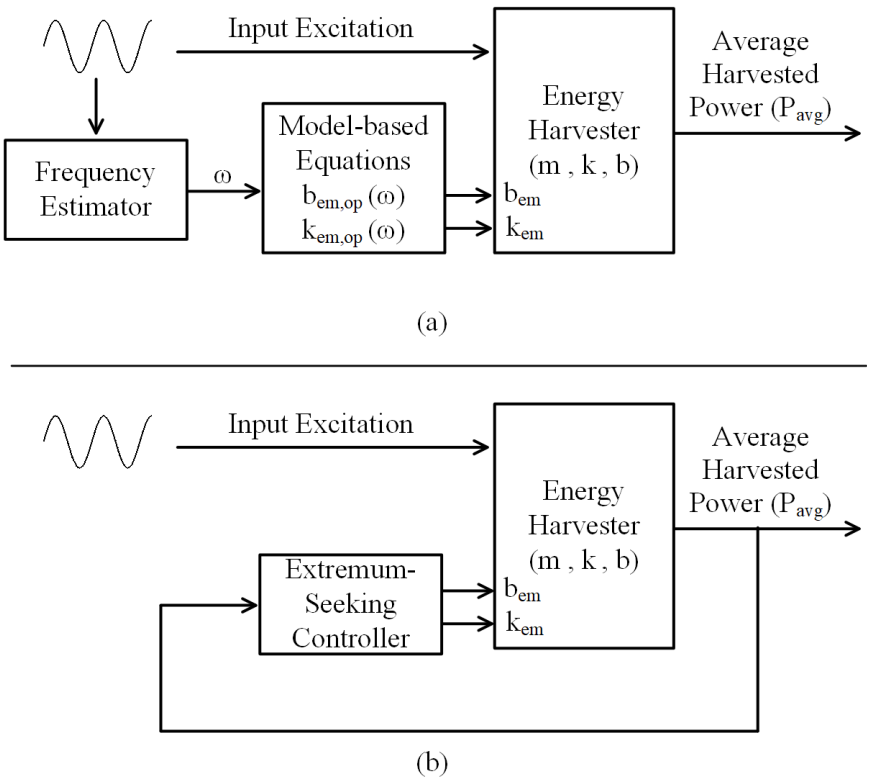

Figure 5.13: (a) Open-loop, model-based self-tuning energy harvester (b) Closed-loop, model-free adaptive energy harvester

It was shown that proper tuning of electromagnetic damping (b_{em}) and stiffness (k_{em}) can maximize harvested power at each given frequency. The simplest structure for implementing this adaptiveness would be a model-based system shown schematically in Fig. 5.13(a).

In this system, the frequency of the input excitation should be estimated at each control cycle. Then, optimum b_{em} and k_{em} are calculated using (5.12) and (5.13). The system impedance should be updated according to the calculated values to make the harvester track the optimal operating point. In this system, P_{avg} is not used as a control feedback, and the control algorithm relies on the system parameters (m, k and b) for tuning electromagnetic damping and stiffness. As a result, the self-tuning system is not able to adapt to any change in the system parameters or any other unmodeled effect.

As a more appropriate solution for the adaptive energy harvesting problem, the sliding mode extremum-seeking controller introduced in Section 5.2 is utilized. The harvested power is considered as the output function, and EM damping and stiffness (b_{em} and k_{em}) are treated as the extremum-seeking variables 5.13(b). Experimental results are provided in the following.

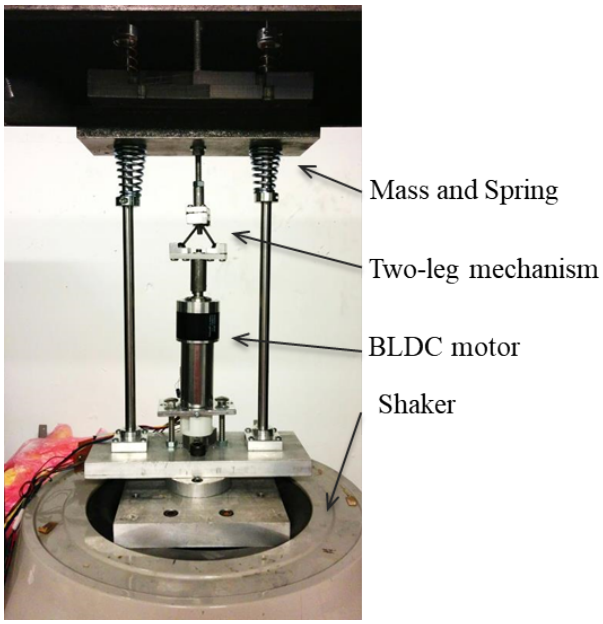

Figure 5.14: Vibration energy harvester used in experiments

5.3.2 Experimental Results

To investigate performance of the proposed extremum seeking controller in tuning VEHs, the algorithm was implemented on a dSpace real-time control hardware with control loop frequency $f_s = 50kHz$. A mass-spring structure comprised of an electromagnetic harvester was utilized as the VEH. The harvester is a combination of the 3-phase brushless DC motor (EC-MAX 283873 from Maxon, Inc.) and a two-leg mechanism for converting linear motion into rotational motion (see [58]). The three-phase full bridge power electronics converter DRV8305 (from Texas Instruments) was used for electrical current control and creating the desired shunt impedance. The energy harvester is shown in Fig. 5.14 with its parameters provided in Table 5.1.

Before testing the extremum seeking algorithm, some experiments were first conducted by sweeping a range of electromagnetic damping and stiffness levels and measuring the harvested power. These experiments are necessary to acquire a two-dimensional experimental model of the system that can later be used to check if the controller converges to the correct extremum points. For each excitation frequency, a surface was fitted on the measured values as shown in Figs. 5.15 and 5.17. It is needed to explain that the experiments were limited to excitation frequencies that are close to the resonance frequency of the available energy harvester. The main reason is that in frequencies far away from the resonance frequency, the harvester used in the experiments undergoes very small displacements. As a result, the regenerated power levels are too low to be effectively captured by the measurement system. Consequently, frequencies $\omega = 5.51Hz$ and $\omega = 6.5Hz$ were used in experiments as explained below.

In the first test, the energy harvester was excited with its own resonance frequency ($\omega = 5.51Hz$). The initial values of the tuning variables were set as $[b_{em}, k_{em}] = [120N.s/m, 1500N/m]$.

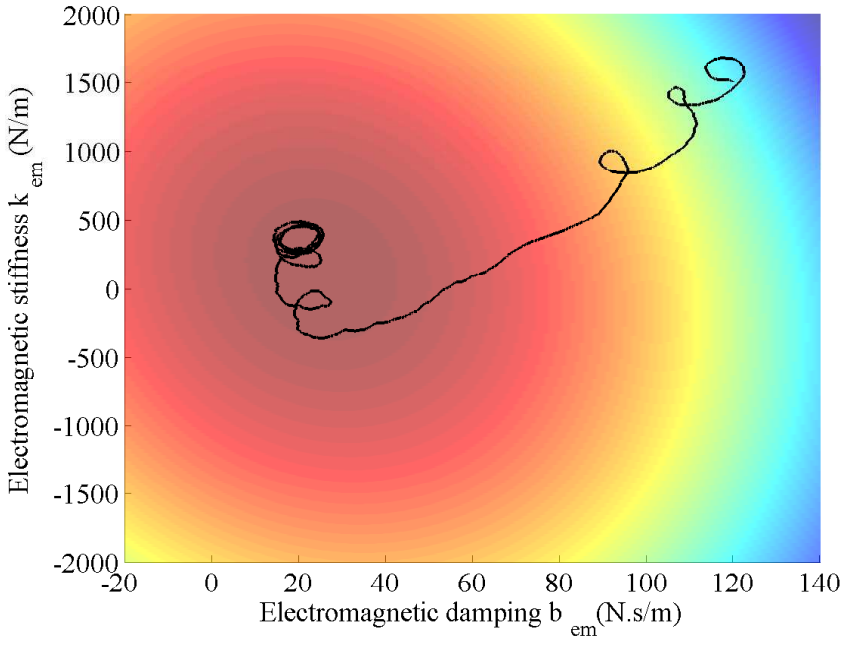

Figure 5.15: Trajectory of EM damping and EM stiffness toward the extremum point when $\omega = 5.51Hz$, comparison with the surface fit on the identification results

Changes in the tuning variables and the resulting harvested power are shown in Fig. 5.16. As shown in the Fig., electromagnetic damping approximately converges to $b_{em} = 20N.s/m$ while electromagnetic stiffness moves to values around $k_{em} = 400N/m$. The trajectory of the system in seeking the extremum point is plotted in Fig.5.15. It can be easily seen that the tuning variables have moved the system to the extremum point.

In the next experiment, the system was excited with a frequency of $\omega = 6.5Hz$, which is slightly larger than its resonance frequency. This is when the system is detuned from the dominant excitation harmonic, or the excitation frequency changes from the expected value used in design of the harvester. The same identification experiment was conducted to find the extremum point of the system. As shown in Fig. 5.18, the optimum values are around the point $[b_{em}, k_{em}] = [50N.s/m, 900N/m]$. Changes of the input and output variables with time are shown in Fig. 5.18. It can be inferred from the above figure that tuning variables have converged to the optimum values, and the extremum is sought.

It is noticed that the power regenerated in the experiments is less than what is expected from the analytical methods. This can be attributed to the power losses of higher-order harmonics in the controlled current. The actuator current oscillates around its reference value, which results in additional conduction losses. As a result, a portion of the power is wasted in the actuator, and less power is regenerated. This effect is more evident in Fig. 5.18 where the harvester back emf voltage levels are smaller. To resolve this problem, the DC voltage of the power converter needs to be tuned

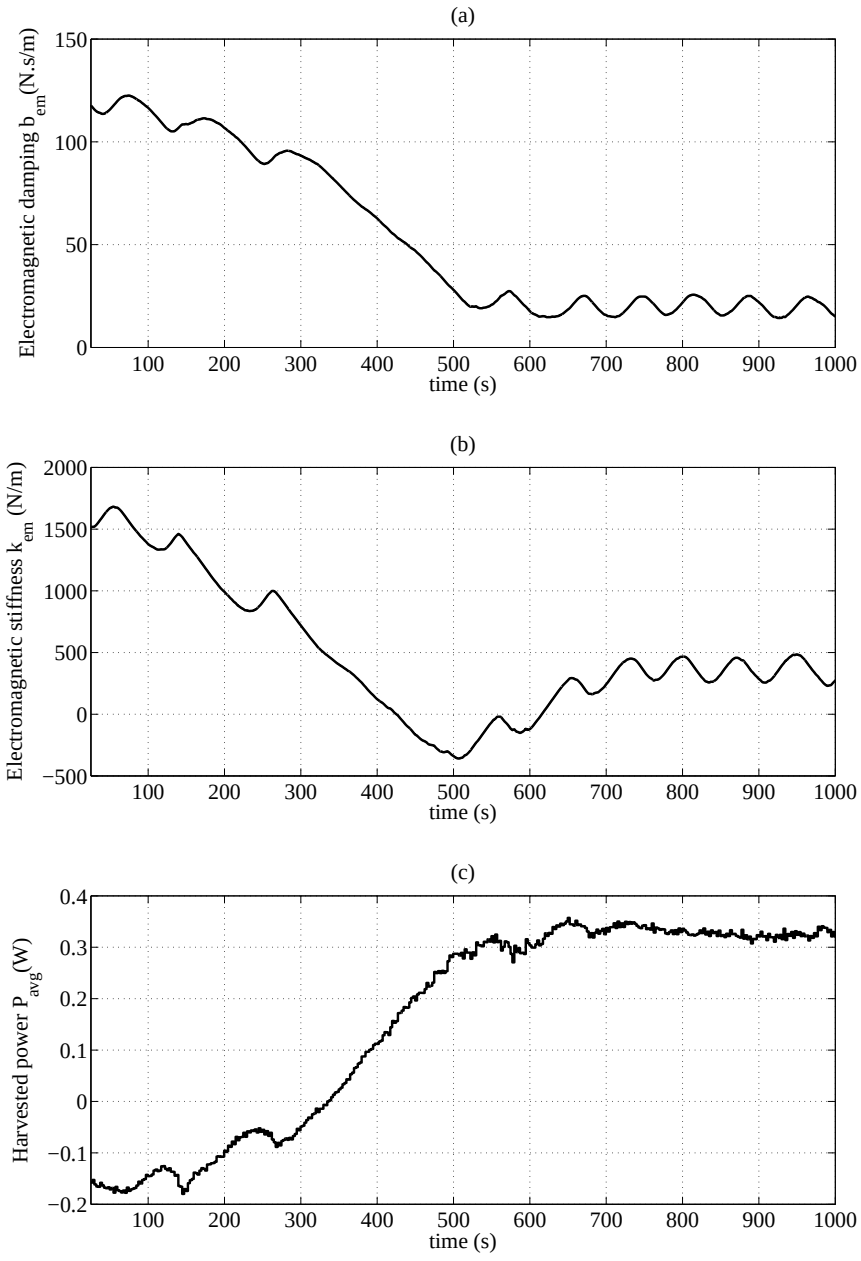

Figure 5.16: Two-variable extremum seeking with EM damping and stiffness for maximizing power when $\omega = 5.51Hz$, (a) EM damping b_{em}, (b) EM stiffness k_{em}, (c) Average harvested power P_{avg},

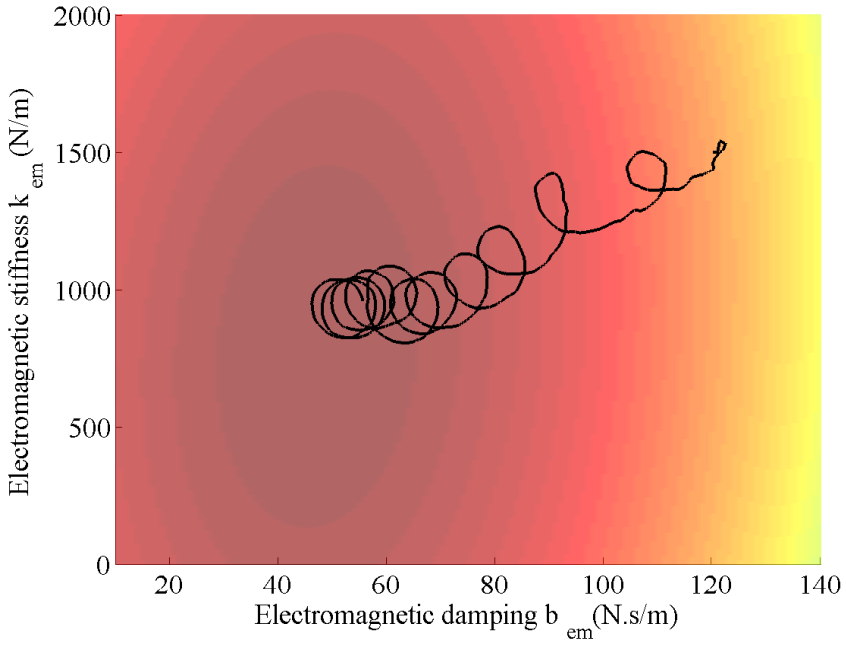

Figure 5.17: Trajectory of EM damping and EM stiffness toward the extremum point when $\omega = 5.51Hz$, comparison with the surface fit on the identification results

based on the actuator operating conditions. This needs to be addressed in a separate study with more focus on power electronics design and control.

It is also observed that it takes a while for the controller to converge to the optimum points. This is mainly due to the fact that the initial conditions have been selected to be far away from the optimum point. As the result, the harvester remains in the energy consuming region for a while and starts harvesting energy when it gets close enough to the optimum point. To reduce the convergence time in practice, it is recommended to start the system with initial conditions that are close to the optimum point. This can be achieved using a model of the harvester. In other words, it is suggested to combine the novel model-free extremum seeking controller with a model-based controller that provides the system with better initial conditions.

5.4 Conclusion

A new two-variable sliding mode extremum seeking controller was introduced and a geometrical interpretation of the controller behaviour was provided. It was shown that the new controller has less number of design parameters and shows better performance in finding the extremum point. As a case study, a two-variable maximum power point tracking problem with application to vibration energy harvesting is investigated. Using power electronics and control an RL shunt circuit for is synthesized for the energy harvester. This results in realization of tunable electromagnetic damping and stiffness. The generated damping and stiffness were considered as the tuning variables for maximizing the

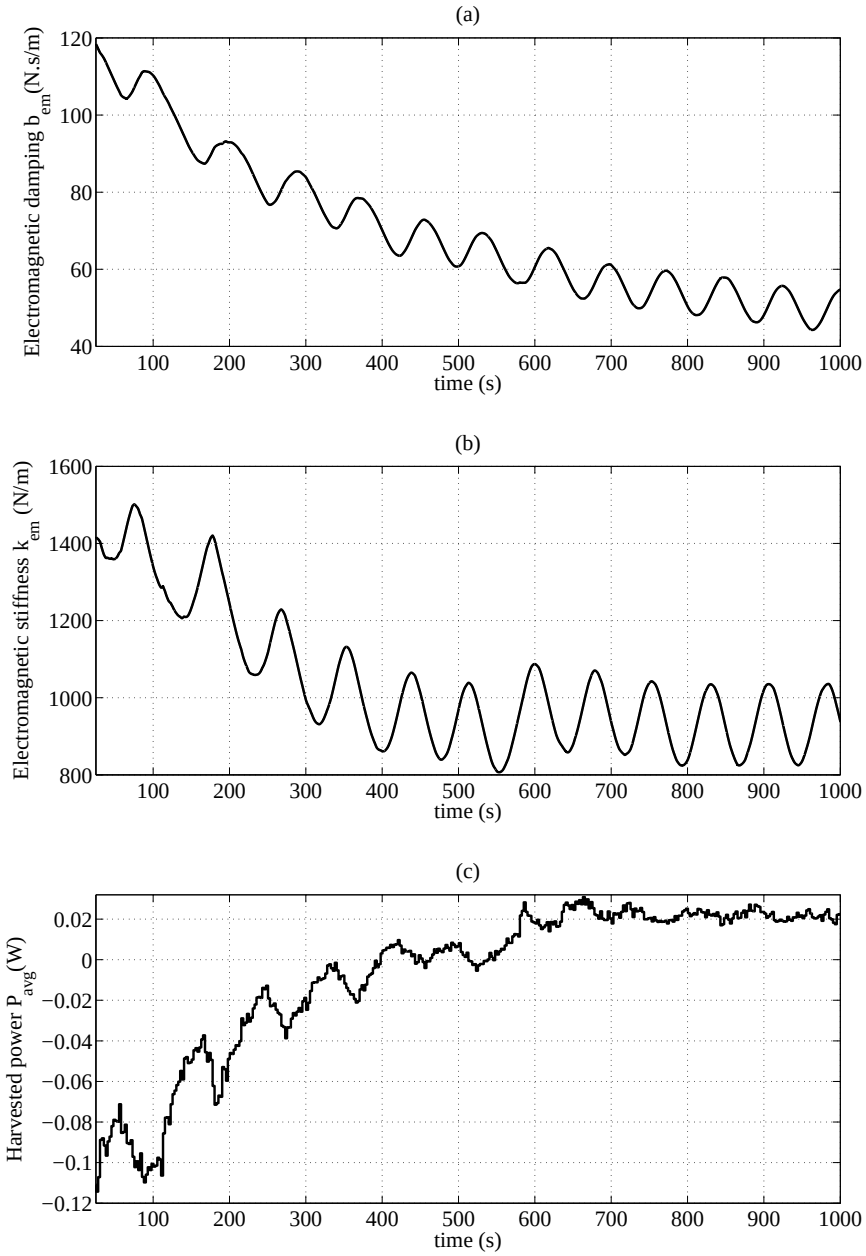

Figure 5.18: Two-variable extremum seeking with EM damping and stiffness for maximizing power when $\omega = 6.5Hz$, (a) EM damping b_{em}, (b) EM stiffness k_{em}, (c) Average harvested power P_{avg},

regenerated power. A mathematical analysis was presented to show that proper tuning of the two variables in each excitation frequency can improve the energy harvesting bandwidth. The system can achieve proper tuning using the proposed two variable extremum seeking controller which can make the system robust against model uncertainties and parameter changes. A number of experiments for vibration energy harvesting were conducted which indicate that the suggested method has the ability to find the extremum point and maximize the harvested power.

More complicated scenarios still need to be explored for the application of the self-tuning controller in vibration energy harvesting. For example, self-tuning under random excitation is a more challenging case that needs further theoretical and experimental studies. It is also suggested to combine the proposed model-free algorithm with a model-based controller to start the extremum seeking from a point which is closer to the real extremum. This would probably help the system to find the extremum point in a shorter convergence time. Both ideas are suggested for future studies.

Chapter 6

Constrained Self-Tuning Vibration Absorbers with Variable Damping and Stiffness

In this Chapter, an electromechanical actuator is utilized for bidirectional power flow in a tuned mass damper (TMD). The actuator force is controlled to achieve desired mechanical damping and stiffness values for the whole system by controlling the current using a power electronic converter. The resulting TMD can autonomously change its damping and stiffness values to minimize a host structure's displacement under different excitation frequencies. A multi-variable sliding mode extremum-seeking algorithm is used to tune the TMD damping and stiffness levels to optimal values. Analytic and simulation results show that the active TMD exhibits better performance when compared to non-adaptive and robust TMDs.

6.1 Introduction

As explained in Section 1.2.2, vibration absorbers or tuned mass dampers are used for controlling vibrations in different applications including civil structures and vehicles. They are resonating mechanical structures that create forces to absorb the extra energy in a vibrating structure.

In this Chapter, an active-regenerative electromagnetic actuator is proposed to be used in a hybrid TMD to make it tunable in terms of its overall damping and stiffness. The SMESC is used as a model-free tuning algorithm to make the system self-adaptive to changes in the excitation frequency. The inputs are constrained to operate the system in the energy-regenerative mode and guarantee stability of the vibration system. The result is a self-powered and self-tuning TMD. It is shown that the performance of the system is improved over non-adaptive systems when the excitation frequency drifts away from the original values. The paper presents electromechanical modelling of the host structure combined with the hybrid TMD. The range of damping and stiffness values in which the system remains self-powered are obtained followed by the optimum inputs for a range of frequencies. The behavior of the self-tuning algorithm is simulated to verify its convergence to optimum values.

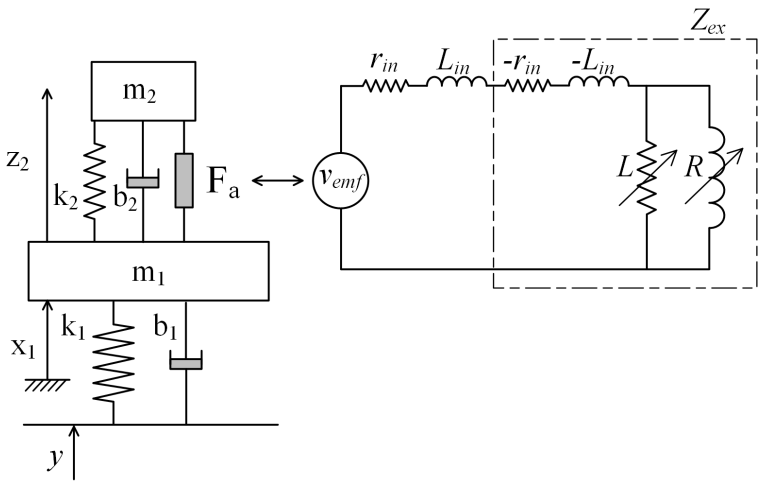

Figure 6.1: Schematic view of the active TMD and its shunt circuit

6.2 Electromechanical Modeling

The system under study consists of a host structure on which a TMD is mounted. The actuator force is created in parallel with the TMD mechanical damper and spring. Referring to Fig. 6.1, the impedance Z_{ex} is created in the shunt circuit of the actuator using power electronic techniques [62]. The impedance consists of the negative resistance $-r_{\text{in}}$ and the negative inductance $-L_{\text{in}}$ to cancel the internal impedance of the actuator. As a result, only the variable inductance L in parallel with the variable resistance R remain in the shunt circuit.

6.2.1 Actuator Force and Power

Considering the shunt circuit, it can be shown that the force created by the actuator can be written as

$$f_{\text{a}} = k_{\text{em}} z_2 + b_{\text{em}} \dot{z}_2, \tag{6.1}$$

while z_2 and $\dot{z}_2$ are the relative displacement and velocity of the TMD, and k_{em}, b_{em} are the electromechanical stiffness and damping terms that the actuator creates. They can be calculated as follows

$$k_{\text{em}} = \frac{{c_{\text{em}}}^2}{L}, \tag{6.2}$$

$$b_{\text{em}} = \frac{{c_{\text{em}}}^2}{R}, \tag{6.3}$$

where c_{em} is the electromechanical coupling constant of the actuator defined as

$$c_{\text{em}} = \frac{f_{\text{a}}}{i}, \tag{6.4}$$

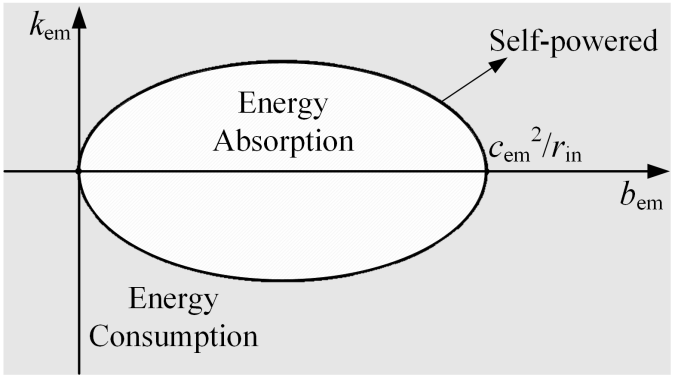

Figure 6.2: Energy regenerating range for the active TMD

in which i is the actuator shunt current. The above analysis shows that the shunt circuit, shown in Fig. 6.1, renders the system behavior similar to a spring-damper combination. However, the system may require energy to create the shunt impedance Z_{ex}.

In the case that the TMD has a single-harmonic motion with amplitude Z_2 and frequency ω, the average power generated in the shunt circuit can be calculated as

$$P_{avg} = \frac{1}{2}|Z_2|^2(\omega^2(b_{em} - \frac{r_{in}}{{c_{em}}^2}{b_{em}}^2) - \frac{r_{in}}{{c_{em}}^2}{k_{em}}^2) \tag{6.5}$$

where r_{in} is the internal resistance of the actuator. According to (6.5), creating stiffness k_{em} is always energy consuming, while creating damping b_{em} can result in power consumption or regeneration depending on value and sign of damping.

To avoid injection of energy from the actuator into the vibration system, which may make the system unstable, it is possible to calculate the range of damping and stiffness that keep the TMD self-powered or energy regenerative. To this end, b_{em} and k_{em} in (6.5) are plotted with respect to each other for constant $|Z_2|$ and ω as shown by the oval curve in Fig. 6.2.

According to Fig. 6.2, if the set (b_{em}, k_{em}) is inside the oval shape, the TMD regenerates power from the vibrations– otherwise it consumes energy. In particular, if $b_{em} < 0$, the actuator consumes power and injects energy into the system as a negative damper. Besides, if $c_{em}^2/r_{in} < b_{em}$, the actuator consumes power to create high damping as already discussed in [41]. To find the range of k_{em} that keeps the system self-powered, (6.5) can be used. The resulting allowable and self-powered range in terms of the two variables can be summarized as follows

$$0 \leq b_{em} \leq c_{em}^2/r_{in}, \tag{6.6}$$

$$-c_{em}\omega\sqrt{\frac{b_{em}}{r_{in}} - (\frac{b_{em}}{r_{in}})^2} \leq k_{em} \leq c_{em}\omega\sqrt{\frac{b_{em}}{r_{in}} - (\frac{b_{em}}{r_{in}})^2}. \tag{6.7}$$

6.2.2 Main Mass and TMD Vibration

As shown in (6.1), the actuator can be considered as a parallel spring-damper system. Thus the overall stiffness and damping of the TMD are $k_2 + k_{\text{em}}$ and $b_2 + b_{\text{em}}$ respectively. Utilizing these terms in the equations of motion of the vibration system, we have

$$\begin{cases} m_1\ddot{x}_1 + b_1\dot{x}_1 - (b_2 + b_{\text{em}})\dot{z}_2 + k_1 x_1 \\ -(k_2 + k_{\text{em}})z_2 = b_1\dot{y} + k_1 y \\ \\ m_2\ddot{x}_1 + m_2\ddot{z}_2 + (b_2 + b_{\text{em}})\dot{z}_2 \\ +(k_2 + k_{\text{em}})z_2 = 0 \end{cases} \tag{6.8}$$

where x_1 is the main mass absolute displacement, and z_2 is the TMD's relative displacement. Assuming a single harmonic base excitation $y(t) = Y\sin(\omega t)$, the main mass displacement amplitude is given by

$$X_1 = Y\sqrt{\frac{(k_1^2 + b_1^2\omega^2)\Big(\big(k_2 + k_{\text{em}} - m_2\omega^2\big)^2 + \big(w(b_2 + b_{\text{em}})\big)^2\Big)}{\Lambda_1^2 + \omega^2(b_2 + b_{\text{em}})^2\Lambda_2^2 + b_1^2\omega^2\Lambda_3^2 + \Lambda_4}}, \tag{6.9}$$

and the TMD's relative displacement is

$$Z_2 = Y\sqrt{\frac{(k_1^2 + b_1^2\omega^2)(m_2\omega^2)^2}{\Lambda_1^2 + \omega^2(b_2 + b_{\text{em}})^2\Lambda_2^2 + b_1^2\omega^2\Lambda_3^2 + \Lambda_4}}, \tag{6.10}$$

while

$$\begin{aligned} \Lambda_1 &= (k_1 - m_1\omega^2)(k_2 + k_{\text{em}} - m_2\omega^2) - m_2\omega^2(k_2 + k_{\text{em}}), \\ \Lambda_2 &= k_1 - m_1\omega^2 - m_2\omega^2, \\ \Lambda_3 &= k_2 + k_{\text{em}} - m_2\omega^2, \\ \Lambda_4 &= b_1^2(b_2 + b_{\text{em}})^2\omega^4 + 2b_1(b_2 + b_{\text{em}})\omega^2(m_2\omega^2)^2. \end{aligned} \tag{6.11}$$

6.3 Optimum Tuning in Frequency Domain

In the proposed system, the TMD is capable of changing its damping and stiffness to achieve a desired performance. For each excitation frequency ω, the main mass displacement given by (6.10) is minimized using the electromechanical damping b_{em} and stiffness k_{em} as the optimization variables. To avoid system instability and keep the system self-powered, b_{em} and k_{em} are constrained in the range shown as (6.6) and (6.7). A simple two-dimensional grid search is used to find the opti-

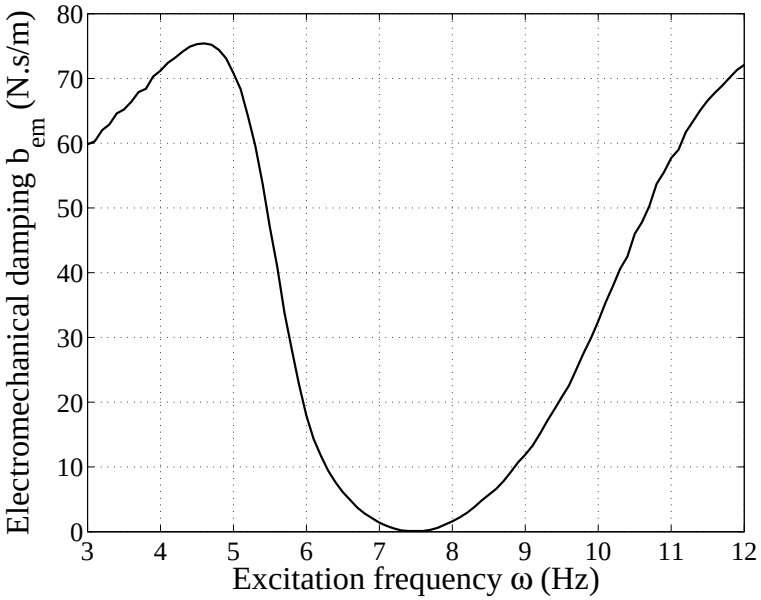

Figure 6.3: Optimal electromechanical damping b_{em}

mal variables. Figures 6.3 and 6.4 show the optimum EM damping and EM stiffness in frequencies between 3 and $12Hz$ for a set of realistic system parameters shown in Table. 6.1.

According to Table 6.1, both the host structure and mechanical TMD, excluding the effect of the actuator, have natural frequencies equal to $7.5Hz$. This makes the TMD ideal for input excitation with a frequency $\omega = 7.5Hz$. Figures 6.3 and 6.4 support this fact since the optimal EM damping and stiffness are equal to zero at the original frequency, which means that the TMD is already tuned. For higher frequencies, optimum k_{em} increases to match the overall frequency of the TMD with the excitation frequency. Considering the power constraint shown as Fig. 6.2, the EM damping has increased too to keep the system in the regenerative region.

Similarly, in frequencies lower than $7.5Hz$, the actuator creates negative stiffness so that the ATMD can track the excitation frequency. However, it seems that the strategy is different when the excitation frequency is less than $5.6Hz$ or more than $10.1Hz$, which are almost equal to the two resonance frequencies of the whole structure (Fig. 6.5). In these cases, the actuator tries to move the resonance frequencies away from the excitation frequency. This is why the EM stiffness starts increasing at frequencies lower than $5.6Hz$ and decreasing when $\omega > 10.1Hz$. This might be more understandable using Fig. 6.5, that shows the response of the system in terms of the host structure displacement ratio X_1/Y.

In Fig. 6.5, performance of the adaptive TMD is compared to other design approaches including the system without TMD, single-frequency design, and a robust approach. The system without TMD has the worst response mostly around $\omega = 7.5Hz$. In contrary, the single-frequency design, results in a very good performance at the host system original resonance frequency, while creating two new uncontrolled resonances at around 5.6 and $10.1Hz$. In the robust design, the damping and stiffness

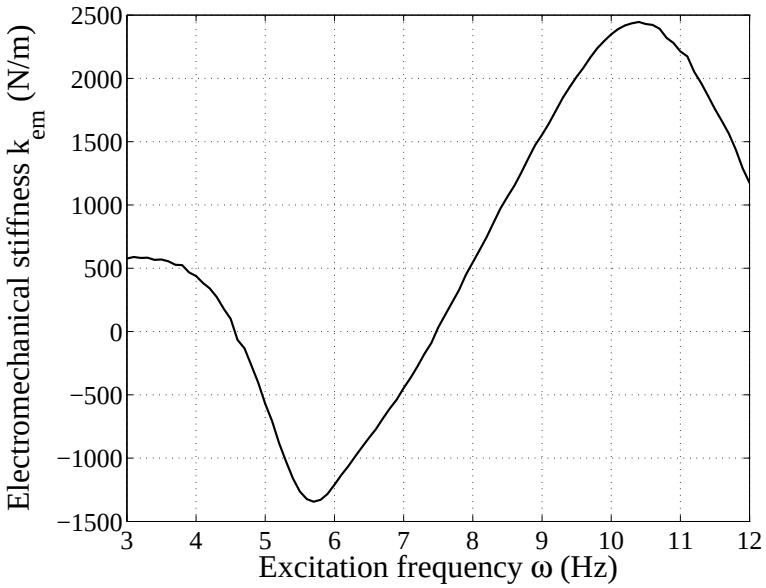

Figure 6.4: Optimal electromechanical stiffness k_{em}

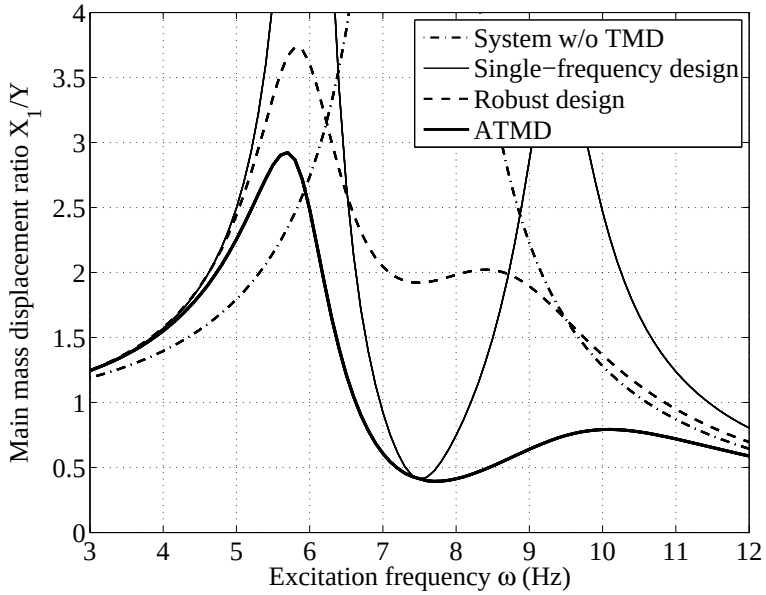

Figure 6.5: Main mass displacement ratio with different design approaches

Table 6.1: Parametric values used for simulating the adaptive tuned mass damper

Parameters	Value
Host structure stiffness, k_1	$22207N/m$
Host structure mass, m_1	$10kg$
Host structure damping, b_1	$40N.s/m$
TMD stiffness, k_2	$4441N/m$
TMD mass, m_2	$2kg$
TMD damping, b_2	$8N.s/m$
Input excitation amplitude, Y	$2mm$
Motor internal resistance, r_{in}	0.98Ω
Actuator force constant, c_{em}	$8.6N/A$

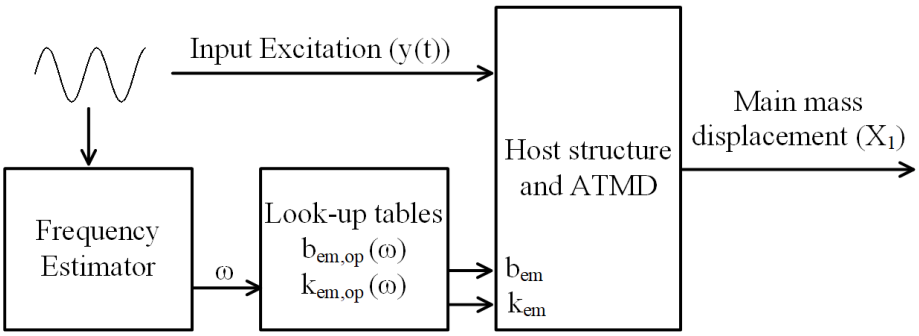

Figure 6.6: Model-based tuning scheme for minimizing X_1 in different frequencies

are designed to minimize the area under the curve in the design frequency range, resulting in a decent behavior of the system both in the original and the new resonance frequencies. However, the ATMD (adaptive TMD) shows an even better performance because of its ability to tune its damping and stiffness following the curves of Figs. 6.3 and 6.4.

6.4 Self-Tuning Algorithm

In the previous Section, it was shown that there are optimal values for electromechanical damping and stiffness b_{em} and k_{em} to minimize the amplitude X_1 of the main mass. The optimal values can be found using the structure model for different frequencies, and the actuator can adopt them using a look-up table as shown in Fig. 6.6.

The system shown in Fig. 6.6 uses the input frequency and a model-based look-up table to tune the TMD; however, this feed-forward and model-based approach is not robust to system changes and model uncertainties. The multi-variable sliding mode extremum-seeking controller [98] is utilized in this paper as a model-free tuning algorithm to take the system to optimal values. Application of this method for the ATMD is shown in Fig. 6.7.

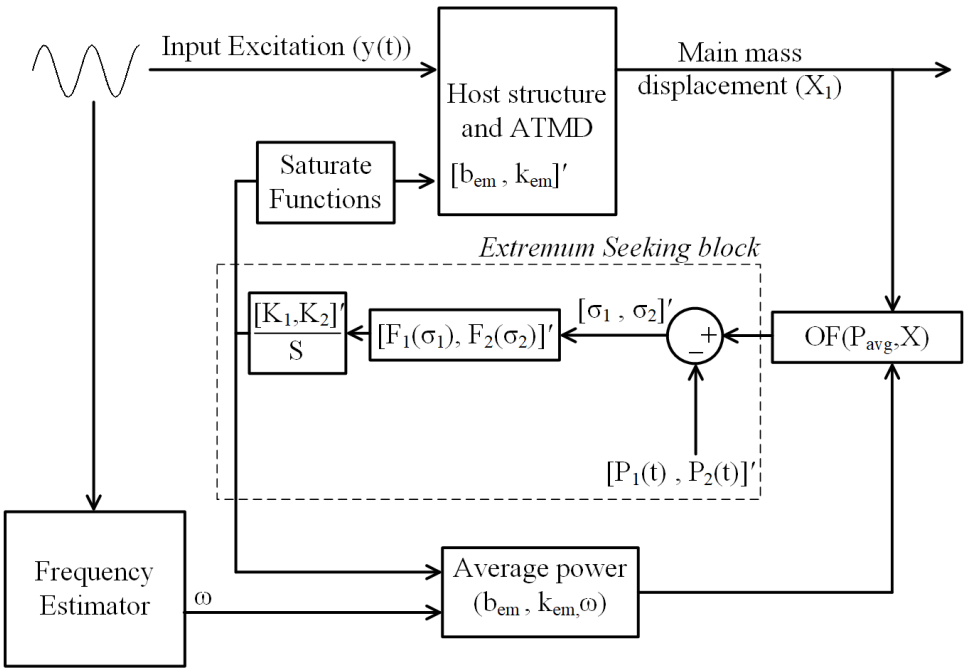

Figure 6.7: Sliding mode extremum-seeking controller for model-free tuning of the ATMD

As shown in Fig. 6.7, the tuning algorithm tries to minimize an objective function OF defined as

$$OF(P_{avg}, X_1) = \begin{cases} X_1, & P_{avg} > 0, \\ X_1 - a.P_{avg}, & P_{avg} < 0. \end{cases} \tag{6.12}$$

The objective function consists of X_1, that should be minimized, but P_{avg} is also added as a piecewise cost function to avoid energy injection into the structure, whereas energy regeneration creates no penalty. The differences between the objective function and two linearly decreasing sliding curves P_i are calculated and used in functions F_i defined as

$$F_i(\sigma_i) = \tan^{-1}(\sin(\pi\sigma_i/\alpha_i), \tag{6.13}$$

where σ_is are sliding mode errors, and α_is define the chattering frequency. The outputs of the control functions F_i are multiplied by the gains K_i and then integrated to calculate the optimization variables. Finally, a saturation block enforcing the constraints (6.6) and (6.7) is used to keep the system in the regenerative range.

The controller is eventually applied to the TMD under study. In the simulation scenario, it is assumed that the structure is excited with frequency $\omega = 8.5Hz$, which is $1Hz$ more than the TMD original design frequency. The initial values of the tunable variables are assumed to be far away from the optimal values. After the system converges to optimal values, it is assumed that the excitation frequency decreases back to the original values of $7.5Hz$ at time $t = 700s$. Behavior of

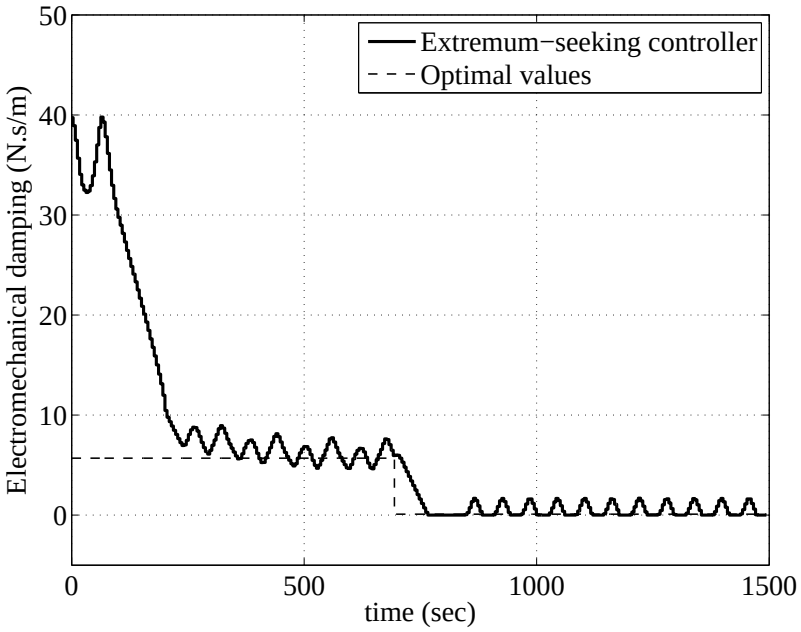

Figure 6.8: Electromechanical damping for minimizing main mass displacement

the system in reaching the optimum values and adapting to the frequency change is shown in Figs. 6.8 to 6.10.

Simulation results show that the extremum-seeking algorithm is correctly tracking optimal values. Even after the sudden change in the excitation frequency at $t = 700sec$, the tuning variables start converging to new optimal values. There is some chattering around the optimal points, which is expected because of the perturb-and-observe behavior of the extremum-seeking controller. As another observation, the curves for EM damping and stiffness are partly clipped mostly when b_{em} is around zero. This is the effect of the saturate function shown in Fig. 6.7 that prevents b_{em} and k_{em} from entering the energy consuming region.

6.5 Conclusion

A shunt-controlled electromagnetic actuator with ability to make variable mechanical impedance was utilized. The actuator was added to a tuned mass damper to create an adaptive vibration absorber. Optimum electromechanical damping and stiffness for minimizing the host structure displacement were calculated using the dynamic model of the system. To avoid instability, the power exchange between the actuator and the structure was constrained to flow only from the structure to the harvester. A multi-variable sliding-mode extremum-seeking controller was used to make the system self-tuning without any need to the mechanical model of the structure. Simulation results show that the controller finds the optimums correctly and tracks them even if the excitation frequency changes.

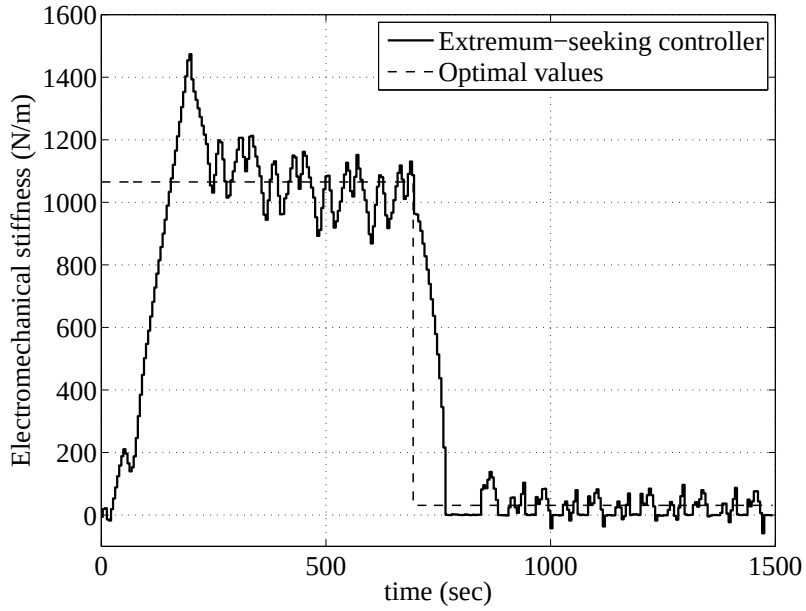

Figure 6.9: Electromechanical stiffness for minimizing main mass displacement

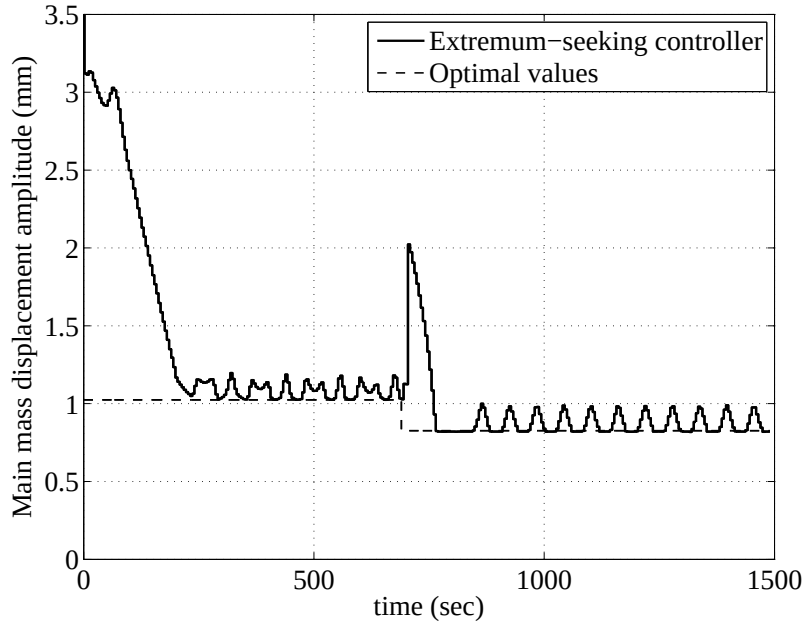

Figure 6.10: Main mass displacement amplitude converging to optimal values

Chapter 7

Conclusions and Suggestions for Future Works

7.1 Summary and Conclusions

In this thesis, effort was devoted to realizing tunable vibration systems. To this end, power electronics design and control techniques were utilized to create electromagnetic actuators with the ability of bi-directional power transfer. It was shown that with proper control of shunt circuit, the actuator can mimic positive and negative damping and stiffness. The actuator with the variable damping and stiffness was utilized in a parallel configuration with passive mechanical elements that create a constant level of damping and stiffness. The addition of the electromagnetic actuator to the passive mechanical structure made it possible to change the overall electromechanical impedance of the structure, which can be interpreted as tunable mechanical impedance.

In Chapter 2, the idea of using shunt control for creating variable damping and stiffness was explored. Power and voltage requirements for creating a certain level of stiffness were studied, and a power electronics system was designed and experimentally validated. It was shown that the proposed shunt control results in a tunable vibration system with variable resonance frequency. It was also shown that using the regenerative force actuation method proposed in this study, efficiency of the stiffness generation is higher compared to the other methods that are already presented in the literature.

In Chapter 3, focus was on creating a negative resistive shunt in the actuator. It was shown that with the negative shunt resistance, the actuator can create damping levels that are larger compared to the short-circuit damping, which was previously assumed as the maximum achievable damping in electromagnetic actuators. Power and voltage requirements were studied, and the idea was experimentally validated. A new mechanical design named cylindrical cam damper was used in the experiments. It was shown that the new design is better in terms of travel-to-length ratio compared to other mechanisms in the literature.

Chapters 4 to 6 take advantage of the technology proved in their preceding Chapters. In Chapters 4 and 5, the tunable vibration control concept is used in the application of vibration energy

harvesting. Sliding mode extremum seeking control is used for autonomous tuning of a vibration energy harvester without using its model. First, damping-only tuning was used in a vibration energy harvester with a maximum allowable displacement. In the experiments, the controller successfully found the maximum power point without violating the maximum displacement constraint. After this achievement, a multi-variable sliding mode extremum seeking controller was proposed to realize the self-tuning with two variables: damping and stiffness. It was shown, using both simulations and experiments, that the novel controller finds the maximum power point with tuning both damping and stiffness in a model-free controller.

Chapter 6, however, uses the tunable vibration control approach in the application of vibration absorption. A tuned mass damper comprising the variable impedance electromagnetic actuator was suggested to work under different excitation frequencies. Similarly, sliding mode extremum seeking controller was used for autonomous tuning of the TMD. A constraint was implemented in the controller to avoid injection of power to the system. It was shown that the proposed TMD tracks the optimum impedance for minimization of the host structure displacements.

7.2 Future Research

With the knowledge and experience obtained during this project, a list of ideas are provided to improve the outcome of this research or open new opportunities related to this field of study. The thesis covers different topics in mechanical vibrations, power electronics and control. The suggestions for future works are classified as below.

7.2.1 Mechanical Vibrations

This thesis focused on creating variable stiffness and damping using a parallel RL shunt configuration. It was shown that this configuration results in creation of forces that are proportional to the actuator displacement and first derivative of displacement. Creating forces proportional to the second derivative of the actuator displacement still needs to be explored. This behavior is interpreted as mechanical inertance that has applications in vibration control [89].

As another idea, it is suggested to study the new opportunities that a variable-stiffness element opens up for optimal vibration control. Vibration control methods using variable damping are extensively reported in the literature [68], while variable-stiffness vibration control is a relatively new concept. It is suggested to study how changing stiffness in the time domain would affect the vibration isolation performance.

It is also suggested to investigate the performance of the tunable actuator when the excitation is more complicated than a single-harmonic sinusoidal wave. Power requirements for the multi-harmonic or random excitation needs further investigation.

7.2.2 Power Electronics

In this study, a switched-mode power converter was used for controlling the current in an electromagnetic actuator comprised of a brushless DC motor. Sliding mode control was used for controlling the current, which proved to be an effective method. However, more study should be devoted to the power electronics part to find the best approach to the current control problem. It is needed to study the circuit configurations and control methods that can minimize the unwanted harmonic content of the electrical current. It is also needed to minimize the switching frequency to avoid switching losses. PWM control is suggested to be examined in this application. Also, buck-boost conversion scheme and multi-level conversion are suggested to improve the quality and efficiency of the power electronics part.

7.2.3 Adaptive Control

In Chapters 4 to 6, extremum-seeking controllers were used for finding the optimum damping and stiffness of the actuator. A novel sliding mode extremum seeking controller was adopted in this study, and a geometric interpretation of the controller was provided. However, a complete stability analysis of the controller would be helpful.

Aside from the sliding mode extremum seeking control, other methods need to be examined and compared. It is also suggested to combine model-based and model-free methods to improve the convergence time and accuracy of the tuning controllers.

Bibliography

[1] A. Abbadi, F. Hamidia, A. Morsli, D. Boukhetala, and L. Nezli. Mppt sliding mode controller for pv system supplying a large scale interconnected grid. In *2017 5th International Conference on Electrical Engineering-Boumerdes (ICEE-B)*, pages 1–6. IEEE, 2017.

[2] Mohamed A.A. Abdelkareem, Lin Xu, Mohamed Kamal Ahmed Ali, Ahmed Elagouz, Jia Mi, Sijing Guo, Yilun Liu, and Lei Zuo. Vibration energy harvesting in automotive suspension system: A detailed review. *Applied Energy*, 229:672–699, 2018.

[3] Rajeevan Amirtharajah and Anantha P Chandrakasan. Self-powered signal processing using vibration-based power generation. *IEEE journal of solid-state circuits*, 33(5):687–695, 1998.

[4] C. Ananthi and B. Kannapiran. Improved design of sliding-mode controller based on the incremental conductance mppt algorithm for pv applications. In *2017 IEEE International Conference on Electrical, Instrumentation and Communication Engineering (ICEICE)*, pages 1–6. IEEE, 2017.

[5] Zackary Martin Anderson, Marco Giovanardi, Clive Tucker, Jonathan R Leehey, Colin Patrick O'shea, Johannes Schneider, Vladimir Gorelik, Richard Anthony Zuckerman, Patrick W Neil, Tyson David Sawyer, et al. Active vehicle suspension, November 3 2015. US Patent 9,174,508.

[6] David P. Arnold. Review of microscale magnetic power generation. *IEEE Transactions on Magnetics*, 43(11):3940–3951, 2007.

[7] Ehsan Asadi, Roberto Ribeiro, Mir Behrad Khamesee, and Amir Khajepour. A new adaptive hybrid electromagnetic damper: Modelling, optimization, and experiment. *Smart Materials and Structures*, 24(7):075003, 2015.

[8] Toshihiko Asami, Osamu Nishihara, and Amr M. Baz. Analytical solutions to h infinity and h2 optimization of dynamic vibration absorbers attached to damped linear systems. *Journal of vibration and acoustics*, 124(2):284–295, 2002.

[9] Simon Baev, Y. Shtessel, Haik Biglari, and R. Adhami. Sliding mode control of a unity power factor ac-to-dc boost converter. In *2007 46th IEEE Conference on Decision and Control*, pages 2005–2010. IEEE, 2007.

[10] Marco Balato, Luigi Costanzo, and Massimo Vitelli. Mppt in wireless sensor nodes supply systems based on electromagnetic vibration harvesters for freight wagons applications. *IEEE Transactions on Industrial Electronics*, 64(5):3576–3586, 2017.

[11] Nick Ilsoe Berg, Rasmus Koldborg Holm, and Peter Omand Rasmussen. A novel magnetic lead screw active suspension system for vehicles. In *Energy Conversion Congress and Exposition (ECCE), 2014 IEEE*, pages 3139–3146. IEEE, 2014.

[12] Thiago Boaventura, Claudio Semini, Jonas Buchli, Marco Frigerio, Michele Focchi, and Darwin G Caldwell. Dynamic torque control of a hydraulic quadruped robot. In *2012 IEEE international conference on robotics and automation*, pages 1889–1894. IEEE, 2012.

[13] Philip Bonello, Michael J. Brennan, Stephen J. Elliott, Julian FV. Vincent, and George Jeronimidis. Designs for an adaptive tuned vibration absorber with variable shape stiffness element. In *Proceedings of the Royal Society of London A: Mathematical, Physical and Engineering Sciences*, volume 461, pages 3955–3976. The Royal Society, 2005.

[14] James A. Bowden, Stephen G. Burrow, Andrea Cammarano, Lindsay R. Clare, and Paul D. Mitcheson. Switched-mode load impedance synthesis to parametrically tune electromagnetic vibration energy harvesters. *IEEE/ASME Transactions on Mechatronics*, 20(2):603–610, 2015.

[15] A. Cammarano, S.G. Burrow, DAW Barton, A. Carrella, and L.R. Clare. Tuning a resonant energy harvester using a generalized electrical load. *Smart Materials and Structures*, 19(5):055003, 2010.

[16] S. Camperi, M. Ghandchi-Tehrani, M. Zilletti, and S.J. Elliott. Active vibration control of an inertial actuator subject to broadband excitation. In *Journal of Physics: Conference Series*, volume 744, page 012038. IOP Publishing, 2016.

[17] N. Caterino, M. Spizzuoco, and A. Occhiuzzi. Ageing effects due to inactivity for magnetorheological seismic dampers: a 10-year experimental investigation. *Smart Materials and Structures*, 27(6):067001, 2018.

[18] Vinod R. Challa, M.G. Prasad, Yong Shi, and Frank T. Fisher. A vibration energy harvesting device with bidirectional resonance frequency tunability. *Smart Materials and Structures*, 17(1):015–035, 2008.

[19] Tai-Hong Cheng and Il-Kwon Oh. A current-flowing electromagnetic shunt damper for multimode vibration control of cantilever beams. *Smart Materials and Structures*, 18(9):095036, 2009.

[20] Justin Creaby, Yaoyu Li, and John E Seem. Maximizing wind turbine energy capture using multivariable extremum seeking control. *Wind Engineering*, 33(4):361–387, 2009.

[21] M. Dansoko, H. Nkwawo, B. Diourté, F. Floret, R. Goma, and G. Kenné. Robust multivariable sliding mode control design for generator excitation of marine turbine in multimachine configuration. *International Journal of Electrical Power & Energy Systems*, 63:423–428, 2014.

[22] Rohan Dayal, Kumar Modepalli, and Leila Parsa. A new optimum power control scheme for low-power energy harvesting systems. *IEEE Transactions on Industry Applications*, 49(6):2651–2661, 2013.

[23] Renkai Ding, Ruochen Wang, Xiangpeng Meng, and Long Chen. A modified energy-saving skyhook for active suspension based on a hybrid electromagnetic actuator. *Journal of Vibration and Control*, 25(2):286–297, 2019.

[24] Alper Erturk and Daniel J. Inman. An experimentally validated bimorph cantilever model for piezoelectric energy harvesting from base excitations. *Smart materials and structures*, 18(2):025009, 2009.

[25] S. Faghihi and M. Moallem. Analysis and design of a low power electronics circuit for energy harvesting applications. In *2012 IEEE International Symposium on Industrial Electronics*, pages 183–188. IEEE, 2012.

[26] M.A. Franchek, M.W. Ryan, and R.J. Bernhard. Adaptive passive vibration control. *Journal of Sound and Vibration*, 189(5):565–585, 1996.

[27] Jacek F. Gieras, Jae-Hyuk Oh, Mihai Huzmezan, and Harshad S. Sane. Electromechanical energy harvesting system, July 17 2012. US Patent 8,222,775.

[28] S. Guo, L. Xu, Y. Liu, X. Guo, and L. Zuo. Modeling and experiments of a hydraulic electromagnetic energy-harvesting shock absorber. *IEEE/ASME Transactions on Mechatronics*, 22(6):2684–2694, Dec 2017.

[29] Bart L.J. Gysen, Jeroen L.G. Janssen, Johannes J.H. Paulides, and Elena A. Lomonova. Design aspects of an active electromagnetic suspension system for automotive applications. *IEEE transactions on industry applications*, 45(5):1589–1597, 2009.

[30] Den Hartog. *Mechanical Vibrations, fourth edition*. McGraw-Hill Book Company, Inc., New York, 1956.

[31] Ibrahim Haskara, Umit Ozguner, and Jim Winkelman. Extremum control for optimal operating point determination and set point optimization via sliding modes. *Journal of Dynamic Systems, Measurement, and Control*, 122(4):719–724, 2000.

[32] Simon Hauser, Matthew Robertson, Auke Ijspeert, and Jamie Paik. Jammjoint: A variable stiffness device based on granular jamming for wearable joint support. *IEEE Robotics and Automation Letters*, 2(2):849–855, 2017.

[33] M. Hendijanizadeh, S. M. Sharkh, S. J. Elliott, and M. Moshrefi-Torbati. Output power and efficiency of electromagnetic energy harvesting systems with constrained range of motion. *Smart Materials and Structures*, 22(12):125009, nov 2013.

[34] K. Hollander and T. Sugar. Concepts for compliant actuation in wearable robotic systems. In *US-Korea Conference (UKC 2004), Research Triangle Park, NC, August*, pages 12–14, 2004.

[35] GOH KIM HOO. *Investigation of direct-current brushed motor based energy regenerative automotive damper*. PhD thesis, 2013.

[36] Gwea Housner, Lawrence A. Bergman, T. K.F. Caughey, Anastassios G. Chassiakos, Richard O. Claus, Sami F. Masri, Robert E. Skelton, T.T. Soong, B.F. Spencer, and James T.P. Yao. Structural control: past, present, and future. *Journal of engineering mechanics*, 123(9):897–971, 1997.

[37] Chen-Yu Hsieh, Bo Huang, Farid Golnaraghi, and Mehrdad Moallem. Regenerative skyhook control for an electromechanical suspension system using a switch-mode rectifier. *IEEE Transactions on Vehicular Technology*, 65(12):9642–9650, 2016.

[38] Tsuyoshi Inoue, Yukio Ishida, and Masaki Sumi. Vibration suppression using electromagnetic resonant shunt damper. *Journal of Vibration and Acoustics*, 130(4):041003, 2008.

[39] Reza N. Jazar. *Advanced Vibrations: A Modern Approach*. Springer Science & Business Media, 2005.

[40] Reza N. Jazar. *Vehicle Dynamics: Theory and Application*. Springer, 2017.

[41] S. H. Kamali, M. Moallem, and S. Arzanpour. Power electronic shunt control for increasing the maximum available damping force in electromagnetic dampers. In *2017 IEEE International Conference on Advanced Intelligent Mechatronics (AIM)*, pages 1514–1519, July 2017.

[42] S. H. Kamali, M. Moallem, and S. Arzanpour. Realization of an energy-efficient adjustable mechatronic spring. *IEEE/ASME Transactions on Mechatronics*, 23(4):1877–1885, Aug 2018.

[43] Seyed Hossein Kamali, Mehrdad Moallem, and Siamak Arzanpour. A self-tuning vibration energy harvester with variable loads and maximum allowable displacement. *Submitted to Smart Materials and Structures*.

[44] Seyed Hossein Kamali, Mehrdad Moallem, and Siamak Arzanpour. Self-tuning active tuned mass damper utilizing constrained multi-variable sliding mode extremum-seeking. In *2018 IEEE Conference on Control Technology and Applications (CCTA)*, pages 127–131. IEEE, 2018.

[45] Anouer Kebir, Lyne Woodward, and Ouassima Akhrif. Extremum-seeking control with adaptive excitation: application to a photovoltaic system. *IEEE Transactions on Industrial Electronics*, 65(3):2507–2517, 2018.

[46] Alireza Khaligh, Peng Zeng, and Cong Zheng. Kinetic energy harvesting using piezoelectric and electromagnetic technologies state of the art. *IEEE Transactions on Industrial Electronics*, 57(3):850–860, 2010.

[47] Byeong-Sang Kim and Jae-Bok Song. Design and control of a variable stiffness actuator based on adjustable moment arm. *IEEE Transactions on Robotics*, 28(5):1145–1151, 2012.

[48] S.K. Korovin and V.I. Utkin. Using sliding modes in static optimization and nonlinear programming. *Automatica*, 10(5):525–532, 1974.

[49] Mojtaba Bahrami Kouhshahi, Joshua Kadel, Jonathan Bird, and Wesley Williams. Designing and experimentally testing a magnetically geared lead screw. *IEEE Transactions on Industry Applications*, 2018.

[50] Dipesh Kumar and Kalyan Chatterjee. A review of conventional and advanced mppt algorithms for wind energy systems. *Renewable and Sustainable Energy Reviews*, 55:957–970, 2016.

[51] Ramona Leewe, Ken Fong, Mehrdad Moallem, and Zahra Shahriari. Novel scheme to tune rf cavities using reflected power. In *28th Linear Accelerator Conf.(LINAC'16), East Lansing, MI, USA, 25-30 September 2016*, pages 757–759. JACOW, Geneva, Switzerland, 2017.

[52] Ramona Leewe, Zahra Shahriari, and Mehrdad Moallem. Resonance frequency control of rf normal conducting cavity using gradient estimator of reflected power. *Nuclear Instruments and Methods in Physics Research Section A: Accelerators, Spectrometers, Detectors and Associated Equipment*, 869:172–179, 2017.

[53] Joachim Leicht and Yiannos Manoli. A 2.6 μw–1.2 mw autonomous electromagnetic vibration energy harvester interface ic with conduction-angle-controlled mppt and up to 95% efficiency. *IEEE Journal of Solid-State Circuits*, 52(9):2448–2462, 2017.

[54] Zhongjie Li, Lei Zuo, Jian Kuang, and George Luhrs. Energy-harvesting shock absorber with a mechanical motion rectifier. *Smart Materials and Structures*, 22(2):025008, 2012.

[55] Changwei Liang, Junxiao Ai, and Lei Zuo. Design, fabrication, simulation and testing of an ocean wave energy converter with mechanical motion rectifier. *Ocean Engineering*, 136:190–200, 2017.

[56] Yilun Liu, Chi-Chang Lin, Jason Parker, and Lei Zuo. Exact h2 optimal tuning and experimental verification of energy-harvesting series electromagnetic tuned-mass dampers. *Journal of Vibration and Acoustics*, 138(6):061003, 2016.

[57] Yilun Liu, Lin Xu, and Lei Zuo. Design, modeling, lab and field tests of a mechanical-motion-rectifier-based energy harvester using a ball-screw mechanism. *IEEE/ASME Trans. Mechatronics*, 22(5):1933–1943, 2017.

[58] Amir Maravandi and Mehrdad Moallem. Regenerative shock absorber using a two-leg motion conversion mechanism. *IEEE/ASME Transactions on Mechatronics*, 20(6):2853–2861, 2015.

[59] Ismenio Martins, Jorge Esteves, Gil D. Marques, and F. Pina Da Silva. Permanent-magnets linear actuators applicability in automobile active suspensions. *IEEE Transactions on vehicular technology*, 55(1):86–94, 2006.

[60] A.J. McDaid and B.R. Mace. A self-tuning electromagnetic vibration absorber with adaptive shunt electronics. *Smart Materials and Structures*, 22(10):105013, 2013.

[61] Andrew J. McDaid and Brian R. Mace. A robust adaptive tuned vibration absorber using semi-passive shunt electronics. *IEEE Transactions on Industrial Electronics*, 63(8):5069–5077, 2016.

[62] Paul D. Mitcheson, Tzern T. Toh, Kwok H. Wong, Steve G. Burrow, and Andrew S. Holmes. Tuning the resonant frequency and damping of an electromagnetic energy harvester using power electronics. *IEEE Transactions on Circuits and Systems II: Express Briefs*, 58(12):792–796, 2011.

[63] T. Morita and S. Sugano. Design and development of a new robot joint using a mechanical impedance adjuster. In *Proceedings of 1995 IEEE International Conference on Robotics and Automation*, volume 3, pages 2469–2475 vol.3, May 1995.

[64] Mohammad Mehdi Naserimojarad, Mehrdad Moallem, and Siamak Arzanpour. A comprehensive approach for optimal design of magnetorheological dampers. *Journal of Intelligent Material Systems and Structures*, 29(18):3648–3655, 2018.

[65] Francesca Negrello, Manuel G. Catalano, Manolo Garabini, Mattia Poggiani, Darwin G Caldwell, Nikos G Tsagarakis, and Antonio Bicchi. Design and characterization of a novel high-compliance spring for robots with soft joints. In *2017 IEEE International Conference on Advanced Intelligent Mechatronics (AIM)*, pages 271–278. IEEE, 2017.

[66] Donghong Ning, Haiping Du, Shuaishuai Sun, Wenfei Li, and Weihua Li. An energy saving variable damping seat suspension system with regeneration capability. *IEEE Transactions on Industrial Electronics*, 2018.

[67] Donghong Ning, Shuaishuai Sun, Haiping Du, Weihua Li, and Nong Zhang. Vibration control of an energy regenerative seat suspension with variable external resistance. *Mechanical Systems and Signal Processing*, 106:94–113, 2018.

[68] Fernando Oliveira, Miguel Ayala Botto, Paulo Morais, and Afzal Suleman. Semi-active structural vibration control of base-isolated buildings using magnetorheological dampers. *Journal of Low Frequency Noise, Vibration and Active Control*, 37(3):565–576, 2018.

[69] Siavash Pakdelian, Morteza Moosavi, Hussain A. Hussain, and Hamid A Toliyat. Control of an electric machine integrated with the trans-rotary magnetic gear in a motor drive train. *IEEE Transactions on Industry Applications*, 53(1):106–114, 2017.

[70] Yaodong Pan, Ümit Özgüner, and Tankut Acarman. Stability and performance improvement of extremum seeking control with sliding mode. *International Journal of Control*, 76(9-10):968–985, 2003.

[71] Joseph A. Paradiso and Thad Starner. Energy scavenging for mobile and wireless electronics. *IEEE Pervasive computing*, 4(1):18–27, 2005.

[72] Alexander V. Pedchenko, Janette Jaques Meyer, and Eric J Barth. Assessing stability and predicting power generation of electromagnetic vibration energy harvesters using bridge vibration data. *IEEE/ASME Transactions on Mechatronics*, 22(1):269–279, 2017.

[73] Alexander V Pedchenko, E Bryn Pitt, and Eric J Barth. Analytical tools for investigating stability and power generation of electromagnetic vibration energy harvesters. *IEEE/ASME Transactions on Mechatronics*, 21(2):717–726, 2016.

[74] Shashank Priya and Daniel J. Inman. *Energy Harvesting Technologies*, volume 21. Springer, 2009.

[75] P.P. Proynov, G.D. Szarka, B.H. Stark, and N. McNeill. Resistive matching with a feed-forward controlled non-synchronous boost rectifier for electromagnetic energy harvesting. In *Applied Power Electronics Conference and Exposition (APEC), 2013 Twenty-Eighth Annual IEEE*, pages 3081–3086. IEEE, 2013.

[76] Feng Qian, Wanlu Zhou, Suresh Kaluvan, Haifeng Zhang, and Lei Zuo. Theoretical modeling and experimental validation of a torsional piezoelectric vibration energy harvesting system. *Smart Materials and Structures*, 27(4):045018, 2018.

[77] Singiresu S. Rao and Fook Fah Yap. *Mechanical Vibrations*, volume 4. Prentice Hall Upper Saddle River, 2011.

[78] Yaser M. Roshan, Amir Maravandi, and Mehrdad Moallem. Power electronics control of an energy regenerative mechatronic damper. *IEEE Transactions on Industrial Electronics*, 62(5):3052–3060, 2015.

[79] Yaser M. Roshan and M. Moallem. Maximum power point estimation and tracking using power converter input resistance control. *Solar Energy*, 96:177–186, 2013.

[80] Shad Roundy and Yang Zhang. Toward self-tuning adaptive vibration-based microgenerators. In *Smart Structures, Devices, and Systems II*, volume 5649, pages 373–385. International Society for Optics and Photonics, 2005.

[81] E. Rustighi, M.J. Brennan, and B.R. Mace. A shape memory alloy adaptive tuned vibration absorber: design and implementation. *Smart Materials and Structures*, 14(1):19, 2004.

[82] Reza Sabzehgar, Amir Maravandi, and Mehrdad Moallem. Energy regenerative suspension using an algebraic screw linkage mechanism. *IEEE/ASME Transactions on Mechatronics*, 19(4):1251–1259, 2014.

[83] Reza Sabzehgar and Mehrdad Moallem. A boost-type power converter for energy-regenerative damping. *IEEE/ASME Transactions on Mechatronics*, 18(2):725–732, 2013.

[84] Waleed Salman, Lingfei Qi, Xin Zhu, Hongye Pan, Xingtian Zhang, Shehar Bano, Zutao Zhang, and Yanping Yuan. A high-efficiency energy regenerative shock absorber using helical gears for powering low-wattage electrical device of electric vehicles. *Energy*, 2018.

[85] Brian Scully, Lei Zuo, Jurgen Shestani, and Yu Zhou. Design and characterization of an electromagnetic energy harvester for vehicle suspensions. In *ASME 2009 International Mechanical Engineering Congress and Exposition*, pages 1007–1016. American Society of Mechanical Engineers, 2009.

[86] Zahra Shahriari, Ramona Leewe, Mehrdad Moallem, and Ken Fong. Automated tuning of resonance frequency in an rf cavity resonator. *IEEE/ASME Transactions on Mechatronics*, 23(1):311–320, 2018.

[87] Umesh Shinde, Sumant Kadwane, and Snehal Gawande. Rapid mppt of grid tied photovoltaic system with quadratic converter using sliding mode like controller. *International Journal of Renewable Energy Research (IJRER)*, 7(4):2032–2040, 2017.

[88] Yuri Shtessel, Simon Baev, and Haik Biglari. Unity power factor control in three-phase ac/dc boost converter using sliding modes. *IEEE Transactions on Industrial Electronics*, 55(11):3874–3882, 2008.

[89] Malcolm C. Smith. Synthesis of mechanical networks: the inerter. In *Decision and Control, 2002, Proceedings of the 41st IEEE Conference on*, volume 2, pages 1657–1662. IEEE, 2002.

[90] Dirk Spreemann, Daniel Hoffmann, Bernd Folkmer, and Yiannos Manoli. Numerical optimization approach for resonant electromagnetic vibration transducer designed for random vibration. *Journal of Micromechanics and Microengineering*, 18(10):104001, 2008.

[91] Alessandro Stabile, Guglielmo S Aglietti, and Guy Richardson. Electromagnetic damper design using a multiphysics approach. In *Active and Passive Smart Structures and Integrated Systems 2015*, volume 9431, page 943120. International Society for Optics and Photonics, 2015.

[92] Alessandro Stabile, Guglielmo S Aglietti, Guy Richardson, and Geert Smet. A 2-collinear-dof strut with embedded negative-resistance electromagnetic shunt dampers for spacecraft micro-vibration. *Smart Materials and Structures*, 26(4):045031, 2017.

[93] Alessandro Stabile, Guglielmo S Aglietti, Guy Richardson, and Geert Smet. Design and verification of a negative resistance electromagnetic shunt damper for spacecraft micro-vibration. *Journal of Sound and Vibration*, 386:38–49, 2017.

[94] N.G. Stephen. On energy harvesting from ambient vibration. *Journal of sound and vibration*, 293(1):409–425, 2006.

[95] Jiantao Sun, Zhao Guo, Yubing Zhang, Xiaohui Xiao, and Jianrong Tan. A novel design of serial variable stiffness actuator (svsa) based on an archimedean spiral relocation mechanism. *IEEE/ASME Transactions on Mechatronics*, 2018.

[96] Gyorgy D. Szarka, Stephen G. Burrow, Plamen P. Proynov, and Bernard H. Stark. Maximum power transfer tracking for ultralow-power electromagnetic energy harvesters. *IEEE transactions on Power Electronics*, 29(1):201–212, 2014.

[97] Xiudong Tang, Teng Lin, and Lei Zuo. Design and optimization of a tubular linear electromagnetic vibration energy harvester. *IEEE/ASME Transactions on Mechatronics*, 19(2):615–622, 2014.

[98] Shirin Fartash Toloue and Mehrdad Moallem. Multivariable sliding-mode extremum seeking control with application to mppt of an alternator-based energy conversion system. *IEEE Transactions on Industrial Electronics*, 64(8):6383–6391, 2017.

[99] Andrea Tonoli, Nicola Amati, Joaquim Girardello Detoni, Renato Galluzzi, and Enrico Gasparin. Modelling and validation of electromechanical shock absorbers. *Vehicle System Dynamics*, 51(8):1186–1199, 2013.

[100] E. Turco and P. Gardonio. Sweeping shunted electro-magnetic tuneable vibration absorber: Design and implementation. *Journal of Sound and Vibration*, 407:82–105, 2017.

[101] Ronald Van Ham, Thomas G. Sugar, Bram Vanderborght, Kevin W Hollander, and Dirk Lefeber. Compliant actuator designs. *IEEE Robotics & Automation Magazine*, 16(3), 2009.

[102] Bram Vanderborght, Alin Albu-Schäffer, Antonio Bicchi, Etienne Burdet, Darwin G Caldwell, Raffaella Carloni, M Catalano, Oliver Eiberger, Werner Friedl, Ganesh Ganesh, et al. Variable impedance actuators: A review. *Robotics and autonomous systems*, 61(12):1601–1614, 2013.

[103] Nicola Vitiello, Tommaso Lenzi, Stefano Roccella, Stefano Marco Maria De Rossi, Emanuele Cattin, Francesco Giovacchini, Fabrizio Vecchi, and Maria Chiara Carrozza. Neuroexos: A powered elbow exoskeleton for physical rehabilitation. *IEEE Transactions on Robotics*, 29(1):220–235, 2013.

[104] Nikola Vujic, Donald J. Leo, and Douglas K. Lindner. Power regeneration in active vibration isolation systems. In *Smart Structures and Materials*, pages 368–379. International Society for Optics and Photonics, 2003.

[105] Ruochen Wang, Renkai Ding, and Long Chen. Application of hybrid electromagnetic suspension in vibration energy regeneration and active control. *Journal of Vibration and Control*, 24(1):223–233, 2018.

[106] William Weaver Jr., Stephen P. Timoshenko, and Donovan Harold Young. *Vibration problems in engineering*. John Wiley & Sons, 1990.

[107] C.B. Williams and Rob B. Yates. Analysis of a micro-electric generator for microsystems. *Sensors and Actuators A: Physical*, 52(1-3):8–11, 1996.

[108] Xiaoming Wu, Jianhui Lin, Seiki Kato, Kai Zhang, Tianling Ren, and Litian Liu. A frequency adjustable vibration energy harvester. *Proceedings of PowerMEMS*, pages 245–248, 2008.

[109] Longhan Xie, Jiehong Li, Siqi Cai, and Xiaodong Li. Electromagnetic energy-harvesting damper with multiple independently controlled transducers: On-demand damping and optimal energy regeneration. *IEEE/ASME Transactions on Mechatronics*, 22(6):2705–2713, 2017.

[110] Bo Yan, Yajun Luo, and Xinong Zhang. Structural multimode vibration absorbing with electromagnetic shunt damping. *Journal of Vibration and Control*, 22(6):1604–1617, 2016.

[111] Zhengbao Yang, Jean Zu, and Zhuo Xu. Reversible nonlinear energy harvester tuned by tilting and enhanced by nonlinear circuits. *IEEE/ASME Transactions on Mechatronics*, 21(4):2174–2184, 2016.

[112] Yue Yuan, Mingyi Liu, Wei-Che Tai, and Lei Zuo. Design and treadmill test of a broadband energy harvesting backpack with a mechanical motion rectifier. *Journal of Mechanical Design*, 140(8):085001, 2018.

[113] Chunlei Zhang and Raúl Ordóñez. *Extremum-seeking control and applications: a numerical optimization-based approach*. Springer Science & Business Media, 2011.

[114] Xinjie Zhang, Zhihua Li, Konghui Guo, Fumiao Zheng, and Zhong Wang. A novel pumping magnetorheological damper: Design, optimization, and evaluation. *Journal of Intelligent Material Systems and Structures*, 28(17):2339–2348, 2017.

[115] Xinong Zhang, Hongpan Niu, and Bo Yan. A novel multimode negative inductance negative resistance shunted electromagnetic damping and its application on a cantilever plate. *Journal of Sound and Vibration*, 331(10):2257–2271, 2012.

[116] Yuxin Zhang, Hong Chen, Konghui Guo, Xinjie Zhang, and Shengbo Eben Li. Electro-hydraulic damper for energy harvesting suspension: Modeling, prototyping and experimental validation. *Applied energy*, 199:1–12, 2017.

[117] Wenguang Zheng, Bo Yan, Hongye Ma, Rongyang Wang, Jiangming Jia, Lu Zhang, and Chuanyu Wu. Tuning of natural frequency with electromagnetic shunt mass. *Smart Materials and Structures*, 2018.

[118] Daming Zhou, Ahmed Al-Durra, Imad Matraji, Alexandre Ravey, and Fei Gao. Online energy management strategy of fuel cell hybrid electric vehicles: A fractional-order extremum seeking method. *IEEE Transactions on Industrial Electronics*, 2018.

[119] Dibin Zhu, Michael J Tudor, and Stephen P Beeby. Strategies for increasing the operating frequency range of vibration energy harvesters: a review. *Measurement Science and Technology*, 21(2):022001, 2009.

[120] Michele Zilletti, Stephen J Elliott, and Emiliano Rustighi. Optimisation of dynamic vibration absorbers to minimise kinetic energy and maximise internal power dissipation. *Journal of sound and vibration*, 331(18):4093–4100, 2012.

[121] Lei Zuo, Xiaoming Chen, and Samir Nayfeh. Design and analysis of a new type of electromagnetic damper with increased energy density. *Journal of vibration and acoustics*, 133(4):041006, 2011.

[122] Lei Zuo and Wen Cui. Dual-functional energy-harvesting and vibration control: electromagnetic resonant shunt series tuned mass dampers. *Journal of vibration and acoustics*, 135(5):051018, 2013.